

Technical University of Denmark



The Phase of Pb/Ge(111): A Surface X-Ray Diffraction Study

Grey, Francois

Publication date:
1988

Document Version
Publisher's PDF, also known as Version of record

[Link back to DTU Orbit](#)

Citation (APA):
Grey, F. (1988). The Phase of Pb/Ge(111): A Surface X-Ray Diffraction Study. (Risø-M; No. 2737).

DTU Library

Technical Information Center of Denmark

General rights

Copyright and moral rights for the publications made accessible in the public portal are retained by the authors and/or other copyright owners and it is a condition of accessing publications that users recognise and abide by the legal requirements associated with these rights.

- Users may download and print one copy of any publication from the public portal for the purpose of private study or research.
- You may not further distribute the material or use it for any profit-making activity or commercial gain
- You may freely distribute the URL identifying the publication in the public portal

If you believe that this document breaches copyright please contact us providing details, and we will remove access to the work immediately and investigate your claim.

D: 191363224

THE PHASES OF Pb/Ge(111): A SURFACE X-RAY DIFFRACTION STUDY

François Grey

Abstract: This report describes the results of several surface X-ray diffraction measurements of a chemisorbed overlayer of Pb on the Ge(111) surface. Three phases of Pb/Ge(111) exist in the monolayer regime: the α - and β -phases with a $\sqrt{3} \times \sqrt{3} R30^\circ$ unit cell, and a high-temperature 1×1 phase. In the 1×1 phase of Pb/Ge(111), isotropic x-ray scattering is observed consistent with a two-dimensional liquid phase. Measurements of the integer-order Bragg reflections through the $\sqrt{3} \times \sqrt{3} R30^\circ \rightarrow 1 \times 1$ transition confirm the liquid-like nature of the 1×1 phase, and show that the liquid layer is modulated by the periodic potential of the substrate. By measuring variations of the $(2/3, 2/3)$ surface Bragg reflection from the $\sqrt{3} \times \sqrt{3} R30^\circ$ phase as a function of temperature and coverage, a simple phase diagram for Pb/Ge(111) is deduced. Below $1/3$ ML (where 1 ML is one Pb atom per Ge surface atom) the α -phase coexists with the 1×1 phase. Between $1/3$ ML and $4/3$ ML, α - and β -phases form a two-phase system displaying phase separation. Analogies with simple theoretical phase diagrams are emphasized.

March 1988

Risø National Laboratory, DK-4000 Roskilde, Denmark

This report is submitted in partial fulfillment of the requirements for a Ph.D. (lic. scient.) degree at Copenhagen University. The supervisor is Prof. Hans Henrik Andersen of Copenhagen University; co-supervisors are Dr. Mourits Nielsen of Risø National Laboratory and Dr. Robert Johnson of the Max Planck Institute for Solid State Research.

Dette er en rapport over et licentiatstudium ved Københavns Universitet. Vejleder er Prof. Hans Henrik Andersen, Københavns Universitet; medvejleder er Mourits Nielsen fra Forskningscenter Risø og Robert Johnson fra Max Planck Institutet for faststofforskning i Stuttgart.

ISBN 87-550-1454-2

ISSN 0418-6435

Grafisk Service Risø 1988

CONTENTS

	Page
1. INTRODUCTION	5
1.1 Motivation	5
1.2 Pb/Ge(111) : Review	7
1.3 References	15
2. SURFACE X-RAY DIFFRACTION: THEORY AND EXPERIMENT ..	17
2.1 Kinematical Scattering Theory	17
2.2 Grazing Incidence Geometry	22
2.3 Sample Preparation and Characterization	24
2.4 Measurement Procedure	28
2.5 Structural Analysis of Pb/Ge(111)	30
2.6 References	36
3. OBSERVATION OF LIQUID SCATTERING FROM A 2d LAYER OF Pb	
3.1 Introduction	37
3.2 Theory	37
3.3 Experimental Method	41
3.4 Discussion	44
3.5 Conclusion	45
3.6 References	46
4. NATURE OF THE HIGH-TEMPERATURE 1×1 PHASE OF Pb/Ge(111)	
4.1 Introduction	47
4.2 Theory	48
4.3 Experimental Method	49
4.4 Analysis	51
4.5 Discussion	56
4.6 Conclusion	57
4.7 References	57

5. STUDY OF THE PHASE DIAGRAM OF Pb/Ge(111)	59
5.1 Introduction	59
5.2 Theory	60
5.3 Experimental Method	64
5.4 Overview	65
5.5 Analysis	68
5.6 Discussion	73
5.7 Conclusions	75
5.8 References	75
APPENDIX	76
Summary and Outlook	80
Acknowledgments	81

1. INTRODUCTION

This report has two goals: to present recent experimental results concerning chemisorbed Pb/Ge(111), and to provide a review of this chemisorption system that may serve as a useful reference for other researchers. In many respects, Pb/Ge(111) is an ideal system for studying surface phases and phase transitions, and it is hoped that this report will stimulate further research, both experimental and theoretical.

The first two chapters of the report summarize what is known about Pb/Ge(111) to date and provide the theoretical and experimental background to the measurements described in Chapters 3-5. The main experimental technique for these studies has been surface X-ray diffraction. Measurements were carried out at the wiggler line W1 of the Hamburg Synchrotron Radiation Laboratory (HASYLAB), FRG, as well as on a 12 kW rotating anode at Risø National Laboratory, Denmark. The experiments are part of a collaboration between the Max Planck Institute for Solid State Physics, Stuttgart, FRG, and the Risø National Laboratory.

1.1 Motivation

Chemisorbed phases are of interest as experimental realizations of two-dimensional systems. Phase transitions in two dimensions play a special role in the theory of critical phenomena (ref. 1). For example, two is the highest dimension for which an analytical solution of the Ising model exists. More generally, fluctuation-driven second-order phase transitions appear to occur more easily in two dimensions. In one dimension, long-wavelength fluctuations preclude phase transitions above absolute zero, while in three dimensions, fluctuations are often so weak that transitions are first-order, and thus difficult to study theoretically. Two dimensional systems are thus favoured for testing the theoretical predictions concerning second-order transitions. A large amount of experimental data exists, but it is derived predominantly from measurements of rare gases physisorbed on graphite. Although there is much still to be learned from physisorbed films, chemisorbed layers offer a potentially much richer variety of phases and phase transitions.

Before embarking on a detailed study of a phase transition of an adsorbed layer, it is helpful to know what, exactly, the phases are above and below the transition, and this is an incentive to determine the phase diagram of the system. This argument can be turned around: phase diagrams of chemisorbed layers are of intrinsic interest

as they can in principle yield detailed information about adsorbate-substrate interactions; studying phase transitions helps to determine the nature of the phase diagram (ref. 2).

If a chemisorbed film is to approximate a 2d system, one stringent experimental condition must be fulfilled: the chemisorbed atoms should be confined to the surface at all temperatures. This means, thermodynamically, there must be a large difference in chemical potential between the adsorbed film and its vapour, and between the adsorbed film and dissolved adsorbate atoms in the bulk. In the past it has not always been possible to meet such requirements. For example in the study of chemisorbed O/Ni(111) (ref. 3) it was found that near the $2 \times 2 \rightarrow 1 \times 1$ transition Oxygen begins to dissolve into the Ni in appreciable amounts. The study of Pb/Cu(110) (ref. 4) showed structural changes on annealing associated with desorption of Pb.

In the case of Pb/Ge(111) the mutual solid solubilities are negligible at all temperatures (ref. 5). Desorption of Pb is negligible (on the time scale of the experiment) only at temperatures below about 300° C. But this does not overly restrict the experimenter, since one of the most interesting features of the phase diagram is a transition at 180° C.

A further experimental requirement is ultra-high-vacuum (UHV), because chemisorbed films are generally much more reactive than rare gases on graphite. Even with UHV, surface reactivity can be a major technical problem. Fortunately, Pb/Ge(111) is comparatively unreactive. In particular, the dense-packed Pb layer of the β -phase is very inert, showing negligible decay in a UHV transfer chamber over periods of up to two weeks. Further, we have found that the surface can be regenerated to its original clean condition by a brief anneal at about 200° C.

For the analysis of phase transition data, the structure of the various phases should be reasonably well understood on the atomic scale, and the occurrence of a transition should result in an easily measurable effect (large dynamic range). In both these respects Pb/Ge(111) is a good candidate. There are, as a function of coverage, only two room temperature phases, and their simple structure has been elucidated with surface X-ray diffraction (ref. 6,7). Because Pb is such a strong scatterer of x-rays, the surface Bragg reflections can easily be measured with a rotating anode. At the wiggler line in HASYLAB, the strongest surface reflection can be monitored over more than two decades in intensity, which is an impressive range bearing in mind that an atomic monolayer contains only of the order of 10^{15} scatterers.

Finally, there is one unsolved technical problem: so-called "finite-size" effects. These hamper detailed comparison between theoretical results which apply to infinite, ideal systems and experimental results which apply to the real, imperfect, finite world. Eliminating surface defects (point defects, steps, antiphase boundaries) is difficult, if not impossible. Chemical etching and argon-ion bombardment are part of the standard substrate preparation technique of Ge(111), leading inevitably to etch pits and near-surface damage. The accuracy to which the crystallographic surface can be cut, typically $\pm 0.1^\circ$, implies terrace widths of less than 2000 Å. Further cause for concern is the non-uniformity of temperature and of adsorbate coverage. Fortunately, because practically all adsorption experiments face similar problems, theorists have made some effort to determine the consequences of such finite-size effects (ref. 8).

1.2 Pb/Ge(111): Review

Early Low-Energy-Electron-Diffraction (LEED) studies of clean and chemisorption-induced reconstructions of Si(111) and Ge(111) consisted mainly of cataloging the myriad structures according to the symmetry of the LEED patterns. In general, the unit cells are too large for quantitative LEED analysis. Nevertheless, the inspired guesswork of the early studies bears reviewing.

Fig. 1.1 shows a conventional unit cell of a diamond-type lattice cleaved open to reveal the (111) surface, with the LEED surface basis vectors $[10]$ and $[01]$.

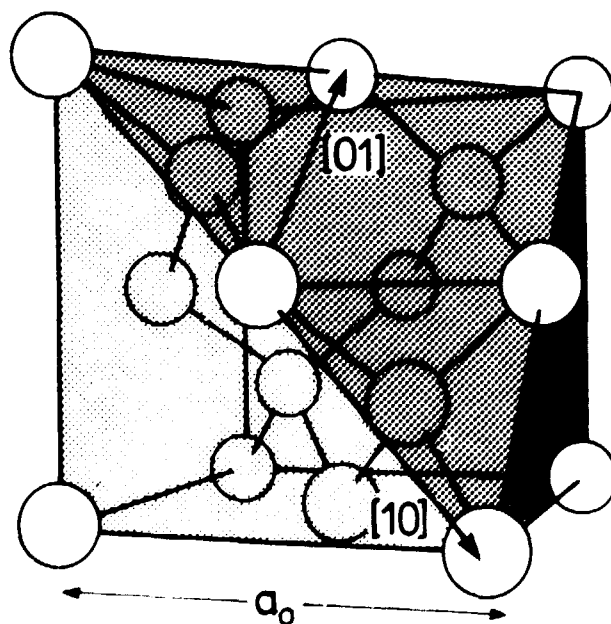


Fig. 1.1: Diamond lattice unit cell and (111) plane.

Fig. 1.2 indicates the relation between the 1×1 unit cell of the ideal surface and the $\sqrt{3} \times \sqrt{3} R30^\circ$ unit cell. Coverage θ is measured in monolayers (ML), 1 ML being one chemisorbed atom per top layer Ge atom of the unreconstructed, ideal Ge(111) surface. Fig. 1.2 illustrates two other important points. First, there are three high symmetry sites on the (111) surface, about which the substrate has $3m$ point symmetry. These are denoted T_1 , T_4 and H_3 and correspond to positions above the first, second and fourth Ge layer, respectively. One of these sites is assumed to be a preferred adsorption site for the formation of a simple (one-atom per unit cell) $\sqrt{3}$ phase. Theoretical calculations for Al, Ga and In on Si(111) favour T_4 (ref. 9), but there are as yet no predictions for Pb/Ge(111). The second point is that the $\sqrt{3}$ structure has three sub-domains: the unit cell can be shifted to positions (b) and (c). The sub-domains are completely analogous to those of the $\sqrt{3}$ structures of physisorbed gases on graphite (ref. 10). In general, any $n \times m$ registered structure has nm subdomains. The importance of the number of subdomains is that they determine the theoretical universality class to which an order-disorder phase transition of the chemisorbed layer belongs, if such a transition occurs (ref. 10).

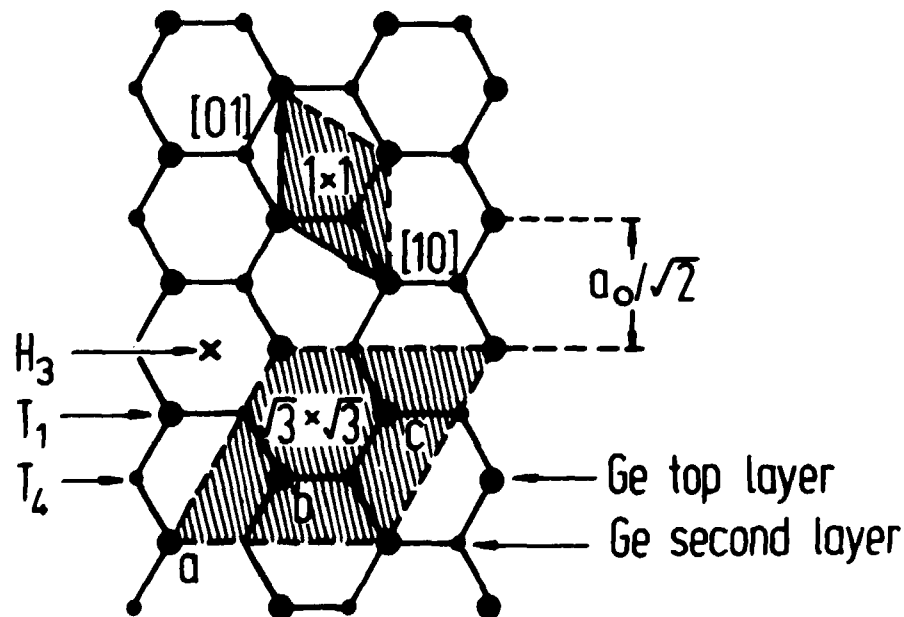


Fig. 1.2: Relationship between 1×1 and $\sqrt{3} \times \sqrt{3} R30^\circ$ unit cells. Also indicated are high symmetry sites H_3 , T_1 , T_4 of the Ge(111) surface and origins for the a , b , c subdomains of the $\sqrt{3}$ structure.

Fig. 1.3 illustrates the relation between the real space lattice and the reciprocal (01) and (10) vectors. The first fractional-order reflections due to a $\sqrt{3}$ superstructure are indicated.

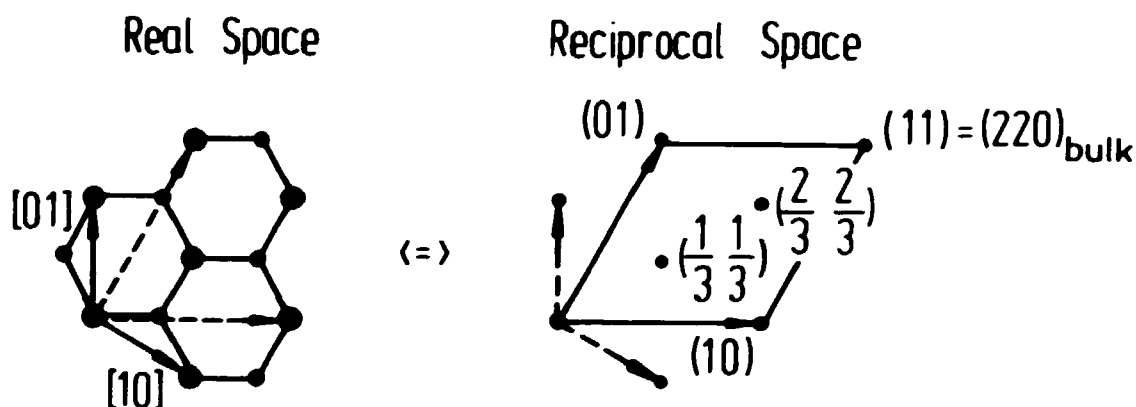


Fig. 1.3: Relationship between real and reciprocal lattice vectors of the 1×1 unit cell (solid) and the $\sqrt{3}$ unit cell (dashed).

Although Pb/Ge(111) has only recently been the subject of experimental investigations, a closely related system, Pb/Si(111), was studied early on by Estrup and Morrison (ref. 11). These authors found, besides a metastable "incommensurate" phase, two stable phases as a function of coverage. The models proposed by Estrup and Morrison, on the basis of variations in the LEED intensities as a function of coverage are shown in Fig. 1.4(a,b), and correspond to a dilute phase, $\theta = 1/3$, and a dense phase, $\theta = 4/3$. The attentive reader will note that the dense phase has $\frac{1}{2}\sqrt{3}$ symmetry. However, inequivalent relaxations of the Pb atoms reduce that symmetry to $\sqrt{3}$, and at the same time explain the weak $(1/3, 1/3)$ reflections, which are the characteristic feature of the dense phase LEED pattern (these reflections would be absent if the structure were strictly $\frac{1}{2}\sqrt{3}$).

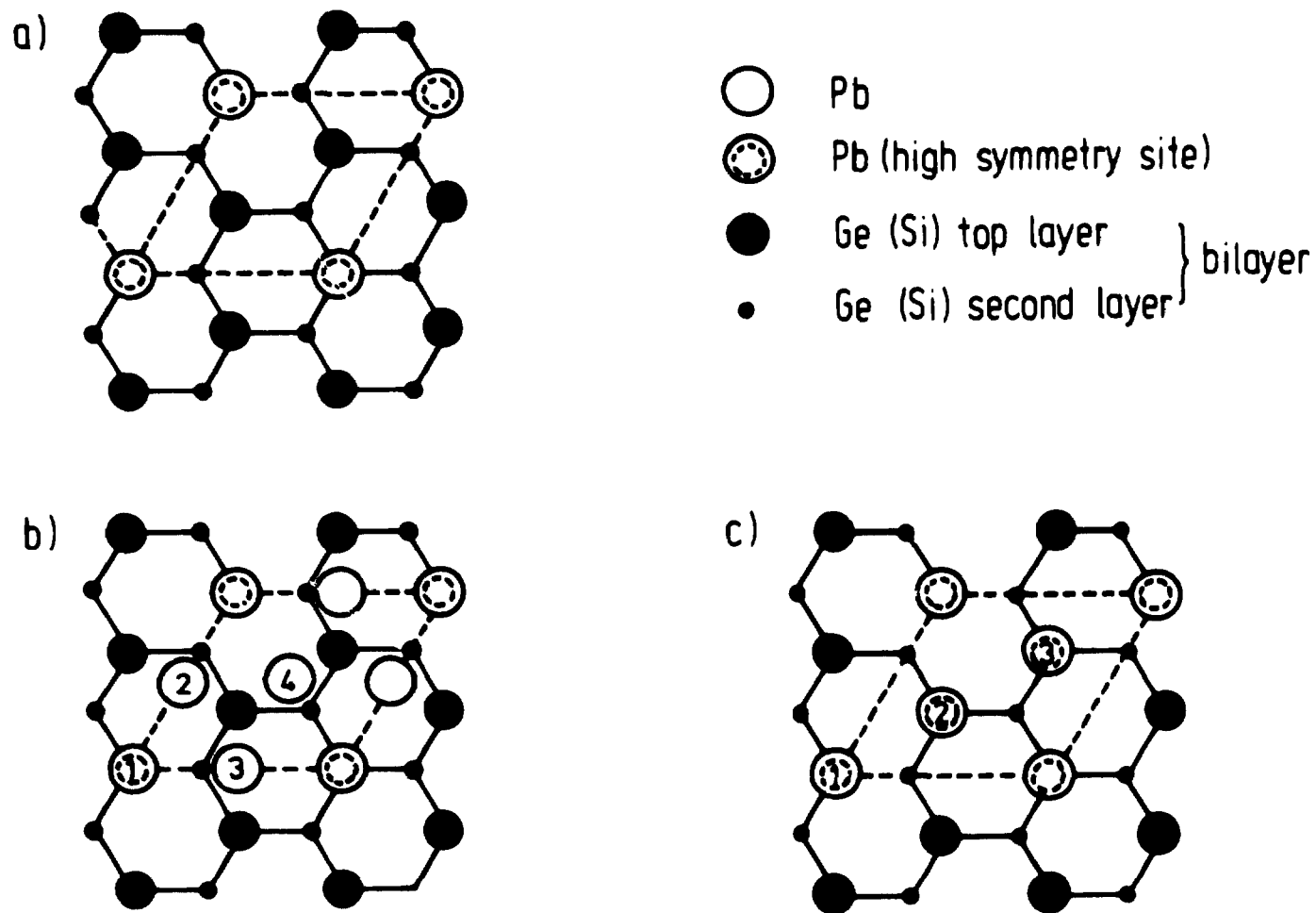


Fig. 1.4a-c: Models for the $\sqrt{3}$ unit cell. (a) Simple model with one atom per unit cell ($1/3$ ML); (b) close-packed Pb layer model ($4/3$ ML); (c) distorted single absorption site model (1 ML)

More recently, independent studies of Pb/Ge(111) by Metois and Le Lay (ref. 12), and by Ichikawa (ref. 13), reached somewhat differing conclusions. Metois and Le Lay identified two $\sqrt{3}$ structures as a function of coverage, again from the variation in intensity of the (1/3,1/3) and (2/3,2/3) reflections (see Fig. 1.5), as well as from desorption measurements

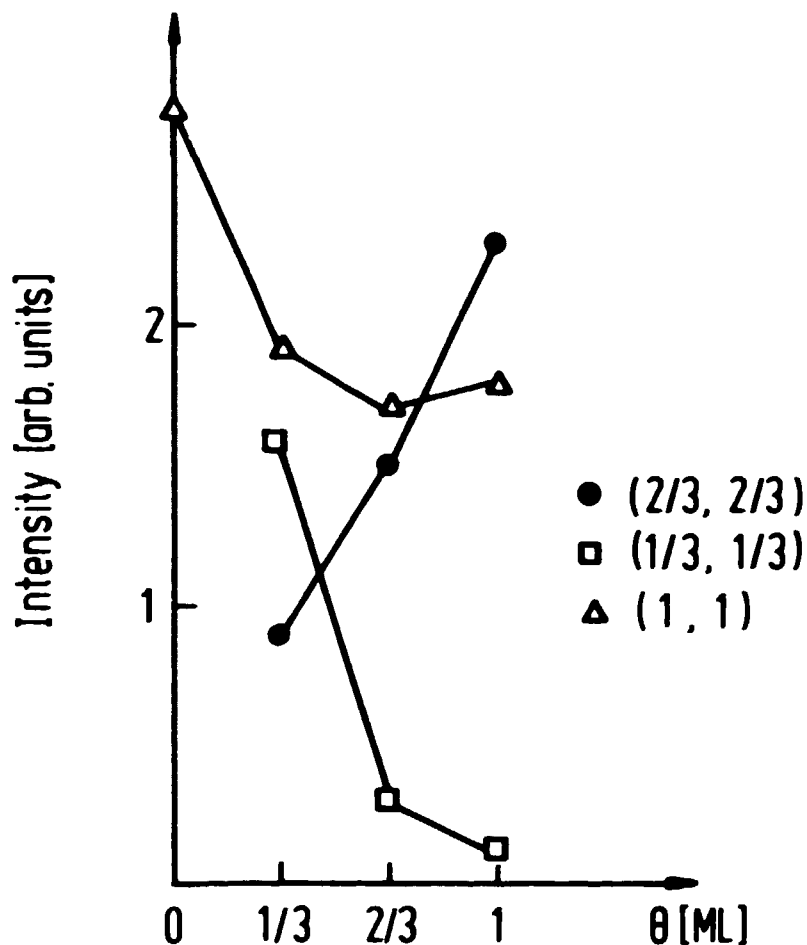


Fig. 1.5: LEED intensities as a function of coverage, from reference 12.

The dilute structure at low coverages is stable up to temperatures at which the desorption rate becomes significant. The desorption rate itself is found to be independent of coverage and obeys

$$-\dot{\theta} = B e^{-A/T}$$

$$A = (2.36 \pm 0.5) \times 10^4 \text{ K}^{-1}$$

$$B = (1.2 \pm 0.5) \times 10^{12} \text{ ML/s}$$

T: temperature in K

which implies negligible desorption rates below 300°C and a rate of .04ML/min at 400° C. The dense structure is found to undergo a reversible transition to a 1x1 structure at 280° C. Metois and Le Lay conclude that the 1×1 phase is an ordered structure. Several possible models of the dense $\sqrt{3}$ unit cell are suggested, consistent with the estimated saturation coverage of this phase, $\theta=1\text{ML}$. One example is illustrated in Fig. 1.4c. Beyond the saturation coverage of the dense phase, Pb is found to grow as 3d islands (Stranski-Krastanov growth mode), with orientation $\text{Pb}(111)\parallel\text{Ge}(111)$ and $\text{Pb}(1\bar{1}0)\parallel\text{Ge}(1\bar{1}0)$.

Ichikawa used Reflection High Energy Electron Diffraction (RHEED) measurements to plot a phase diagram for Pb/Ge(111) (see Fig. 1.6).

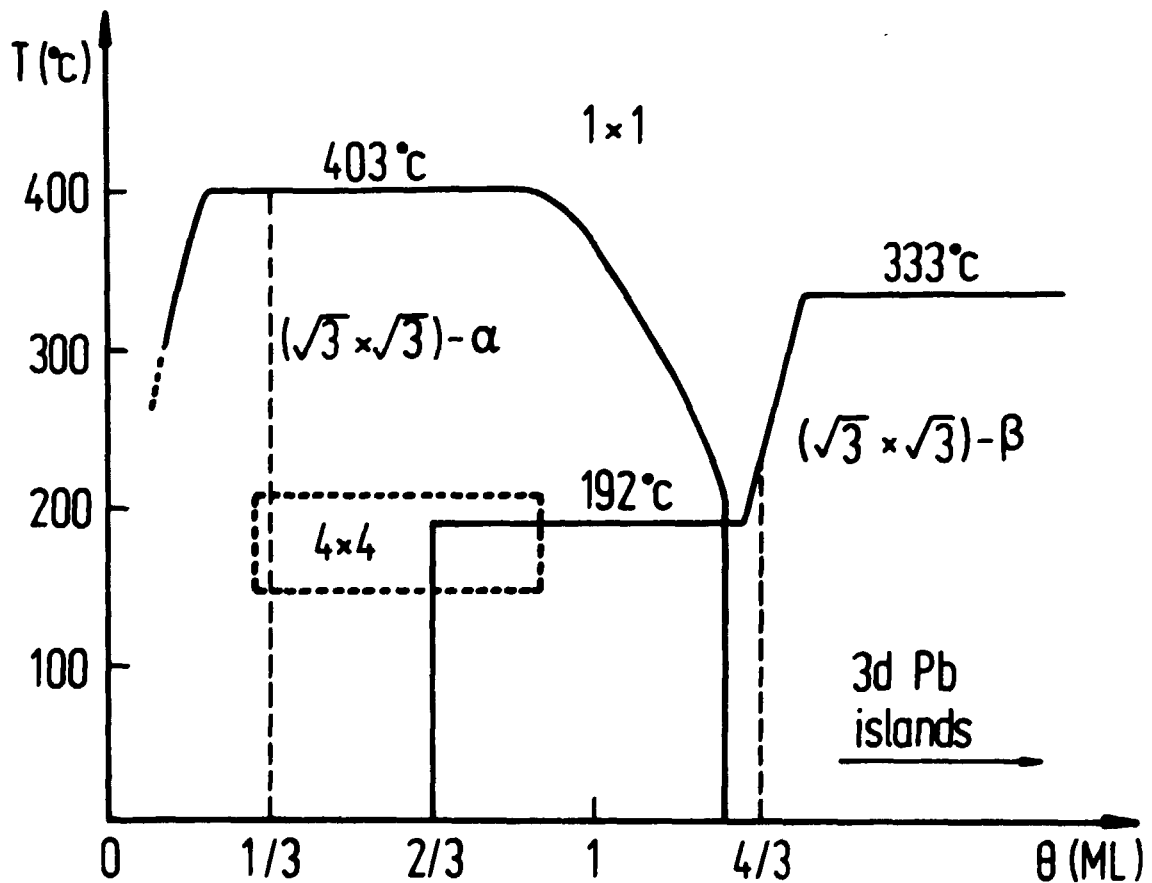


Fig. 1.6: Phase diagram of Pb/Ge(111) proposed by Ichikawa (ref. 13) on the basis of RHEED measurements.

Besides a metastable 4×4 phase during the first anneal, two phases are again found as a function of coverage the α (dilute) phase and the β (dense) phase. Ichikawa proposes the same model for the β -phase as Estrup and Morrison (Fig. 1.4b). On the basis of the phase diagram, Ichikawa proposes a model of the α -phase with $\theta = 2/3$ (ie two atoms per $\sqrt{3}$ unit cell), which is essentially the model of Fig. 1.4c with the atom marked 3 missing. The α -phase undergoes a transition to a 1×1 phase with weak diffuse $\sqrt{3}$ reflections at around 400°C . The β -phase $\rightarrow 1 \times 1$ transition at 192°C was the subject of a separate study (ref. 14). Ichikawa interprets weak, isotropic halos of diffuse scattering in the 1×1 phase as the two-dimensional analogue of diffraction halos seen from 3d liquids. Based on the isotropy of the halos, Ichikawa proposes that the the 1×1 phase is a 2d liquid unperturbed by the substrate.

Tonner et al. (ref. 15,16) have made angle-resolved photoemission measurements of the valence band of the β -phase of Pb/Ge(111). They interpret their data in terms of the model proposed by Metois and Le Lay, with only one type of adsorption site (Fig. 1.4c). It should be noted that this is only a $\sqrt{3}$ structure if inequivalent relaxations of the Pb atoms are invoked. The same model has recently been used by Le Lay et al. for the dense phase of Pb/Si(111) (ref. 17). Other investigations favour the β -phase model for the dense phase of Pb/Si(111) (ref. 18).

The main discrepancy between the various studies so far concerns the coverages at which the two phases are completed. This is in fact a fundamental problem for studies of phase diagrams in the monolayer regime. Few coverage sensitive techniques are accurate to less than 10%. Rutherford Back-Scattering (RBS) measurements, which can achieve a few percent accuracy, have not yet been made on this surface. With the exception of Metois and Le Lay, investigators have used the structural models to define the coverage scale. If this is to be done accurately, detailed structural information is needed. This is provided by the analysis of surface X-ray diffraction data.

Feidenhans'l et al. (ref. 6) and Skov Pedersen et al. (ref. 7), have determined the room-temperature structures to be very similar to the original proposal of Estrup and Morrison for Pb/Si(111), namely a dilute α -phase at $\theta = 1/3\text{ML}$ and a dense β -phase with $\theta = 4/3\text{ML}$. At intermediate coverages, the data can be accounted for by an incoherent sum of the structure factors for the two phases, implying phase separation. From the surface diffraction measurements, it is possible to deduce the relaxations of the Pb atoms and subsurface Ge layers, as well as the registry of the two phases on the (111) surface (see Fig. 1.7).

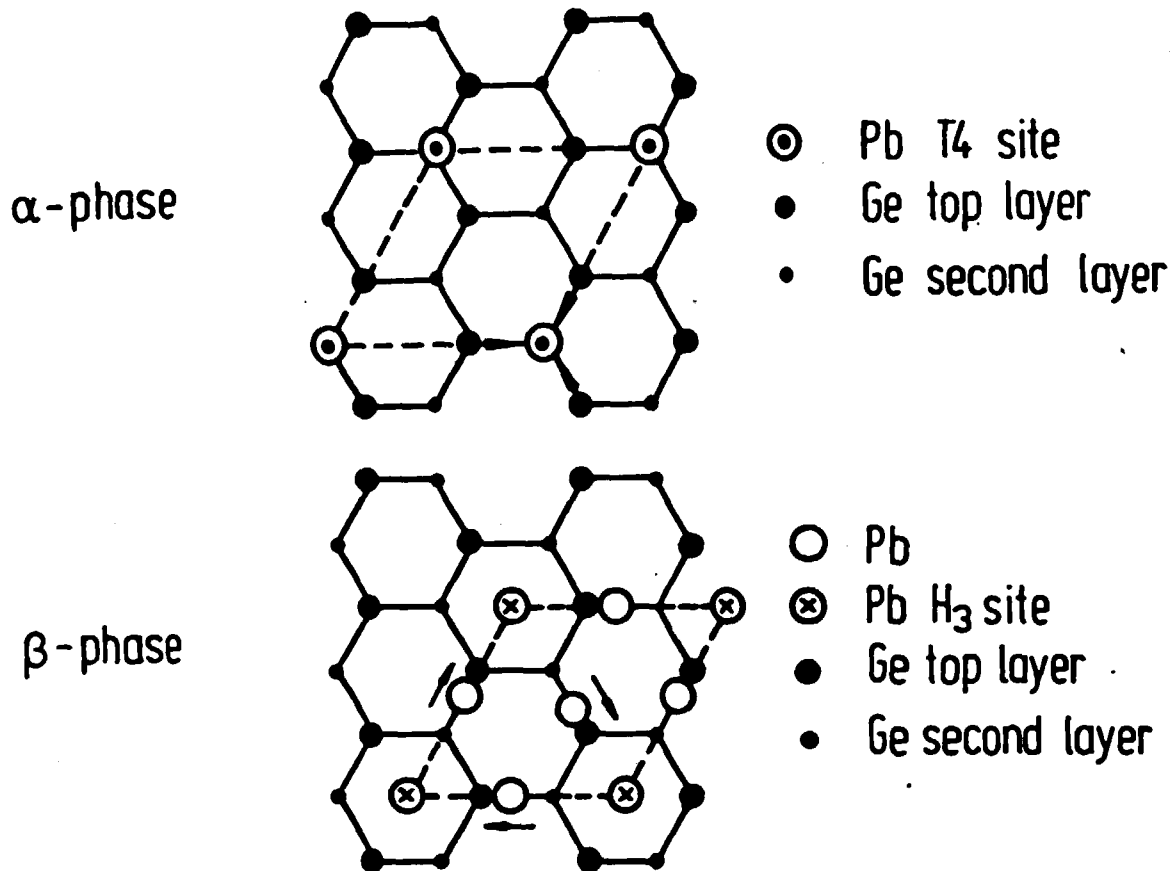


Fig. 1.7: The α and β -phases of Pb/Ge(111). Arrows indicate direction of in-plane relaxation of those Pb atoms not on high symmetry sites in the β -phase.

The α -phase has T₄ registry, which has also been proposed for the simple $\sqrt{3}$ structures of Al, Ga and In on Si(111) (ref. 9). In the β -phase, only one atom per unit cell occupies a high symmetry site, and this is found to be H₃. In other words, the β -phase cannot be obtained from the α -phase by simply filling in the interstitial positions: there is a change of chemisorption site between the two phases.

Two objections have been raised against the β -phase model. The first is that, since the β -phase forms a distorted close-packed layer with a 1% mismatch to a (111) Pb layer, island growth on this layer should proceed epitaxially with Pb($\bar{1}\bar{2}1$)||Ge($1\bar{1}0$) (ref. 15). This argument underestimates the complexity of the crystallite nucleation process since, for example, steps and defects may play an equally important role in determining growth orientation (ref. 19). Very recently, Li and Tonner (ref. 20) have made a detailed LEED investigation of Pb/Ge(111). They do not perform a quantitative analysis of their data, and therefore the work is rather inconclusive. They do note, however, that beyond 5ML, Pb islands

rotated $\pm 4^\circ$ to the $(1\bar{1}0)$ axes appear, indicating that the growth process is rather more complex than previously assumed.

The second objection to the β -phase is that it does not agree with the saturation coverage as determined by microbalance measurements (ref. 12). Two explanations are available: one is that the adsorption characteristics of the microbalance and of the Ge(111) surface may be different. The second is that, even at saturation coverage of the dense phase, there may be low density regions on the surface with only short-range order. These would not noticeably affect the surface diffraction measurements. To clarify this point two measurements could be helpful: RBS to determine the saturation coverage, and Scanning Tunneling Microscopy to determine the degree of order in the dense structure.

1.3 References

1. A recent review with 334 references is given by E. Bauer in "Structure and Dynamics of Surfaces Vol. II", eds. W. Schommers, P. von Blanckenhagen (1987) Springer Verlag; see also: W. N. Unertl, Comments Cond. Matt. Phys. 12, p. 289-323, (1986).
2. M. G. Lagally, T. M. Lu and D. G. Welkie, J. Vac. Sci. Technol. 17, p. 223-230 (1980).
3. K. Christmann, R. J. Behm, G. Ertl, M. A. Van Hove, W. H. Weinberg, J. Chem. Phys. 70, p. 4168-4184 (1979).
4. S. Brennan, P. H. Fuoss, P. Eisenberger, Phys. Rev. B33, p. 3678-3683 (1986).
5. M. Hansen, Constitution of Binary Alloys, p. 771 (1958) McGraw Hill.
6. R. Feidenhans'l, J. S. Pedersen, M. Nielsen, F. Grey, R. L. Johnson, Surf. Sci. 178, p.927-933 (1986).
7. J. S. Pedersen, R. Feidenhans'l, M. Nielsen, F. Grey, R. L. Johnson, Surf. Sci. 189/190 p. 1047-1054 (1987).
8. P. H. Kleban in Chemistry and Physics of Solid Surfaces V, eds. R. Vanselow and R. Howe, p.339-363 (1984) Springer Verlag.

9. J. M. Nicholls, B. Reihl, J. E. Northrup, Phys. Rev. B35, p. 4137-4140 (1987).
10. M. Schick, Physica, 109 & 110B p.1811-1818 (1982).
11. P. J. Estrup, J Morrison, Surf. Sci. 2, p. 465-472 (1964).
12. J. J. Metois, G. Le Lay, Surf. Sci. 133, p. 422-442 (1983); see also: G. Le Lay, J. J. Metois, Appl. Surf. Sci. 17, p. 131-135 (1983) G. Le Lay, Z. Imam, Surf. Sci. 154, p. 90-98 (1985).
13. T. Ichikawa, Sol. Stat. Comm. 46, p. 827-831 (1983).
14. T. Ichikawa, Sol. Stat. Comm. 49, p. 59-64 (1984).
15. B.P. Tonner, H. Li, J. Robrecht, Y. C. Chou, M. Onellion, J. L. Erskine, Phys. Rev. B34, p. 4386-4389 (1986).
16. B.P. Tonner, H. Li, J. Robrecht, M. Onellion, J. L. Erskine, Phys. Rev. B36, p. 989-997 (1986).
17. G. Le Lay, J. Peretti, M. Hahnuecken, W. S. Yang. Surf. Sci. 204, p. 57-68 (1988).
18. M. Saitoh, K. Oura, K. Asano, F. Shoji, T. Hanawa, Surf. Sci. 154, p. 394-416 (1985).
19. J. A. Venables, G. D. T. Spiller, M. Hahnuecken, Rep. Prog. Phys. 47, p. 399-459 (1984).
20. H. Li, B. P. Tonner, Surf. Sci. 193, p.10-23 (1988).

2. SURFACE X-RAY DIFFRACTION: THEORY AND EXPERIMENT

Surface X-ray diffraction is a powerful technique for structure determination on the atomic scale. The reason is that the data analysis is based on a simple kinematical scattering theory, discussed in section 2.1. The surface X-ray diffraction experiments discussed in this report are performed in the grazing incidence geometry, to enhance the surface signal-to-noise ratio, as explained in section 2.2. The Pb/Ge(111) sample preparation and characterization and the typical surface diffraction measurement procedure is described in sections 2.3 and 2.4, respectively. As an illustration of the technique, we present the analysis of room-temperature studies of Pb/Ge(111) at six different coverages in section 2.5. The structural information obtained from these studies is employed throughout the rest of the report.

2.1 Kinematical Scattering Theory

The scattering geometry in a surface diffraction experiment is shown in Fig. 2.1. The scattered electric field amplitude as a function of scattering vector q is (ref. 1):

$$E(q) = E_0 \frac{r_0}{R} \int_{-\infty}^{\infty} \rho(r) e^{iq \cdot r} dr \quad (2.1)$$

E_0 : incident E-field amplitude.

r_0 : classical electron radius = $2.82 \times 10^{-15} \text{m}$

R : distance from sample to detector

$\rho(r)$: electron density in units of electron charge

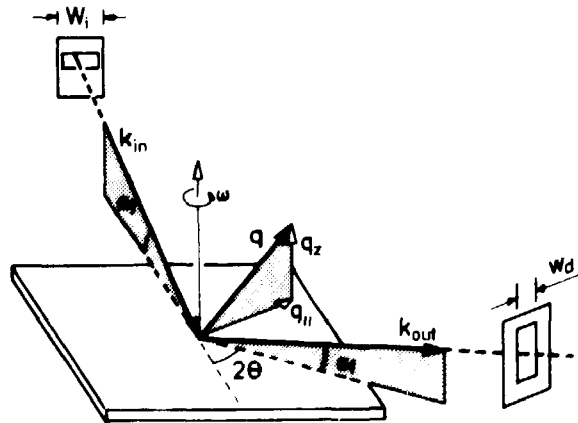


Fig. 2.1: Scattering geometry in surface diffraction. k_{in} and k_{out} are the incident and scattered wavevectors. $q = k_{out} - k_{in}$ is the scattering vector, $q_{||}$ and q_{\perp} are its in-plane and normal components. 2θ is the in plane scattering angle. α_i and α_f are the incident and detection angles. The slit arrangement is indicated.

Usually only relative amplitude variations are of interest. Setting $E_0 = 1$, the scattered amplitude normalized to units of electron scattering is

$$A(q) = f(\rho(r)) \quad (2.2)$$

Where f denotes Fourier transformation. This Fourier relationship between scattered amplitude and electron density is applicable under two conditions: multiple scattering is negligible (Born approximation), and the detector is in the far-field (Fraunhofer diffraction). For illustrative simplicity we will consider a 1-d lattice of atoms with lattice constant a_0 ; the results can be easily generalized. It is convenient to break $\rho(x)$ up according to the physically interesting length scales: atom, unit cell, crystal. For a finite crystal, the electronic distribution can then be written:

$$\rho(x) = \rho_A(x) \otimes \sum_j \delta(x-x_j) \otimes \sum_{n=-\infty}^{\infty} \delta(x-na_0) \cdot h(x) \quad (2.3)$$

$\rho_A(x)$: electron density of individual atom A
 x_j : atomic positions in unit cell

where \otimes denotes a convolution product. The shape function $h(x)$ effectively terminates the infinite Dirac lattice. The Fourier transform is

$$A(q) = F(q) \sum_{n=-\infty}^{\infty} \delta(q-nq_0) \otimes f(h(x)) \quad (2.4)$$

$F(q)$: structure factor = $f_A(q) \sum e^{iqx_j}$
 $f_A(q)$: atomic form factor
 q_0 : reciprocal unit vector = $2\pi/a_0$

In 2.4, the Dirac reciprocal lattice is convoluted with the Fourier transform of the shape function. Such convolution products are in general difficult to evaluate analytically. However, certain simple cases are tractable. A standard choice for $h(x)$ is a box function,

$$h(x) = 1 \text{ for } |x| \leq Na_0/2 \quad (2.5)$$

$$h(x) = 0 \text{ for } |x| > Na_0/2$$

Hence, in Eqn. 2.3

$$\sum_{n=-\infty}^{\infty} \delta(x - na_0) \cdot h(x) = \sum_{n=-N/2}^{N/2} \delta(x - na_0) \quad (2.6)$$

and Fourier transformation leads to the phase factor sum:

$$\sum_{n=-N/2}^{N/2} e^{iqna_0} = \frac{\sin(Nqa_0/2)}{\sin(qa_0/2)} \quad (2.7)$$

In Eqn. 2.7, $\sin(Nqa_0/2)$ is a rapidly oscillating function due to interference from the crystal edges, while $1/\sin(qa_0/2)$ is an envelope function which diverges at the reciprocal lattice points. Between Bragg reflections the average scattering is of the order of that due a single atom (or, in the 3d case, due to a single atomic layer).

Due to a number of experimental effects, the measured line shape of a Bragg reflection does not usually have the functional form of Eqn. 2.7. For example, a real measurement may average over a large number of domains of different sizes and shapes. For a random distribution of domain sizes, the line shape is often quoted as (ref. 1):

$$W(\Delta q) = N \exp \left[- \frac{(Na_0 \Delta q)^2}{8 \pi} \right] \quad (2.8)$$

Δq : distance from Bragg peak = $(q - nq_0)$

In both 2.7 and 2.8, the width of the reflection gives the domain size:

$$\Delta q_{FWHM} \approx 4\pi / Na_0 \quad (2.9)$$

In practice, finite resolution of incident and diffracted beams will affect the measured width. However, the integrated intensity of a Bragg reflection can be shown to be proportional to the structure factor intensity $|F(q)|^2$ (ref. 1). This is the starting point for experimental crystallographic structure determination.

Because X-ray diffraction measurements determine only the amplitude of the structure factor and not the phase, Fourier inversion of the measured structure factor intensities does not yield the real space structure of the unit cell. What it does yield is

$$f^{-1}(F(q) \cdot F^*(q)) = \frac{1}{2\pi} \rho(x) \otimes \rho(-x) \quad (2.10)$$

which is the self-convolution of the crystal electron density. This function provides a map of the interatomic vectors in the unit cell, but not of the absolute coordinates.

Bragg rods: A two-dimensional crystal in the x-y plane can be thought of as the limit of a three dimensional crystal with $N_z = 1$ in Eqn. 2.7. The scattered amplitude as a function of q_z is then simply proportional to the structure factor. Thus there are no sharp Bragg peaks due to periodicity, but instead a Bragg rod, modulated only by the structure factor (see Fig. 2.2). A surface with a superstructure (periodicity

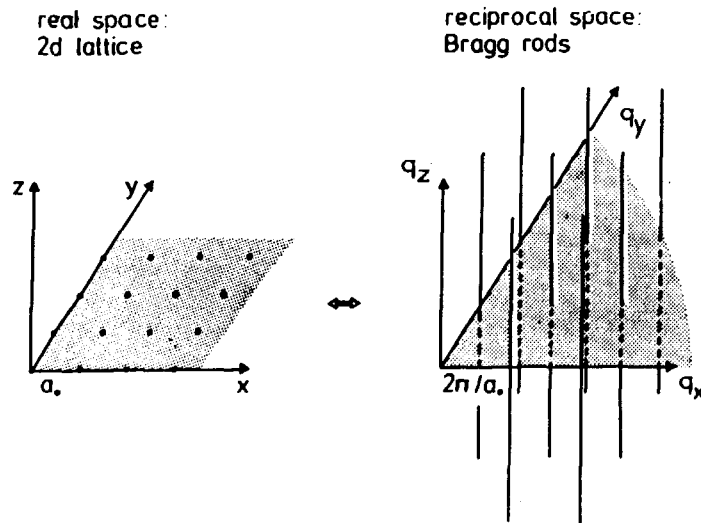


Fig. 2.2: Sketch of 2d lattice and its Fourier transform, an array of Bragg rods.

larger than that of the underlying crystal) will give rise to extra Bragg reflections with fractional Miller indices. Although several layers below the surface may be perturbed by the new surface periodicity (subsurface relaxation) the superstructure is not periodic perpendicular to the surface, and thus also produces Bragg rods.

Bulk termination rods: Diffraction from the flat surface of a semi-infinte crystal is an example where the mathematically sharp edge of a shape function is of physical consequence. The shape function of interest is:

$$h(z) = e^{-\mu z} \text{ for } z \geq 0 \quad (2.11)$$

$$h(z) = 0 \text{ for } z < 0$$

Here an absorption factor has been included to account for damping of the incident and scattered beams. As for the box function, the transform is an easily evaluated geometrical series:

$$\sum_{n=0}^{\infty} e^{-\mu z} e^{i q z} \underset{\mu \rightarrow 0}{=} -\frac{i}{2} e^{i q a_0 / 2} \left(\frac{1}{\sin (q a_0 / 2)} \right) \quad (2.12)$$

This long tail of scattering between bulk reflections is called a bulk termination rod. For a perfect crystal, and in close vicinity of the Bragg reflection, Eqn. 2.1 is no longer valid, because multiple scattering becomes appreciable. We note that the result has the same form as the envelope function of scattered amplitude from a small crystal. This is because a step function is the limiting case of a box function as one edge is taken to infinity, as sketched in Fig. 2.3.

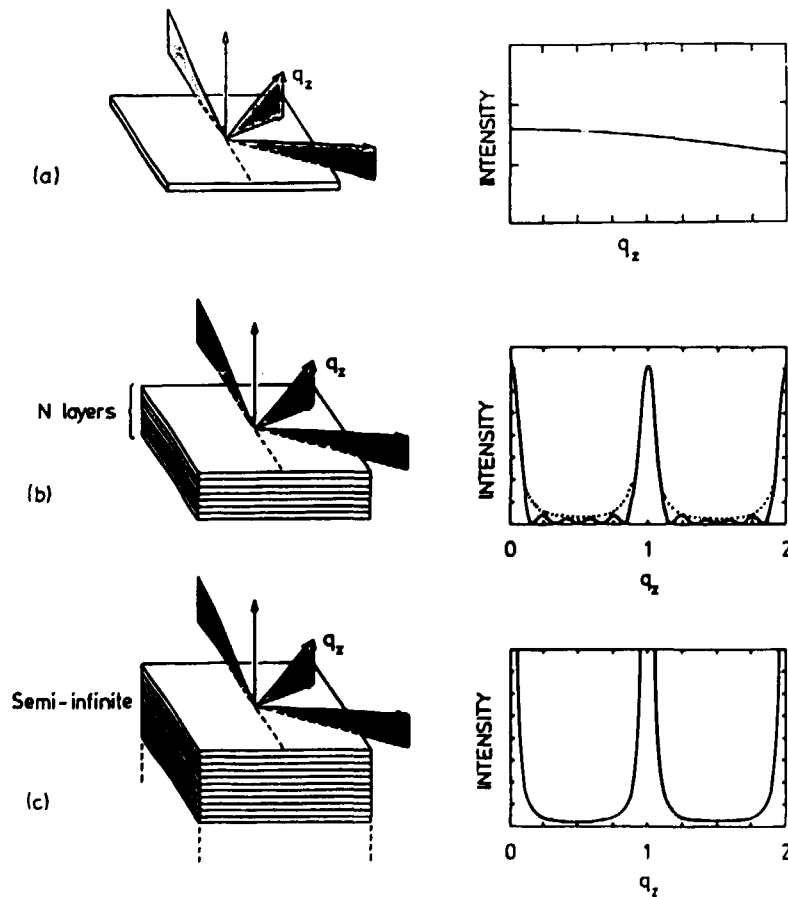


Fig. 2.3: Schema of the scattering from (a) one layer (b) N layers and (c) a semi-infinite crystal.

The scattering between Bragg points for a semi-infinite 3d crystal, along the crystal-normal direction, is comparable with that from a single monolayer, and therefore significant in surface X-ray diffraction experiments. The point to retain is that the sharp edge of the shape function (small extension in real space) leads to broad tails of scattering about the Bragg peaks (large extension in reciprocal space).

Registry: It is convenient to think of a crystal with a surface superstructure as the sum of a surface layer with the periodicity of the superstructure and an undistorted bulk crystal, even though the depth at which superstructure stops and bulk crystal begins is somewhat arbitrary. For any $n \times m$ superstructure, with n, m integer, some Bragg rods from the superstructure will coincide with bulk termination rods. The atomic geometry of the superstructure can be determined by analysis of the fractional order reflections only. The integer order reflections are the coherent sum of Bragg rod and bulk-termination rod, the phase relationship between the two being determined by the registry of the superstructure on the bulk lattice. The total structure factor can be written:

$$F_{\text{tot}}(h, k) = F_{\text{bulk}} + F_{\text{surf}} e^{i2\pi(hx + ky)} \quad (2.13)$$

F_{bulk} : bulk termination rod contribution

F_{surf} : surface Bragg rod contribution

where h, k are the in-plane Miller indices and (x, y) is the displacement of the origin of the overlayer relative to the origin of the bulk crystal structure. In practice, only those (x, y) corresponding to high-symmetry registry of the overlayer are considered. If both the surface and bulk structures are known, the problem is that of comparing the calculated structure factor intensities for different registries with experiment.

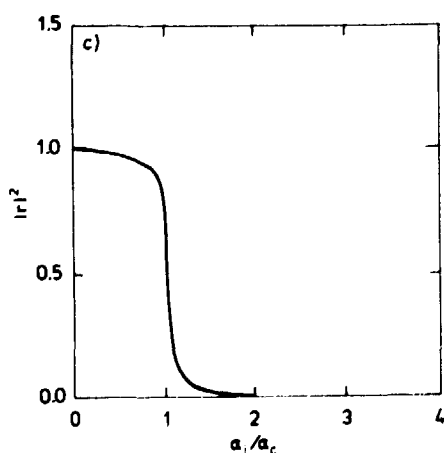
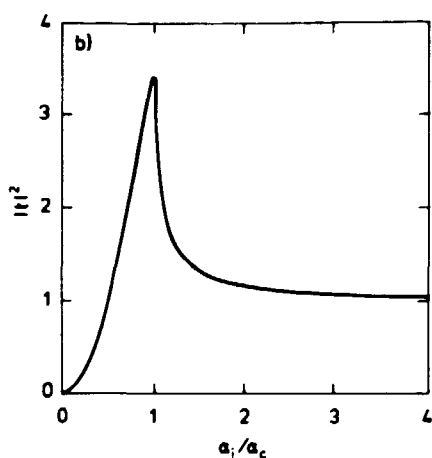
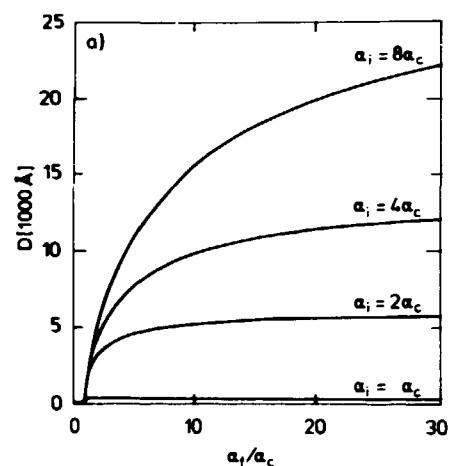
2.2 Grazing Incidence Geometry

At small angles of incidence (α_i) to a surface, the penetration depth D of X-rays is greatly reduced for two reasons. One is the purely geometrical factor $\sin(\alpha_i)$ due to the variation of distance travelled perpendicular to the surface per unit distance travelled in the material. The other is a consequence of the fact that for X-rays, the refractive index n of a material is slightly less than 1:

$$n^2 = 1 - \delta \quad (2.14)$$

$$\delta = 8.98 \times 10^{-6} N_0 Z \lambda^2 \quad (2.15)$$

N_0 : number of atoms per \AA^3
 Z : number of electrons per atom
 λ : wavelength in \AA



Below the critical angle α_c , where $\alpha_c = \sqrt{\delta}$, the incident beam is totally reflected and the refracted beam becomes inhomogeneous, with an exponentially decaying profile perpendicular to the surface (ref. 2). To illustrate this, the penetration depth D (at which the intensity has decayed by $1/e$) is calculated in Fig. 2.4a for Ge at $\lambda = 1.3 \text{\AA}$, for various incidence angles α_i and as a function of exit angle α_f . Clearly, working with incidence angles near the critical angle (grazing-incidence geometry) limits the penetration depth, and hence reduces the unwanted diffuse scattering from the bulk considerably. An additional benefit of working exactly at the critical angle is an enhancement of the refracted amplitude at the surface. This is a simple result of the Fresnel equations of optics (ref. 2), and is illustrated in Fig. 2.4b,c, again for Ge at $\lambda = 1.3 \text{\AA}$.

Fig. 2.4a-c:
 (a) penetration depth D of X-rays as a function of exit angle α_f , for different incidence angles. Squared amplitude of (b) transmission and (c) reflection coefficients of a flat surface. All curves calculated for Ge and X-rays of $\lambda = 1.3 \text{\AA}$; absorption is included.

2.3 Sample Preparation and Characterization

Ge single crystals were cut, polished and etched at the Max Planck Institute, Stuttgart. The optical surface was aligned to better than 0.1° with the crystallographic (111) plane, as determined by X-ray diffraction measurements.

The UHV sample preparation was carried out at the Flipper II photoemission system in HASYLAB (Fig. 2.5). The Ge sample, dimensions $3 \times 10 \times 10 \text{ mm}^3$, was mounted on a holder such that the backside of the sample made pressure contact with a W/Rh 25%/3% thermocouple. (Fig. 2.6). The sample was heated by passing current directly through it, molybdenum clamps acting as electrical contacts. After outgassing at 700° C , the sample surface was cleaned by 3-4 sputter anneal cycles, each cycle consisting typically of 1 hour sputtering with 500 eV Ar^+ ions, 3 hours annealing at 700° C , and cooling at $< 10^\circ \text{ C/minute}$.

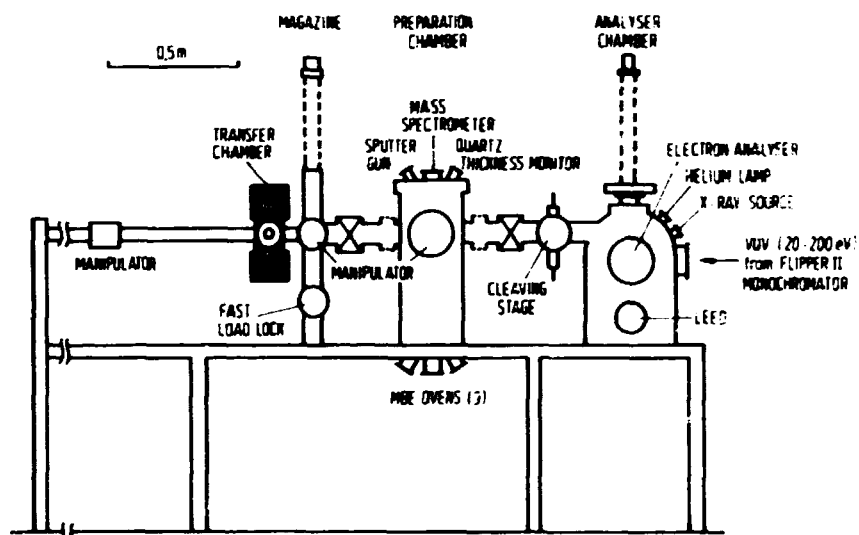


Fig. 2.5: Side view of the Flipper II photoemission system in HASYLAB.

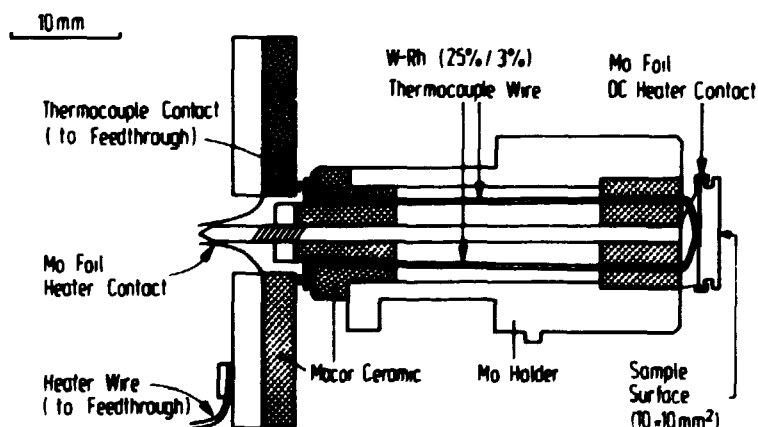


Fig. 2.6: Sample holder with thermocouple (cross-section). Also shown is the clamp used to fix the sample holder during measurements.

After this treatment, a LEED (2×8) pattern was seen, characteristic of the clean Ge surface. The $1/8$ spots were weak and sometimes streaky, apparently an intrinsic property of this surface. Pb was evaporated at a rate of 0.2-0.5 ML/minute from a boron-nitride crucible onto the clean Ge(111) (2×8) surface at room temperature. The deposition rate was monitored by a quartz oscillator. The LEED $\sqrt{3} \times \sqrt{3} R30^\circ$ pattern was visible directly after deposition, although annealing the sample at 250° C for two minutes visibly sharpens the LEED spots.

Photoemission Measurements: Synchrotron photoemission measurements at Flipper II enable a rapid characterization of the sample. The proximity of the Pb5d and Ge3d outer core levels in a photoemission spectrum provides a particularly convenient means of calibrating the coverage. After completion of the β -phase, the 5d/3d intensity ratio remains practically constant up to much higher coverages (~ 10 ML) at which the 3d Pb islands start to occupy a significant fraction of the surface area. Thus the typical β -phase spectrum can be easily determined and is shown in Fig. 2.7. The coverage of the other spectrum in Fig. 2.7 was determined by surface diffraction to be $\theta = 0.33$, that is, a pure α -phase.

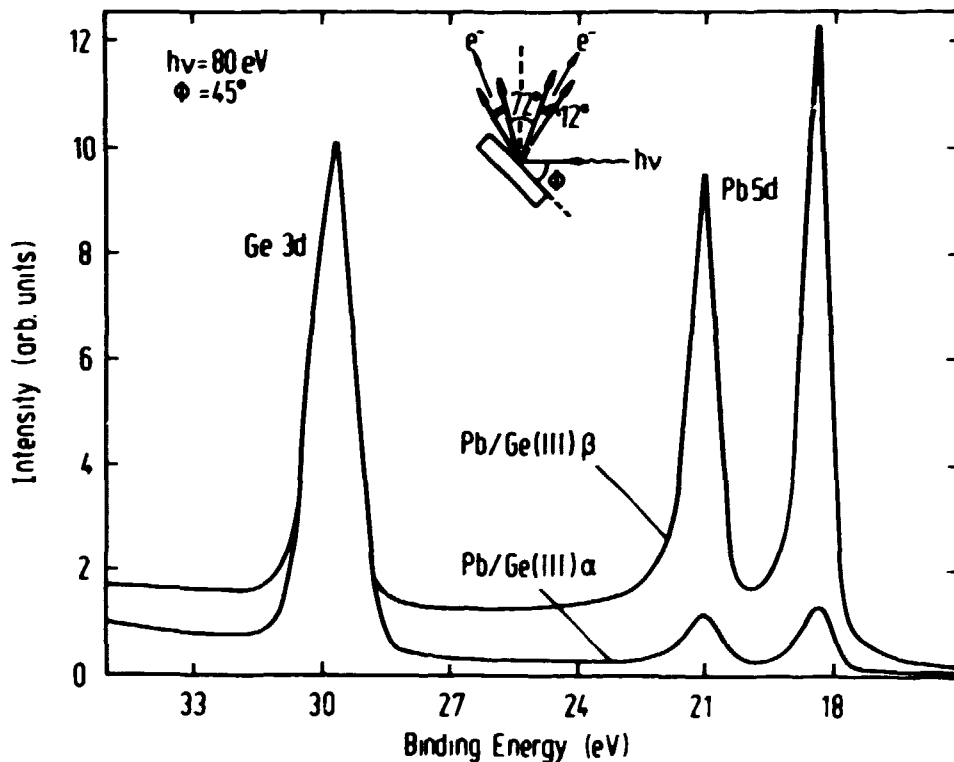


Fig. 2.7: Electron Distribution Curve (EDC) of the outer core levels of Pb and Ge for the α and β -phase of Pb/Ge(111) at a photon energy of 80 eV. Inset shows collection geometry of the cylindrical mirror analyser at Flipper II. Φ is the angle of incidence.

It is reasonable, in the monolayer regime, to assume a linear rather than exponential damping of the incident beam due to the adsorbed species, since the intensity lost from the forward beam is determined not by the film thickness, but by the area effectively blocked by Pb atoms. On this basis, a simple expression for the transmitted intensity is:

$$I_t = I_0 (1 - \theta\mu) \quad (2.15)$$

I_0 : incident intensity

θ : coverage

μ : absorption coefficient

If the absorption of the Pb layer were negligible ($\mu=0$) then the ratio of the integrated intensities of the Pb5d and Ge 3d peaks, I_{5d}/I_{3d} , would be simply proportional to coverage, and $(I_{5d}/I_{3d})_{\beta}/(I_{5d}/I_{3d})_{\alpha} = 4$.

From the measurements in Fig. 2.7, the ratio is 8.3, corresponding to $\mu=0.44$. The value of μ can be estimated theoretically, using the ideal coverages of the α and β -phase and tabulated cross-sections of Pb at 80eV (ref. 3). The result is $\mu=0.29$; the difference between theoretical and calculated μ arises because the effect of the Pb layer on the emitted Ge photoelectrons has been neglected. Effects such as scattering, refraction and photoelectron diffraction are important, and coverage-dependent. The larger experimental value of μ implies that the β -phase is more effective at stopping the Ge photoelectrons, which is reasonable. For the purposes of coverage calibration, the experimental value of μ is adequate, and we do not pursue the complexities of photoelectron emission here.

Photoemission results in the monolayer regime allow a calibration of the quartz oscillator. It is then possible to estimate the coverage beyond $4/3ML$, where growth proceeds by 3d islands. This estimate assumes that the deposition rate is the same for the β -phase as for the islands, which may be reasonable at room temperature (everything sticks) but is probably not true for deposition on hot substrates.

Valence band spectra for the clean Ge(111)c(2x8) surface, the α and β -phases are shown in Fig. 2.8. Caution must be observed when interpreting the features in such spectra, since they are only partially angle-integrated by the cylindrical mirror analyser (acceptance geometry shown in inset of Fig. 2.7) and thus sensitive to the choice of incidence angle. Nevertheless, it is possible to explain the differences between the spectra of the clean c(2x8) surface and the α -phase in Fig. 2.8,

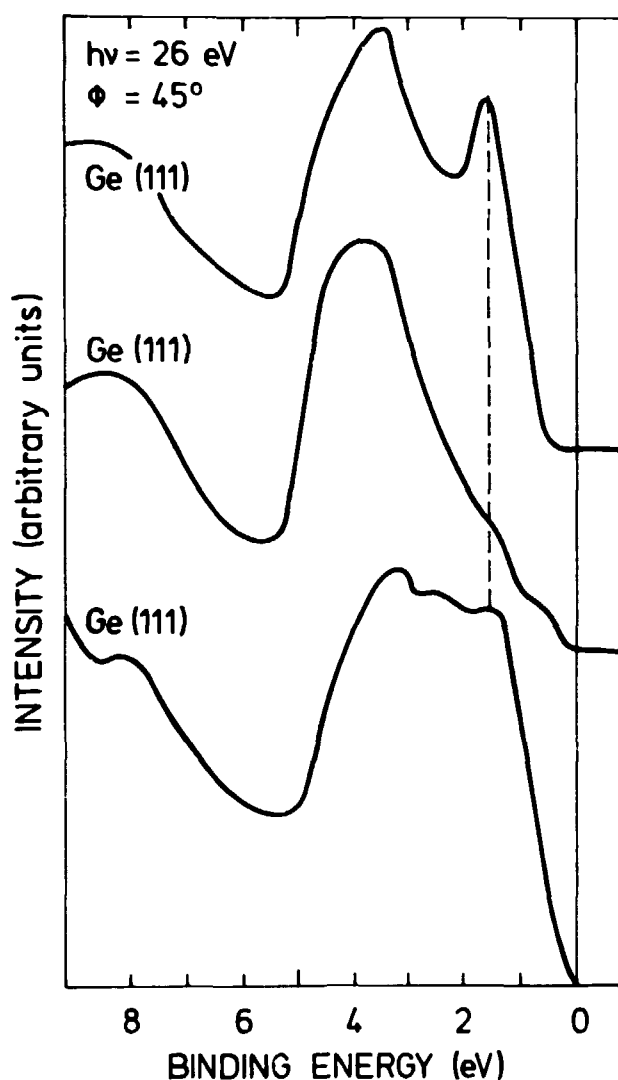


Fig. 2.8:
EDCs of the valence band of
Ge(111)c2x8, and the α and β -
phases of Pb/Ge(111) at a photon
energy of 26 eV.

by comparison with angle-resolved photoemission studies. The strong feature 1.5 eV below the Fermi level E_f for the clean c(2x8) surface corresponds to an intense, near-dispersionless surface band at 1.4 eV (width 0.2 eV) that has been associated with adatom dangling bonds (ref. 4). For the $\sqrt{3}$ structure of Sn/Si(111) (ref. 5) and $\sqrt{3}$ structures of group III elements on Si(111) (ref. 6), there is also a band centred at about 1.5 eV, but it has much larger dispersion (width 1.0 eV for Sn/Si(111)) and is weak at exit angles sampled by the analyser. Thus the comparatively weak featureless top of the valence band for the α -phase is compatible with a band structure similar to that of the simple (one-atom per unit cell) $\sqrt{3}$ structures of Sn, In, Ga and Al on Si(111). In the valence band of the β -phase, there is again considerable intensity at 1.2 eV below the top of the valence band. This agrees with angle-resolved measurements (ref. 6), which find an intense band 1.3 eV below the Fermi level.

2.4 Measurement Procedure

A detailed description of the steps involved in a typical surface X-ray diffraction experiment has been given elsewhere (ref. 7). Here we will summarize the salient points.

Transfer Chamber and Wiggler Beamline: After preparation and characterization by LEED and photoemission, the sample is transferred to a transportable vacuum chamber (Fig. 2.9). The chamber is disconnected from Flipper II (Fig. 2.10a) and mounted on a 2-axis vertical-scattering X-ray diffractometer at the wiggler line W1 (Fig. 2.10b). A base pressure of 1×10^{-10} mbar is maintained throughout the experiment. The wiggler beam is monochromated by two Ge(111) crystals; typically a wavelength of 1.3-1.5 Å is chosen. The beam is focussed by a Au-coated mirror 20m upstream from the experiment, to gain extra intensity. The intensity in the beam is estimated to be 10^{13} photons/cm²/sec, or about 10^5 more than a 12kW rotating anode (ref. 7). Theoretically the beam is roughly 90% polarized in the horizontal plane (ref. 8), and so the polarization factor for vertical scattering is (ref. 1)

$$P(2\theta) = 0.9 + 0.1 \cos^2 2\theta \quad (2.16)$$

Alignment: For alignment and measurement, a Position Sensitive Detector (PSD) is used, subtending 4° perpendicular to the surface and 0.8° in the surface plane. An ionization chamber monitoring the incident beam is used to normalize the scattered intensity to the incident flux. A cross beam area on the sample of size $(w_i \times w_d / \sin 2\theta)$ mm² is defined by slits of width w_i and w_d on the the incident and diffracted beams, respectively, 2θ being the detector rotation angle (see Fig. 2.1). The total externally reflected beam from the sample surface is monitored as a function of sample rotation (ω), and the sample goniometer (Fig. 2.10b) is adjusted so that the total reflected beam remains the same for all ω . When this is done, the normal of the optical surface is aligned along the ω axis, and the angle of incidence α_i can be varied using the tilt-table. For optimum intensity, α_i is set to the critical angle of the substrate. However, for optimum reproducibility, it is better to work at an incidence angle of $2-3\alpha_c$, where the scattered intensity is much less sensitive to slight misalignment. After orienting the reciprocal space of the sample by measuring the in-plane bulk Ge reflections, the surface reflections can be measured. Uniformity of coverage across the surface can be judged by translating the sample relative to the beam while measuring a surface reflection. Over the central region of the sample (7×7 mm²) an upper limit on coverage non-uniformity of 5% is typical.

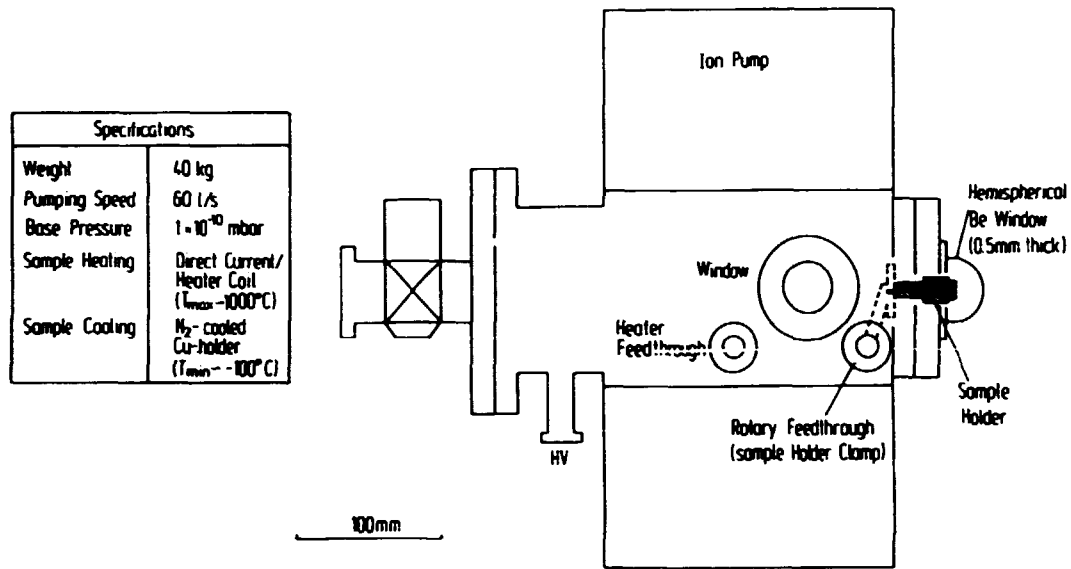


Fig. 2.9: The UHV transfer chamber used for most of the phase transition measurements discussed in this report. Not shown are feedthroughs for thermocouple and heater (other side of chamber).

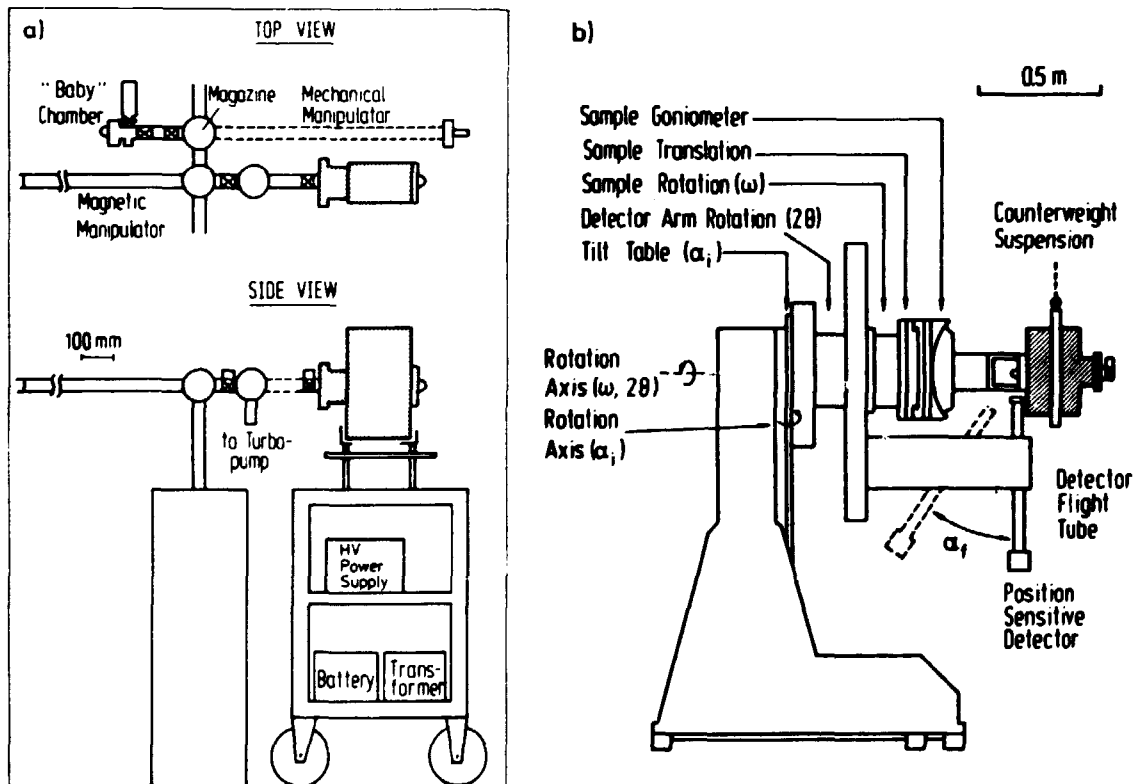


Fig. 2.10a, b: (a) Transfer chamber at Flipper II (see also Fig. 2.5). (b) Transfer chamber mounted on the 2-axis diffractometer at the wiggler beamline W1 in HASYLAB. The beam direction is out of the page.

Temperature calibration: The thermocouple and heating arrangement of Fig. 2.6 is chosen within the constraints set by the sample preparation and transfer technique and by the requirement of easy access to the sample surface for diffraction studies. The solution is thus not necessarily optimal for temperature-dependent studies. However, experience shows that the thermal characteristics of this sample/thermocouple arrangement are quite satisfactory. The temperature was stabilized by a thermocontroller to 0.1°C on a relative scale. Uniformity of temperature over the central region of the sample ($7 \times 7\text{mm}^2$) was better than 3°C for directly heated samples, as judged by translation scans of a surface reflection on approaching a steep surface phase transition. The absolute temperature is correct to $\pm 5^\circ\text{C}$ in the range $0\text{-}400^\circ\text{C}$ as judged by the reproducibility of standard transition temperatures (triple line in Pb/Ge(111) = 175°C , disordering of Cu_3Au = 390°C).

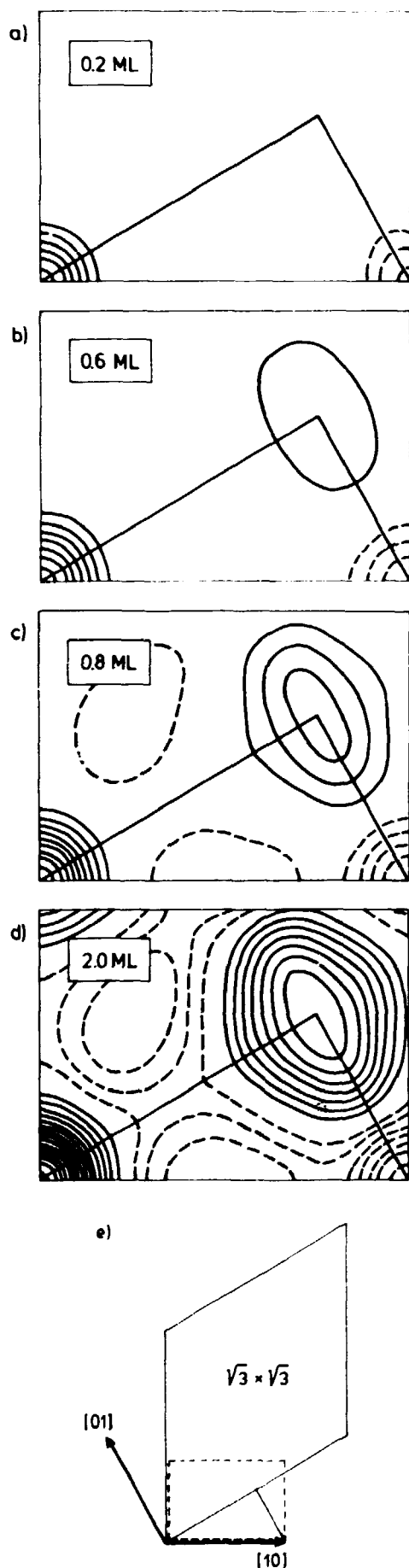
Data reduction: The steps to obtain a set of experimental structure factor intensities from the measured surface reflections are straightforward. The background-subtracted integrated intensities of sample rotation (ω) scans are corrected for two q -dependent factors, the cross beam area ($\propto 1/\sin 2\theta$) and the Lorentz factor ($\propto 1/\sin 2\theta$), the latter being a consequence of the particular integration path chosen in reciprocal space (ref. 1). For the innermost reflections, a further correction must be made because the cross-beam area stretches beyond the sample surface. No correction is made for the polarization factor. The errors on the structure factor intensities are estimated by combining quadratically the statistical errors of the individual integrated intensities with reproducibility errors between symmetry equivalent reflections. The statistical errors vary typically from $<1\%$ for the most intense reflections to 10% for the weakest. The errors determined by the reproducibility of symmetry equivalent reflections are 5-15%.

2.5 Structural Analysis of Pb/Ge(111)

Experimental fractional-order structure factor intensities for room-temperature measurements of Pb/Ge(111) are given in Table 2.1 (the data for $\theta = 0.33\text{ML}$ is from ref. 9, that for 0.6, 0.8 and 1.3 ML from ref. 10). The data has been put on a common scale after the analysis. The coverages are determined from the analysis and from photoemission measurements (0.2ML) and deposition rate calibration (2ML). Because the diffraction measurements do not yield the structure factor phases, it is not possible to determine the structure unambiguously from the data. However, a considerable amount of information about the surface structure

		0.2 ML		0.33 ML		0.6 ML		0.8 ML		1.3 ML		2 ML	
h	k	$ F_{exp} ^2$	σ_{exp}	$ F_{exp} ^2$	σ_{exp}	$ F_{exp} ^2$	σ_{exp}	$ F_{exp} ^2$	σ_{exp}	$ F_{exp} ^2$	σ_{exp}	$ F_{exp} ^2$	σ_{exp}
1/3	1/3	26.3	2.6	24.7	2.8	17.9	1.3	12.5	1.0	1.4	0.5	0.3	0.1
2/3	2/3	16.4	0.7	17.1	2.0	78.6	3.8	125.9	7.6	220.0	19.1	285.6	28.9
4/3	1/3	27.6	10.5	13.9	1.6	23.7	5.6	18.9	2.0	15.0	1.8	17.8	1.1
4/3	4/3	27.0	6.6	11.3	1.3	16.6	2.6	28.6	3.0	38.6	3.6	30.9	4.7
5/3	2/3	19.7	6.6	12.7	1.5	22.2	4.1	27.2	2.6	40.0	4.1	43.6	3.4
5/3	5/3	2.6	2.6	2.4	0.3	5.9	0.8	8.3	1.4	15.9	1.4	14.1	2.1
7/3	1/3	7.2	1.3	5.7	0.7	7.9	1.5	8.3	1.1	10.0	0.9	8.8	1.3
7/3	4/3	10.5	5.3	4.5	0.5	3.6	0.5	10.3	1.0	9.1	3.6	10.2	1.6
7/3	7/3									5.5	1.4	6.1	1.0
8/3	2/3	13.8	2.6	5.4	0.6	4.8	1.0	8.1	0.6	7.7	0.9	4.3	0.9
8/3	5/3			3.3	0.4							1.1	0.4
8/3	8/3			0.4	0.1								
10/3	1/3			3.7	1.5	4.6	0.8	1.9	0.4	1.6	0.3	1.7	0.3
10/3	4/3			2.2	0.3								
11/3	2/3			1.3	0.2	1.5	0.3	3.4	0.8	3.3	0.5	4.1	0.8
13/3	1/3			1.3	0.5								
Ba[A ²]		1.2±0.7		3.2±0.3		3.0±1.0		4.0±1.0					
Bβ[A ²]						5.0±1.0		4.0±1.0		4.0±0.5		4.1±0.5	
χ^2		1.3		0.6		2.2		4.6		1.5		4.0	

Table 2.1: Experimental structure factor intensities $|F_{exp}|^2$ and errors σ_{exp} for Pb/Ge(111). Coverages are determined from the structure factor analysis. The data is normalized to units of electron scattering and divided by 250. B-factors and χ^2 for the best-fit models are also given.



can be extracted from the data without reference to any model, by plotting the Patterson function, or electron density self-convolution. As shown in section 2.1, this is simply the Fourier transform of the measured structure factor intensities.

Patterson functions based on data for 0.2, 0.6, 0.8 and 2.0 ML are shown in Figs. 2.11a-d, for the irreducible unit of the Patterson function. Fig. 2.11e shows the relation between the irreducible Patterson unit (shaded) and the $\sqrt{3}$ unit cell. The contour levels are the same in each figure. At 0.2ML, a peak at the origin is the only significant feature, strongly suggesting only one Pb atom per unit cell. As the coverage increases, a peak builds up in the Patterson at the position of the midpoint of the side of the $\sqrt{3}$ unit cell. This feature corresponds to the nearest neighbour distance in a 2d close-packed structure. Only fractional order reflections are used to obtain the

Fig. 2.11 a-e:
 Patterson functions based on measured data. Dashed lines are negative contours. (e) shows the relation of the Patterson irreducible unit (shaded) to the $\sqrt{3}$ unit cell; the dashed rectangle is the region portrayed in (a-d). Pattersons for 0.33 and 1.3 ML (not shown) are nearly identical to (a) and (d), respectively.

Patterson function, since the integer-order reflections contain a contribution from the bulk termination rod. The absence of the integer-order reflections produces minima at the position of the [10] unit vector in all Pattersons.

With the models derived from the Patterson as a starting point, the structure is then refined by a least-squares fitting procedure. Goodness of fit is determined by a least-squares residual,

$$\chi^2 = \frac{1}{N-p} \sum_{c=1}^N \left(\frac{|F_{\text{exp}}|^2 - |F_{\text{calc}}|^2}{\sigma_{\text{exp}}^2} \right)^2 \quad (2.17)$$

- N: number of reflections measured
- p: number of fit parameters
- $|F_{\text{exp}}|^2$: experimental structure factor intensities
- $|F_{\text{calc}}|^2$: model structure factor intensities
- σ_{exp} : experimental uncertainties on $|F_{\text{exp}}|^2$

Ge atoms are relaxed in the subsurface layers to obtain good agreement. The 3 Pb atoms per unit cell not on high-symmetry sites in the β -phase (see Fig 1.7) are also allowed to relax. The only constraint imposed on the structural parameters is the projected 3m symmetry of the substrate. The non-structural fit parameters are an overall scale factor, and an isotropic X-ray Debye-Waller factor e^{-M} due to atomic thermal motion (ref. 1):

$$M = Bq^2 / 4\pi^2 \quad (2.18)$$

The room-temperature values of the B-factors for bulk Pb and Ge are $B_{\text{Pb}} = 2.2 \text{ \AA}^2$ (ref. 11), $B_{\text{Ge}} = 0.57 \text{ \AA}^2$ (ref. 12). The relaxations of the atoms for the best fit models of the α and β -phase are summarized in Table 2.2. Several other structural models were tested, but none were remotely as successful as those presented here.

Phase	Atom	In-plane relaxation	Direction
α	Ge 1st layer	0.046 ± 0.005	Towards Pb at T_4
	Ge 4th layer	0.020 ± 0.004	away from Pb at T_4
β	Pb "interstitial" sites	0.1 ± 0.03	See Fig.1.7
	Ge 1st layer	0.014 ± 0.006	away from Pb at H_3

Table 2.2: In-plane relaxations of α - and β -phases. Amplitudes are quoted in units of the [10] surface lattice vector, $[10] = a_s/\sqrt{2} = 4.00 \text{ \AA}$. Pb atoms on high-symmetry sites are not relaxed in-plane.

At coverages between 1/3 and 4/3 ML, the diffraction data is reproduced by summing the structure factor intensities $|F_\alpha|^2$, $|F_\beta|^2$ of α and β -phase models according to

$$|F|^2 = (1-x)|F_\alpha|^2 + x|F_\beta|^2 \quad (2.19)$$

where x is the fraction of β -phase. The formula implies phase separation, at least on the scale of the coherence length of the x-rays. A coverage calibration table can be derived from Eqn. 2.19 using the best-fit structural models for the α and β -phases (Table 2.3). With the aid of Table 2.3, it is possible to give an accurate estimate of the coverage by measuring only a few reflections carefully (typically (1/3,1/3) (2/3,2/3) and (4/3,1/3)). Agreement with photoemission coverage estimates is good (± 0.1 ML). Near completion of the β -phase, the ratio

$$|F(1/3, 1/3)|^2 / |F(2/3, 2/3)|^2 \quad (2.20)$$

is a particularly sensitive gauge of the coverage. There is an easily measurable 10-fold increase in this ratio between 1.33ML and 1.25 ML. The change has been found to correlate with a drop in the $\sqrt{3} \rightarrow 1 \times 1$ transition temperature, from about 300° C ($\theta > 1.33$ ML) to 175° C ($\theta < 1.3$ ML).

h	k	0.33	0.4	0.5	0.6	0.7	0.8	0.9	1.0	1.1	1.2	1.3	1.33
1/3	1/3	26.6	24.9	22.2	19.6	16.9	14.3	11.6	9.0	6.3	3.7	1.0	0.1
2/3	2/3	14.5	28.6	49.7	70.9	92.0	113.2	134.3	155.4	176.6	197.7	218.8	225.9
4/3	1/3	14.0	14.3	14.7	15.2	15.6	16.1	16.5	17.0	17.4	17.9	18.3	18.5
4/3	4/3	12.3	13.8	16.0	18.2	20.4	22.7	24.9	27.1	29.3	31.5	33.8	34.5
5/3	2/3	12.3	13.9	16.3	18.7	21.1	23.5	25.8	28.2	30.6	33.0	35.4	36.2
5/3	5/3	2.6	3.5	4.7	6.0	7.2	8.5	9.7	11.0	12.2	13.5	14.7	15.2
7/3	1/3	5.2	5.6	6.2	6.8	7.3	7.9	8.5	9.1	9.6	10.2	10.8	11.0
7/3	4/3	4.7	4.8	5.1	5.4	5.6	5.9	6.2	6.5	6.7	7.0	7.3	7.4
7/3	7/3	3.7	3.7	3.7	3.7	3.7	3.8	3.8	3.8	3.8	3.8	3.9	3.9
8/3	2/3	5.4	5.6	5.9	6.2	6.5	6.8	7.1	7.5	7.8	8.1	8.4	8.5
8/3	5/3	3.1	3.0	2.7	2.5	2.3	2.1	1.8	1.6	1.4	1.1	0.9	0.8
8/3	8/3	0.4	0.4	0.4	0.4	0.4	0.4	0.4	0.3	0.3	0.3	0.3	0.3
10/3	1/3	4.9	4.7	4.4	4.1	3.8	3.5	3.2	2.9	2.6	2.3	2.0	1.9
10/3	4/3	2.3	2.2	2.1	1.9	1.7	1.5	1.4	1.2	1.0	0.9	0.7	0.6
11/3	2/3	1.2	1.3	1.6	1.8	2.0	2.2	2.5	2.7	2.9	3.2	3.4	3.5
13/3	1/3	2.6	2.5	2.4	2.3	2.2	2.0	1.9	1.8	1.7	1.6	1.5	1.4

Table 2.3: Calculated structure factor intensities $|F_{calc}|^2$ as a function of coverage [ML]. Pure α and β phase models are based on the best-fit model to experimental data at 0.33 ML and 1.3 ML data (Table 2.1). Intermediate coverages are calculated using Eqn. 2.19. Intensities are normalized to units of electron scattering and divided by 250.

The Debye-Waller B-factors derived from the fits are not expected to be accurate due to the uncertainty in the polarization factor. However, we note that the β -phase B-factor is consistently larger than that of the α -phase. This may reflect the weaker binding of the β -phase structure to the substrate, since 3/4 of the atoms are not on high-symmetry sites.

As discussed in section 2.1, the integer-order reflections can be analysed by combining the surface and substrate structure factors coherently for different registries of the surface structure. For Ge(111), it is straightforward to show that the in-plane structure factor of a bulk termination rod per 1x1 unit cell is (for an ideally flat surface):

$$F_{\text{bulk}} = -if_{\text{Ge}} e^{-M_{\text{Ge}} \cot\left(\frac{\pi}{3}(2h+k)\right)} \quad (2.21)$$

Since the scale factor and the structural parameters of the superstructure have been derived from the analysis of the fractional order reflections, the registry is the only fit parameter required for the integer-order analysis. The best-fit results are shown in Table 2.4 for coverages of 0.33 and 1.3 ML. The α -phase has T_4 registry, the β -phase H_3 registry.

h	k	0.33 ML			1.3 ML			Pb β -phase		Ge substrate	
		$ F_{\text{exp}} ^2$	σ_{exp}	$ F_{\text{calc}} ^2$	$ F_{\text{exp}} ^2$	σ_{exp}	$ F_{\text{calc}} ^2$	$ F_{\text{calc}} _{\text{Pb}}$	$\Phi_{\text{Pb}}/2\pi$	$ F_{\text{calc}} _{\text{Ge}}$	$\Phi_{\text{Pb}}/2\pi$
1	0	53.2	12.0	51.8	31.3	6.8	22.9	5.3	-0.26	3.0	0.42
2	0	41.1	9.0	28.4	29.5	5.9	38.9	8.2	0.01	2.4	0.58
2	1	22.0	2.5	18.6	9.5	2.2	19.3	3.3	0.22	2.0	0.42
3	1	9.8	1.1	8.4	0.2	0.2	1.6	2.5	0.03	1.5	0.58
4	0	7.4	1.8	7.1	3.0	0.6	3.3	1.2	0.17	1.3	0.42
3	2	5.7	1.6	5.1							
			$\chi^2=1.0$	(T_4)		$\chi^2=7.5$	(H_3)				

Table 2.4: Integer order reflections for two of the experimental data sets. For the α -phase, T_4 registry is favored (other registries have $\chi^2 > 20$). For the β -phase, the corner atoms of the unit cell sit on H_3 sites (other registries, $\chi^2 > 50$). Also tabulated are structure factor amplitudes and phases for the β -phase Pb atoms and for the Ge substrate. Note that for (20) and (31) reflections, the scattering is nearly in antiphase. Data is normalized as in Tables 1 and 2.

2.6 References

1. B. E. Warren, in "X-ray Diffraction", Addison-Wesley (1969). For recent reviews of the surface diffraction technique see: R. Feidenhans'l, Risø Report M-2569, Risø National Laboratory (1986); J. Als-Nielsen, in "Structure and Dynamics of Surfaces", Vol. 2 Eds. W Schommers and P. van Blanckenhagen, Springer Verlag, (1987); I. Robinson in "Handbook of Synchrotron Radiation", Eds. D. E. Moncton, G. Brown, North Holland (1987); P. A. Fuoss, K. S. Liang and P. Eisenberger in "Synchrotron Radiation Research", Ed. R. Z. Bachrach, Plenum (1987).
2. G. H. Vineyard, Phys. Rev. B26, p.4146-4159, (1982).
3. S. M. Goldberg, C. S. Fadley, S. Kono, Jour. of Electron Spectr. and Related Phenomena 21, p.285-363 (1981).
4. R. D. Bringans, R. I. G. Uhrberg, R. Z. Bachrach, Phys. Rev. B34, p. 2373-2380 (1986).
5. T. Kinoshita, S. Kono, T. Sagawa, Phys. Rev. B34, p.3011-3014 (1986).
6. J. M. Nicholls, B. Reihl, J. E. Northrup, Phys. Rev. B35, p. 4137-4140 (1987).
7. R Feidenhans'l, op. cit. (ref. 1) .
8. G. Materlik, P. Suortti, DESY Report SR 83-13 (1983).
9. J. S. Pedersen, R. Feidenhans'l, M. Nielsen, F. Grey, R. L. Johnson, Surf. Sci. 189/190, p1047-1054 (1987).
10. R. Feidenhans'l, J. S. Pedersen, M. Nielsen, F. Grey, R. L. Johnson, Surf. Sci. 178 p.927-933 (1986).
11. E. J. Lisher, Acta Crysta A32, p.506-509 (1976).
12. B. W. Batterman, D. R. Chipman, Phys. Rev. 127, p.690-693 (1962).

3. OBSERVATION OF LIQUID SCATTERING FROM A 2d LAYER OF Pb

Abstract: On the basis of RHEED measurements, it has been proposed (ref. 1) that in the 1×1 phase of Pb/Ge(111), Pb is a two-dimensional (2d) liquid. Surface X-ray diffraction measurements of an isotropic halo of scattering about the origin in reciprocal space provide confirming evidence for this statement.

3.1 Introduction

The $\sqrt{3} \times \sqrt{3} R30^\circ$ β -phase of Pb/Ge(111) has a transition to a 1×1 phase at a temperature of approximately 330° C (ref. 2). It has been suggested that the transition is to an ordered structure with the 1×1 symmetry of the substrate (ref. 3, 4). However, Ichikawa has studied the 1×1 phase with Reflection High Energy Electron Diffraction (RHEED), and observed diffuse halos of scattering about the origin in reciprocal space, which he interprets as being due to a 2d liquid layer of Pb (ref. 1). On the basis of the isotropy of the observed halos, Ichikawa proposes that the liquid layer is unperturbed by the substrate.

In this chapter we present surface X-ray diffraction measurements of the strongest liquid-like halo observed by Ichikawa. We find that the halo coexists with the $\sqrt{3}$ structure below the transition, implying a first order 2d melting transition.

3.2 Theory

In this section we derive the basic results of liquid scattering theory, and investigate the dependence of liquid scattering on the dimension d of the liquid. Consider a pure liquid with N atoms, the instantaneous electron density of which can be written

$$\rho(\mathbf{r}) = \rho_A(\mathbf{r}) \otimes \sum_{n=1}^N \delta(\mathbf{r} - \mathbf{r}_n) \quad (3.1)$$

where the notation of Chapter 2 is adopted, and the \mathbf{r}_n are the atom centers. The scattered amplitude is then

$$\Lambda(\mathbf{q}) = f_A(\mathbf{q}) \sum_{n=1}^N e^{i\mathbf{q} \cdot \mathbf{r}_n} \quad (3.2)$$

For an ideal gas of particles with no interactions the r_n are completely random, and on average the phase factors will cancel except for $q \rightarrow 0$. At $q=0$, the scattered amplitude is

$$A(q=0) = Nf_A(0) \quad (3.3)$$

Nevertheless, there is scattered *intensity* at non-zero q . The problem can be mapped onto a random walk in the complex plane. The step length is

$$x_n = f_A(q) e^{iq \cdot r_n} \quad (3.4)$$

the average total distance travelled is

$$\langle A(q) \rangle = Nf_A(q) \langle e^{iq \cdot r_n} \rangle = 0 \quad (3.5)$$

where the brackets indicate averaging over all n . The variance is

$$\langle A(q) A^*(q) \rangle = Nf_A^2(q) \left(\langle e^{iq \cdot r_n} e^{-iq \cdot r_n} \rangle - \langle e^{-iq \cdot r_n} \rangle^2 \right) = Nf_A^2(q) \quad (3.6)$$

Thus at finite q , the intensity is simply that due to N atoms scattering incoherently, as might intuitively be expected for a completely random distribution of atoms. In real liquids, however, the positions are correlated. Central to liquid scattering theory is the Pair Distribution Function (PDF) $g(r)$ defined such that $g(r)4\pi r^2 dr$ is the time-averaged probability of finding an atom in a shell between r and $r+dr$, given that there is an atom at the origin. Due to hard-core repulsion

$$g(r) \rightarrow 0 \quad (r \rightarrow 0) \quad (3.7)$$

Attraction will produce oscillations in $g(r)$ due to higher than average density for shells of nearest neighbours, next-nearest neighbours, and so on. For a liquid the oscillations die out rapidly and

$$Ng(r) \rightarrow \rho_0 \quad (r \rightarrow \infty) \quad (3.8)$$

where ρ_0 is the average atom density of the liquid. Calculating $g(r)$ from first principles is one of the central problems in liquid state theory. Here we assume only that the function is isotropic. Returning to the phase factor sum of Eqn. 3.2, and following Warren (ref. 5)

$$\begin{aligned}
 I &= f_A^2(q) \sum_m e^{iq \cdot r_m} \sum_n e^{-iq \cdot r_n} \\
 &= N f_A^2(q) + \sum_m f_A^2 \sum_{n \neq m} e^{iq \cdot r_{mn}}
 \end{aligned}
 \tag{3.9}$$

r_{mn} : atom position relative to origin atom = $r_m - r_n$

The first term is identical to that obtained for the ideal gas: by collecting phase-factor products with $n = m$ we have extracted the self-correlation term. Averaging over configurations about each atom, and letting r_{mn} become a continuous variable, the second term is

$$N f_A^2(q) \rho_0 \int_V g(r) e^{iq \cdot r} dr
 \tag{3.10}$$

where the condition $n \neq m$ is incorporated in the definition of $g(r)$ and integration is over the sample volume V . The result is then split into

$$N f_A^2(q) \rho_0 \left\{ \int_V [g(r) - 1] e^{iq \cdot r} dr + \int_V e^{iq \cdot r} dr \right\}
 \tag{3.11}$$

The first term in braces is due to short range order and is 0 for the ideal gas. The second term is simply the Fourier transform of the shape function of the liquid. The PDF and scattered intensity for ideal gas and realistic liquid are sketched in Fig. 3.1.

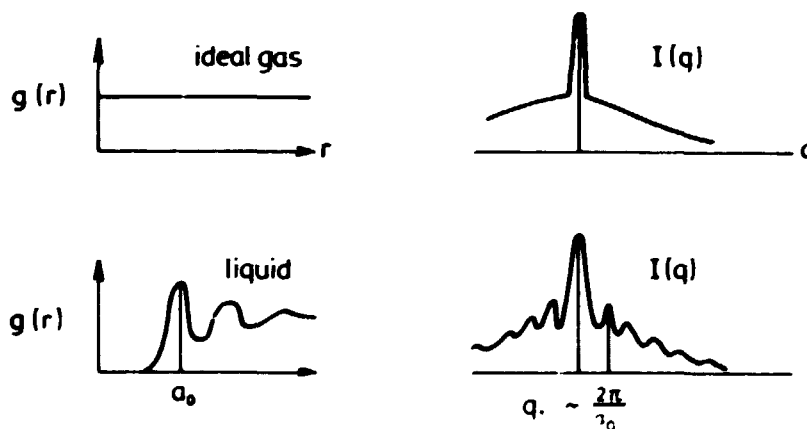


Fig. 3.1: Sketch of the pair distribution function $g(r)$ and corresponding scattered intensity for an ideal gas with no interactions and for a realistic model of a liquid. The position q_1 of the first ring of intensity is determined by the position a_0 of the nearest neighbour shell in the liquid.

Experimentally, the quantity of interest is the liquid static structure factor

$$S(q) = 1 + \rho_0 \int [g(r)-1] e^{iq \cdot r} dr \quad (3.12)$$

$S(q)$ for a monatomic liquid is obtained from the measured isotropic intensity after correction for Compton scattering, and division by the squared atomic form-factor of the liquid atom (ref. 5).

For a given $g(r)$, the scattered intensity from a d -dimensional liquid will depend on d through the form of the integration element in Eqn. 3.11. The results for $d=1,2,3$ are summarized in Table 3.1. For simplicity, a delta function at $r=a_0$ is considered. Although this PDF is adequate for the purpose of demonstration, this is not a liquid PDF but that of a gas formed of diatomic molecules, and is known as the Ehrenfest model. The main effect of the dimension is that the first peak in the diffracted intensity shifts to larger q as the dimension of the liquid increases.

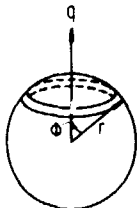
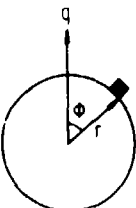
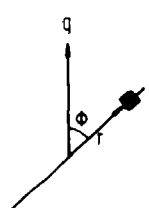
Dimension	3	2	1
Volume elements	 $2\pi r^2 \sin\phi dr d\phi$	 $r dr d\phi$	 dr
Transform $i(q) = (S(q)-1)/\rho_0$	Fourier-Sine $K(r) \sin qr dr$	Fourier-Bessel $K(r) J_0(qr) dr$	Fourier $K(r) e^{iqr \cos\phi} dr$
Kernel $K(r)$	$\frac{4\pi r}{q} [g(r)-1]$	$2\pi r [g(r)-1]$	$[g(r)-1]$
$i(q)$ for $g(r)-1 = \delta(r-a_0)$	$4\pi a_0^2 \text{sinc}(qa_0)$	$2\pi a_0 J_0(qa_0)$	$2\cos(q a_0 \cos\phi)$
First maximum	$\frac{2\pi}{a_0} \cdot 1.2295$	$\frac{2\pi}{a_0} \cdot 1.1166$	$\frac{2\pi}{a_0} \quad (\phi = 0)$

Table 3.1: Dimensional dependence of liquid scattering. A simple example, which is equivalent to the Ehrenfest model for a diatomic molecule, illustrates the shift of the first peak in $S(q)$ to higher q as a function of dimension, for a fixed nearest-neighbour distance a_0 .

The form of $S(q)$ for a fluid depends on the density of the fluid. For a dilute gas, $S(q)$ reflects the hard-core radius of the atom. For a dense liquid, shells or rings (in 2d) of nearest neighbours result in a more strongly modulated $S(q)$. Atoms in an elemental liquid have a local close-packed geometry, so $S(q)$ is very similar when scaled to $2\pi/a_0$ (ref. 6).

3.3 Experimental Method

The measurements were made at the wiggler line W1 in HASYLAB. Sample preparation, alignment and coverage calibration are detailed in Chapter 3. The wavelength was 1.370 Å and the angle of incidence was set to $\alpha_i = 0.9^\circ$. From measurements of several fractional order reflections of the Pb $\sqrt{3}$ structure at room temperature, the coverage was estimated to be 1.33 ± 0.05 ML. The estimated coverage corresponds to a complete β -phase within the errors.

The measurements were made with a "baby" transfer chamber, without thermocouple. The temperature was calibrated using the current-voltage characteristics of the Ge sample. The transition temperature, at which the intensity at the position of the (2/3,2/3) surface reflection falls to background level, was $300^\circ \pm 50^\circ$ C. According to the phase diagram of Pb/Ge proposed by Ichikawa (ref. 2), this transition temperature corresponds to a pure β -phase (4/3 ML).

Above the transition, ω -scans 5° either side of the nominal position of the (2/3,2/3) reflection were featureless, but radial scans showed a broad, weak peak centered at a slightly smaller q than that of the (2/3,2/3) reflection. Fig. 3.2 illustrates a scan through the liquid peak along the (1,1) direction, at a temperature of $320^\circ \pm 5^\circ$ C where the error is relative to the nominal transition temperature, 300° C. The solid curve is a fitted Gaussian. The sloping background is due to streaks of thermal diffuse scattering (TDS) extending from the bulk in-plane (1,1) reflection. Radial scans were made at the same temperature 10° and 15° to either side of the (1,1) direction, as shown in Fig. 3.3. The halo is isotropic within this range, as determined by Gaussian fits to the lineshape (Table 3.2). The width of the peak is mainly intrinsic; the experimental resolution for radial scans is 0.045 \AA^{-1} . We were not able to observe further rings of intensity, because of relatively intense ridges of bulk TDS along the high-symmetry directions through the in-plane bulk Ge reflections (1,1), (3,0).

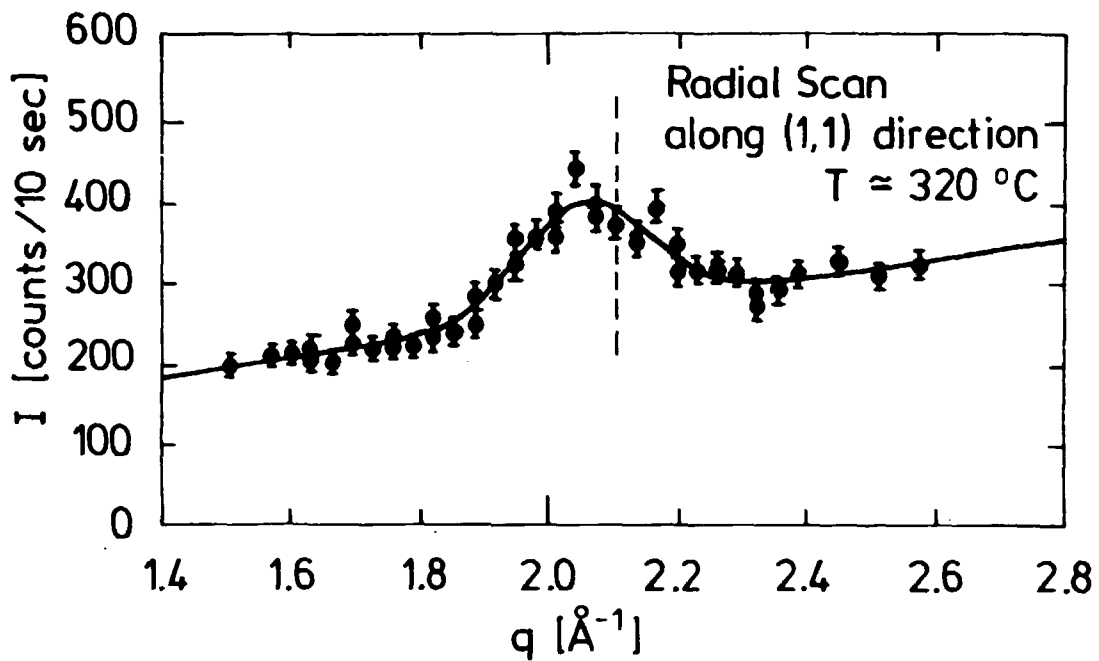


Fig. 3.2: Radial scan through the diffuse halo in the 1×1 phase, along the $(1, 1)$ direction. The position of the $(\frac{2}{3}, \frac{2}{3})$ surface reflection in the β -phase is indicated by a dashed line.

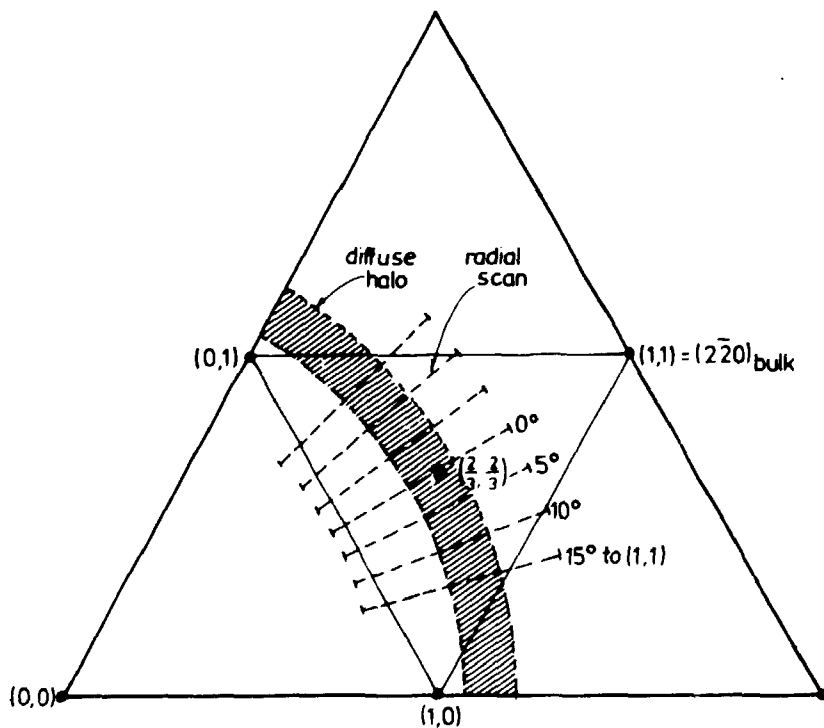


Fig. 3.3: Reciprocal space illustration of position and FWHM of the diffuse halo seen in the 1×1 phase.

$\omega(1,1)$	Amplitude (counts/10s)	Midpoint (\AA^{-1})	FWHM (\AA^{-1})
0°	135 ± 20	2.055 ± 0.01	0.245 ± 0.01
$10^\circ +$	110 ± 25	2.052 ± 0.01	0.225 ± 0.01
$10^\circ -$	80 ± 25	2.048 ± 0.01	0.225 ± 0.01
$15^\circ +$	100 ± 20	2.065 ± 0.01	0.230 ± 0.01
$15^\circ -$	150 ± 20	2.065 ± 0.01	0.230 ± 0.01
(2/3, 2/3)	2×10^5	2.095 ± 0.005	0.0350 ± 0.002

Table 3.2: Parameters of Gaussian fits to the radial scans through the liquid halo in the 1×1 phase. $\omega(1,1)$ is the direction of the radial scan relative to the $(1,1)$ direction (see Fig. 3.3). To within the precision of the measurement, the halo is isotropic. For comparison, the parameters for the $(2/3, 2/3)$ peak of the β -phase at room temperature are given (no correction for instrumental resolution).

The halo intensity persists into the $\sqrt{3}$ phase. Fig 3.4 illustrates radial scans 10° off the $(1,1)$ axis. For each scan, the estimated temperature is given, as well as the ratio of the integrated intensity, I , in an ω scan of the $(2/3, 2/3)$ reflection at that temperature, to the integrated intensity at room temperature, I_0 .

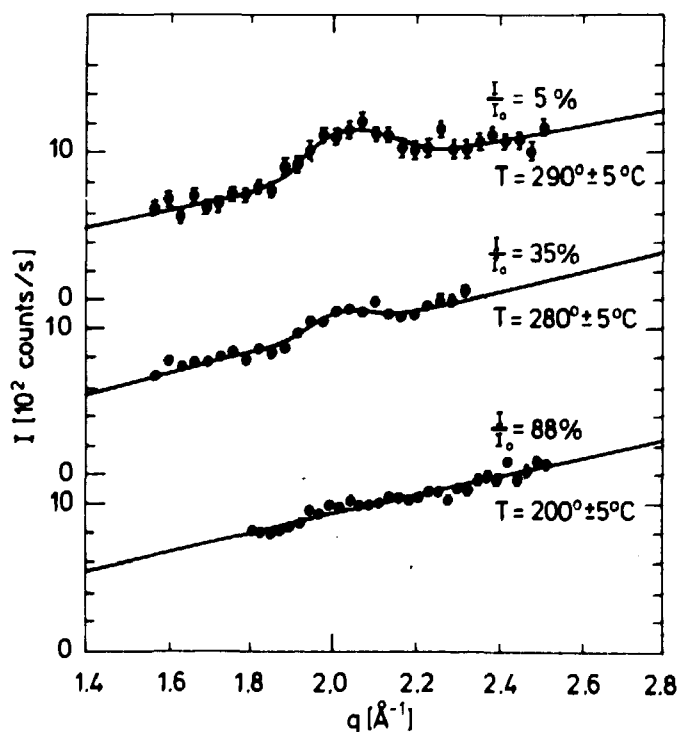


Fig. 3.4: Radial scans 10° to the $(1,1)$ direction, below the $1 \times 1 \rightarrow \sqrt{3}$ transition temperature ($\sim 300^\circ\text{C}$). The liquid halo is still detected $\sim 20^\circ$ below the transition, implying a two-phase region.

3.4 Discussion

The position of the isotropic peak in the 1×1 phase ($2.05 \pm 0.01 \text{ \AA}^{-1}$) is very close to the position determined by Ichikawa of 2.01 \AA^{-1} . We note that in his study, Ichikawa quotes a coverage of 1.3ML, for which the transition temperature is 192° C ; Ichikawa's measurements were made at 258° C . The position of the first ring of scattering of 3d liquid Pb at 239° C is 2.19 \AA^{-1} (ref. 7). The shift of the halo to larger q in 3d is expected from the discussion in section 3.2. From the simple model considered in Table 3.1, a 10% shift is expected on going from a 2d liquid to a 3d liquid of the same areal density. The experimental shift is 7%. The discrepancy is probably mainly due to the limitations of the Ehrenfest model for the description of a liquid static structure factor.

To the best of the author's knowledge, this measurement represents the first X-ray observation of the isotropic scattering from a liquid monolayer. Even with the intensity from a wiggler, the 2d liquid scattering is so weak that it is not possible to measure $S(q)$ in detail. This problem could in future be remedied to some extent by measuring with the incidence and exit angles below the critical angle, in order to maximize signal-to-noise.

It is instructive to compare the results of Ichikawa for the positions of maxima and minima of $S(q)$ (the amplitudes cannot be deduced from the published RHEED data) with those of the intercalation compounds C_{24}Rb (ref. 8) and C_{24}Cs (ref. 9), in the room-temperature 2d liquid phase of the intercalate. This is done in Table 3.3; the similarity is clear when the peaks are scaled to q_1 , the position of the first halo. Also included for comparison is the scattering vector corresponding to the nearest neighbour distance in the solid phase. The similarity of the liquid scattering due to Pb and that due to the intercalates suggests that the 1×1 phase, like the liquid phase of the intercalates, is best described as a random 2d liquid. The scattering from a disordered lattice gas, for example, would have a quite different $S(q)$ (ref. 10).

		$C_{24}Cs$			$C_{24}Rb$			$Pb/Ge(111)$	
max	min	$q[\text{\AA}^{-1}]$	q/q_1	$S(q)$	$q[\text{\AA}^{-1}]$	q/q_1	$S(q)$	$q[\text{\AA}^{-1}]$	q/q_1
1		1.17	1	3.1	1.22	1	2.9	2.01	1
	1	1.65	1.41	0.8	1.75	1.43	0.7	3.10	1.54
2		2.28	1.95	1.4	2.44	2.00	1.2	4.0	2.0
	2	2.9	2.6	0.9	3.0	2.5	0.8	4.8	2.4
3		4.7	3.6	1.1	3.9	3.2	1.1	5.7	2.9
	3				4.5	3.7	0.9	6.9	3.4
	$2\pi/a_{nn}$	1.04	0.89		1.04	0.85		1.81	0.90

Table 3.3: Comparison of positions of maxima and minima for $S(q)$ of two intercalates and $Pb/Ge(111)$. q_1 is the position of the first maximum in $S(q)$. All values estimated by the author on the basis of published data (ref. 8, 9, 1). For comparison, the spatial frequency corresponding to the nearest neighbour distance a_{nn} in the solid phase is shown. The amplitude of $S(q)$ cannot be estimated from the RHEED data for $Pb/Ge(111)$.

The coexistence of liquid scattering and surface Bragg reflections implies that the melting of the β -phase of $Pb/Ge(111)$ is first-order, and that the phase diagram includes a mixed-phase ($\beta + 1 \times 1$) region. In the analysis, we have not considered the possibility of a substantial change in density in the $\beta \rightarrow 1 \times 1$ transition, which could affect $S(q)$. We find no evidence for loss of Pb after several cycles through the transition. The liquid phase may thus involve local density fluctuations perpendicular to the surface (partial population of a second layer), and would not be a 2d liquid in the strictest sense.

3.5 Conclusion

We have measured an isotropic halo of scattering in the 1×1 phase of $Pb/Ge(111)$ at a coverage of $1.33 \pm .05ML$. This observation agrees with previous RHEED measurements, and supports the view that the $\beta \rightarrow 1 \times 1$ transition is a 2d melting transition, and that the Pb in the 1×1 phase is a 2d liquid. The coexistence of the isotropic scattering with fractional-order Bragg reflections from the β -phase indicates that the transition is first order.

3.6 References

1. T. Ichikawa, Solid State. Comm. 49, p. 59-64 (1984).
2. T. Ichikawa, Solid State Comm. 46, p. 827-831 (1983).
3. J. J. M. tois, G. Le Lay, Surf. Sci. 133, p. 422-442 (1983).
4. B.P. Tonner, H. Li, M. J. Robrecht, M. Onellion, J. L. Erskine, Phys. Rev. B36, p. 989-997 (1987).
5. B. E. Warren, "X-ray Diffraction", Addison Wesley (1969), Chap. 10.
6. L. E. Reichl, "A Modern Course in Statistical Physics", University of Texas Press (1984)., Chap 11 and references therein.
7. R. Kaplow, S. L. Strong, B. L. Averbach, Phys. Rev. 145, p. 1336-1345 (1965).
8. S. C. Moss, G. Reiter, J. L. Robertson, C. Thompson, J. D. Fan, Phys. Rev. Lett. 57, p. 3191-3194 (1986).
9. R. Clarke, N. Caswell, S. A. Solin., p. M. Horn, Phys. Rev. Lett. 43, p. 2018-2021 (1979).
10. M. J. Winokur, J. H. Rose, R. Clarke, Phys. Rev. B25, p. 3703-3713 (1982).

4. NATURE OF THE HIGH-TEMPERATURE 1×1 PHASE OF Pb/Ge(111)

Abstract: We have used surface X-ray diffraction to monitor several in-plane integer-order reflections of Pb/Ge(111) through the $\sqrt{3} \times \sqrt{3} R30^\circ (\beta) \rightarrow 1 \times 1$ transition at 175°C and a coverage of $1.25 \pm .05 \text{ ML}$. The results are compared with several models of the 1×1 phase, and favour a 2d liquid model, where the liquid is modulated by the periodic potential of the host substrate. Values for Fourier components of the adsorbate-substrate interaction potential are derived.

4.1 Introduction

A very common type of surface phase transition is that between an ordered phase with a superstructure and a high-temperature phase with the 1×1 diffraction pattern of the substrate. Examples include Si(111) $7 \times 7 \rightarrow 1 \times 1$ at $T = 1100 \text{ K}$ (ref. 1) and Au (110) $2 \times 1 \rightarrow 1 \times 1$ at $T = 570 \text{ K}$ (ref. 2), as well as Pb/Ge(111) $\sqrt{3} \rightarrow 1 \times 1$ at $T = 175^\circ \text{C}$ (448 K) which is discussed here. Such transitions are possible candidates for order-disorder transitions, which have attracted considerable theoretical interest (ref. 3). But although the experimentalist may suspect a disordered phase, an ordered overlayer structure with the 1×1 periodicity of the ideal surface cannot be ruled out - at least not on the basis of the symmetry of the reciprocal lattice alone. Further, there are distinctions in the theoretical literature between different types of disorder. Two examples are a disordered lattice gas, where adsorbate atoms populate a random subset of specific lattice sites, and a two-dimensional liquid, where the overlayer atoms are essentially unperturbed by the periodic potential of the substrate. Reality may lie somewhere between the two extremes. The experimental task is to decide between these various possibilities.

In this chapter we present surface X-ray diffraction measurements of the intensity of the integer-order surface reflections (those reflections belonging to the reciprocal lattice of the ideal, unreconstructed surface of the substrate) as a function of temperature through the $\sqrt{3} \rightarrow 1 \times 1$ transition of Pb/Ge(111). We are able to determine the nature of the 1×1 phase by comparing the experimental results with several models: a 1×1 ordered structure, a purely lattice gas type of disorder, and the sort of disorder associated with a random dense liquid. We find that for Pb/Ge(111), the 1×1 phase is best described by a 2d dense liquid, perturbed by the periodic potential of the host surface.

Reiter and Moss (ref. 4) have recently developed a theoretical expression for the structure factors of the integer order reflections, in the case where the interaction potential between the liquid overlayer and the substrate is small but not negligible. We are able to apply this theory, albeit with some rather crude approximations, to derive values for several Fourier components of the adsorbate-substrate interaction potential in the 1×1 phase of Pb/Ge(111).

4.2 Theory

If an external potential $V(r)$ imposes a periodic modulation on the density of a liquid, there will result Bragg diffraction. The phenomenon has a well-known example in optics: the Debye-Sears effect (ref. 5). In that case, light is diffracted by the density modulation in a liquid due to an ultrasonic source. The case considered here is a 2d liquid modulated by a periodic host substrate. In the general form considered by Reiter and Moss, the problem is quite complex. However if the modulation potential is small, it is possible to derive a simple result by a straightforward linear response calculation. First we consider the even simpler case of an ideal 2d (classical) gas, for which the Boltzmann distribution determines the density:

$$\rho(r) = \rho_0 e^{-V(r)/k_B T} \quad (4.1)$$

k_B : Boltzmann constant

T : absolute temperature

For simplicity only one Fourier component will be considered:

$$V(r) = V_1 \cos(q_1 x) \quad (4.2)$$

For the case where $V_1 \ll k_B T$, the exponential in Eqn. 4.1 can be expanded, yielding

$$\rho(r) = \rho_0 \left(1 - \frac{V_1}{k_B T} \cos(q_1 x) \right) \quad (4.3)$$

The Fourier transform contains two Bragg reflections (delta functions) at $\pm q_1$ of amplitude $(-\rho_0 V_1/2k_B T)$. In the case of a real liquid, the Boltzmann distribution is not applicable. The result for small $V(r)$ is, however, very similar (ref. 4). The response (deviation from thermodynamic mean value) of the Fourier component $\rho_{hk} e^{i q_{hk} x}$ of the density to a weak external potential $V(r)$, can be written in terms of the generalized susceptibility, $\chi(q, \omega)$, as

$$\delta \langle \rho(q, \omega) \rangle = -\chi(q, \omega) V(q, \omega) \quad (4.4)$$

where the brackets indicate a thermal average. Since we are dealing with a static field, we need only consider the static susceptibility, defined as (ref. 6):

$$\chi(q) = \frac{1}{k_B T} \int [g(r)-1] e^{iq \cdot r} dr \quad (4.5)$$

where $g(r)$ is the pair distribution function, and the integral in Eqn. 4.5 is the liquid static structure factor $S(q)$ (see Chapter 3). For the potential

$$V(r) = \sum_{h,k} V_{hk} e^{iq_{hk} \cdot r} \quad (4.6)$$

the response is, to first order in $V_{hk}/k_B T$ (ref. 6):

$$\delta \langle \rho(q) \rangle = - \frac{S(q) V_{hk}}{k_B T} \delta(q, q_{hk}) \quad (4.7)$$

For large q , $S(q) \rightarrow 1$, and the ideal gas result is retrieved. Eqn. 4.7 is for point atoms. For X-ray scattering we are interested in the electronic density. Multiplying Eqn. 4.7 by the atomic form factor gives the scattering amplitude per liquid atom. The result should be multiplied by the number of liquid scatterers per surface unit cell, to obtain the structure factor of the modulated liquid at the integer-order positions.

4.3 Experimental Method

The surface X-ray diffraction measurements were made at the wiggler line W1 in HASYLAB. The sample preparation technique, alignment and coverage determination are detailed in Chapter 2. For this measurement, the X-ray wavelength was 1.30 Å, the grazing angle of incidence was set to 1°.

By measuring several fractional order reflections due to the $\sqrt{3}$ structure at room-temperature, it is possible to determine the coverage accurately (Chapter 2). For this sample, the coverage was estimated to be 1.25 ± 0.05 ML. The estimated coverage corresponds to 6% less than a complete β -phase. There was no measurable change of coverage after several cycles through the transition to the 1×1 phase. Temperature was measured by a thermocouple making contact to the back of the sample. The transition occurred at approximately 175°C, at which temperature the intensity at

the position of the peak of the (2/3, 2/3) surface reflection had fallen to background level. The transition temperature is in reasonable agreement with the results of a Reflection High Energy Electron Diffraction (RHEED) study of the phase diagram by Ichikawa (ref. 7), which indicates that at slightly less than a complete β -phase (4/3ML), there is a transition to a 1×1 phase at 192°C .

Sample rotation (ω) scans were made of several integer-order reflections as a function of temperature through the transition. The structure factor intensities of the reflections are plotted in Fig. 4.1a-d. Because the room temperature structure has been determined by surface X-ray diffraction (ref. 8, 9), the structure factor intensities can be expressed in absolute units.

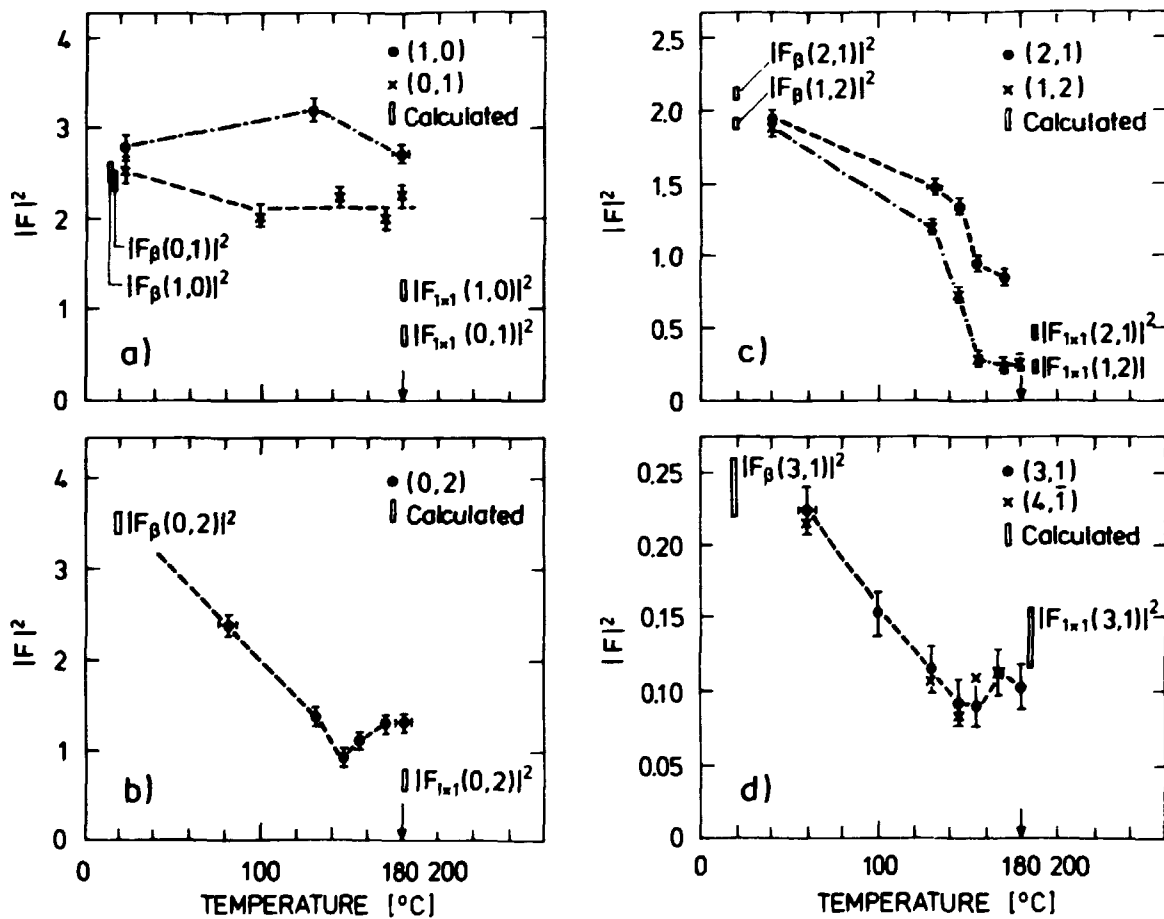


Fig. 4.1a-d: Measured integer-order structure factor intensities as a function of temperature, through the $\sqrt{3} \rightarrow 1 \times 1$ transition at 175°C . The open bars are calculated intensities with $q_z = 0.09 \text{ \AA}^{-1}$. Structure factor intensities are per 1×1 unit cell, in units of electron scattering divided by 250.

For comparison, theoretical values of the structure factor intensities are also plotted. At room temperature, these intensities are calculated from the known structure of the β -phase ($|F_{\beta}(h, k)|^2$ in Figs. 4.1a-d). A minor correction is also made for the small amount of α -phase present, based on the estimated coverage. At 180° C, we have plotted the structure factor intensities expected for an ideal 1×1 Ge(111) surface ($|F_{1 \times 1}(h, k)|^2$ in the Figs. 4.1 a-d), using the Debye Waller B-factor $B=0.85$ (ref. 10). The integer-order reflections vary rapidly as a function of perpendicular momentum transfer (q_z), even for the small range of q_z probed by the detector (0.18 \AA^{-1}). The plotted theoretical values are for the average q_z , 0.09 \AA^{-1} .

4.4 Analysis

The measured structure factor intensities in the 1×1 phase are corrected for the measured intensity variation along the direction normal to the surface, to obtain a set of in-plane structure factor intensities $|F_{\text{exp}}(hk)|^2$ and experimental errors σ_{exp} , given in Table 4.1. The values in Table 4.1 include (hk) and (kh) reflections, when both have been measured.

h	k	(a) $ F_{\text{exp}}(h, k) ^2$	(b) $ F_{1 \times 1}(h, k) ^2$	(c) $S(q_{hk})$	(d) $V_{hk}/k_B T$ Pb/Ge(111) 1×1	(e) $\frac{V_{hk}}{k_B T}$	(f) $\frac{V_{hk}}{k_B T}$
1	0	2.4 \pm 0.1	1.0 \pm 0.1	1.1 \pm 0.4	0.21 \pm 0.06	0.48	0.45
0	1	2.8 \pm 0.1	1.0 \pm 0.1	"	0.25 \pm 0.06	"	"
0	2	1.1 \pm 0.6	0.56 \pm 0.06	1.2 \pm 0.2	0.15 \pm 0.05	0.14	0.01
2	1	0.72 \pm 0.06	0.44 \pm 0.06	1.0 \pm 0.2	0.15 \pm 0.05	0.04	0.03
1	2	0.39 \pm 0.06	0.44 \pm 0.06	"	0 \pm 0.05	"	"
3	1	0.15 \pm 0.03	0.20 \pm 0.03	0.9 \pm 0.1	0 \pm 0.03	-	-

Table 4.1: Column (a) is the experimental integer-order structure factor intensities in the 1×1 phase at $T=180^\circ \text{ C}$, in units of electron scattering divided by 250. Column (b) gives the theoretical values for a 1×1 unreconstructed Ge(111) surface (both (a) and (b) are per 1×1 unit cell); Column (c) is the ideal 2d liquid structure factor, estimated as described in the analysis. Using Eqn. 4.10, it is possible to extract approximate values for the amplitudes of the adsorbate-substrate interaction potential (d). These are compared with results for the intercalation compound C_{24}Rb ($T=300 \text{ K}$), both as obtained from an approximate expression analogous to Eqn. 4.10, and using an exact expression (e and f, respectively).

Three simple models for the transition are considered: order-order, order-disorder, and solid-liquid. A 1d sketch of the main features of each model is illustrated in Fig. 4.2. Structural models for the 1×1 phase were tested against the data in Table 4.1: a χ^2 residual was used to determine goodness of the model.

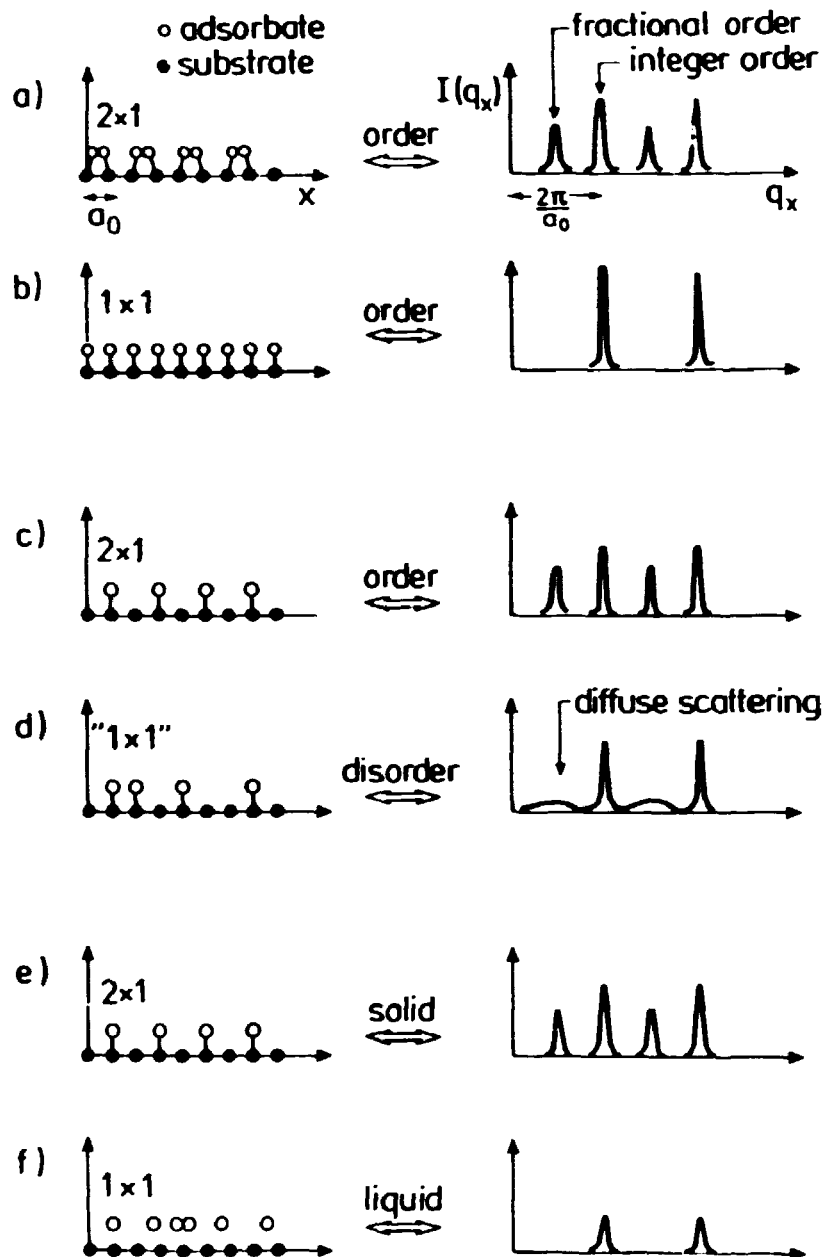


Fig. 4.2: 1d illustration of three types of transition to a 1×1 phase: order-order (a \rightarrow b), order-disorder (c \rightarrow d), and solid-liquid (e \rightarrow f). In general, order-order will involve an increase of intensity at the integer-order reflections and solid-liquid a decrease. For order-disorder, the integer-order reflections remain nominally the same.

Order-order: This model assumes that the high temperature phase is an ordered phase with the 1×1 periodicity of the substrate. The simplest structural model of a 1×1 phase is one Pb atom per surface unit cell of the unreconstructed Ge(111) surface (see Fig. 1.4c). Slight distortions of such a 1×1 structure can yield a $\sqrt{3}$ unit cell, and such a model has been proposed for the dense phase of Pb/Ge(111) (ref. 11, 12). For the closely analogous system Pb/Si(111), it has been suggested that the transition to 1×1 involves disappearance of these distortions (ref. 13). To test this model for the 1×1 phase, it is assumed that the Pb atoms preferentially occupy one of the three high symmetry sites T_1 , T_4 , H_3 on the surface (see Fig. 1.2). The only free parameter considered was the Pb Debye-Waller factor. For each of the three possible registries, and allowing the Pb Debye-Waller factor to vary freely, this model gave $\chi^2 > 100$.

Order-disorder: From surface diffraction studies, the corner atoms of the β -phase are known to be registered on the H_3 site. However, there are three equivalent H_3 sites per $\sqrt{3}$ unit cell, defining three subdomains (a, b, c in Fig. 1.2). For the fractional order reflections, scattering from these subdomains interferes destructively. If the domain size shrinks well below the X-ray coherence length, but individual unit cells remain well registered (a lattice-gas model) there will be only diffuse short-range order scattering at the fractional reflections. In the case of one atom per $\sqrt{3}$ unit cell (the α -phase), such an order-disorder transition has been shown to belong to the universality class of the three-state Potts model (ref. 14). The contribution of the scattering to the integer-order reflections should, however, remain unchanged, except for Debye-Waller factor corrections. By varying the Debye-Waller factor,

$$e^{-M} = e^{-B_{Pb} q^2 / (4\pi)^2} \quad (4.8)$$

of the β -phase only, no good agreement could be obtained for $B_{Pb} < 7$ ($\chi^2 > 100$). The best agreement was $\chi^2 = 15$ for $B_{Pb} = 10.2$. We note that such a large value of B_{Pb} would correspond to a root-mean-squared thermal displacement of Pb atoms of 0.36 Å or over 20% of the Pb-Pb interatomic distance in the β -phase.

Solid-liquid: This model assumes that the Pb layer becomes a free-floating 2d liquid. In Ichikawa's RHEED study of Pb/Ge (ref. 7), the diffuse cylinders of scattering about the $(0, 0)$ position were interpreted as the two-dimensional analogue of diffuse rings from a dense liquid. From the isotropy of the rings, Ichikawa concluded that the liquid layer was not under the influence of the substrate potential. Our measurement of the first liquid halo supports Ichikawa's

findings (Chapter 3). Weak isotropic liquid scattering should not affect the integrated intensities of the integer-order Bragg reflections. So in this model of the 1x1 phase, the ideal bulk-terminated Ge(111) surface should give an adequate description of the integer-order structure factors. We find, however, $\chi^2 = 80$ with $B_{Ge} = 0.85$. Varying B_{Ge} produces only marginal improvement.

It should be emphasized that the above analysis is strongly dependent on the previous structural studies (ref. 8, 9). It would not be possible to quote the integer-order intensities in absolute units otherwise. The uncertainties in the structural parameters of the α and β -phases, in the estimated coverage and in the correction for finite q_z increase the quoted experimental uncertainties, reducing χ^2 . Nevertheless, none of the models proposed above can be deemed to provide an adequate description of the measured integer order reflections in the 1x1 phase.

Concerning the isotropic liquid model, though, we note that the discrepancy between measured and calculated integer-order structure factors falls off rapidly as q_{hk} increases (see Figs. 4.1a-d). Such a behaviour was recently reported by Moss et al. for the graphite intercalate $C_{24}Rb$ (ref. 15), and explained by including the contribution of the modulated liquid to the Bragg scattering, discussed in section 4.2. If the Fourier components of the graphite-intercalate (or adsorbate-substrate) interaction potential are small compared with $k_B T$, ie

$$V_{hk} \leq 0.1 k_B T \quad (4.9)$$

where V_{hk} is the amplitude of the hk Fourier component of the potential, then result (4.7) can be used. It is straightforward to show, using eqn 2.21 that the total integer-order in-plane structure factor for the 1x1 Ge substrate plus modulated liquid is, per 1x1 unit cell:

$$F(hk) = -if_{Ge} e^{-M_{Ge} \cot\left(\frac{\pi}{3}(2h+k)\right)} - \frac{4}{3} X f_{Pb} \frac{V_{hk}}{k_B T} S(q_{hk}) \quad (4.10)$$

where f_{Ge} and f_{Pb} are the atomic form factors of Ge and Pb, $\exp(-M_{Ge})$ is the Debye Waller factor of Ge, X is the ratio of the of the Pb areal density in the liquid phase to that in the ideal β -phase, and $S(q_{hk})$ is the static structure factor of the unperturbed 2d Pb liquid. To apply Eqn. 4.10 it is necessary to determine: (i) the unperturbed liquid structure factor $S(q_{hk})$, (ii) the relative Pb concentration X .

- (i) For $C_{24}Rb$, Moss et al were able to measure $S(q)$ out to large q . Although the unperturbed $S(q)$ is not accessible to experiment, they showed that the azimuthally averaged experimental $S(q)$ is a reasonable approximation. Further, the first integer-order graphite reflections occur at large q where $S(q) \approx 1$ to a good approximation. For Pb/Ge , we have neither an experimental $S(q)$, nor can we apply the approximation $S(q) \approx 1$, since the first integer-order reflections occur at q values where $S(q)$ is still oscillating strongly. When scaled to the position of the first maximum in the liquid scattering, Ichikawa's measurements of liquid halos of $Pb/Ge(111)$ agree at the 10% level with the positions of maxima and minima in the $S(q)$ of intercalated Rb and Cs (see Chapter 3). Encouraged by this similarity, we use the reported $S(q)$ (ref. 15) in order to estimate $S(q_{hk})$ for the reflections measured, the estimates are given in Table 4.1 with conservative errors.
- (ii) From the estimated coverage at room temperature, $X = 0.94$. However, a solid liquid transition is expected to be accompanied by a change in density. According to computer simulations, that change can be up to 20%. However, in the present case X is not known, and to be able to pursue the analysis we choose $X = 0.8$.

Having thus made crude, but not unreasonable estimates for the unknowns in Eqn. 4.10, we derive a set of $(V_{hk}/k_B T)$, given in Table 4.1. For comparison, the initial estimates of $V_{hk}/k_B T$ from the work of Moss et al, based on an equation similar to Eqn 4.10, are also shown in Table 4.1.

The relative error made in applying Eqn. 4.10 is proportional to $(V_{hk}/k_B T)$. For Pb/Ge this implies relative errors of $\sim 20\%$. Such poor accuracy warrants abandoning Eqn. 4.10 for more unwieldy, but exact expressions, derived by Reiter and Moss (ref. 4). However, given the large source of inaccuracy in the estimates of $S(q_{hk})$ and X , and the sparsity of the data, more refined analysis is a questionable exercise which we will not pursue.

We note that there is a pronounced dip in the integer-order intensity at about $150^\circ C$ for the $(0, 2)$ reflection. In the β -phase, the $(0, 2)$ structure factors for the $Pb \sqrt{3}$ unit cell and the bulk-termination rod are almost in antiphase (see Table 2.4). Thus, as the β -phase melts, this integer order reflection is expected to go through a minimum, when the scattering amplitudes of surface and bulk rod are nearly equal.

4.5 Discussion

In the analysis, we have emphasized the similarity of measurements presented here to those made on the graphite intercalation compound $C_{24}Rb$ by Moss et al. It is appropriate here to note the differences. Moss et al. measured bulk Bragg reflections of graphite. We have measured bulk-termination rods, typically some 10^{-6} times weaker than the bulk reflections of Ge. Because we restricted ourselves to in-plane measurements, some low-index integer-order reflections could not be measured (for example, (1, 1) and (3, 0) are bulk Bragg reflections of Ge). Further, due to the form of equation Eqn 4.10, it is not possible to determine the sign of V_{hk} , only its magnitude. Both these limitations could be overcome in future by measuring along the bulk-termination rod, and thus varying the relative phase of bulk and liquid terms in Eqn 4.10.

Despite their limited accuracy, the values of $V_{hk}/k_B T$ derived from the analysis deserve some comment. We note that the values of V_{hk} for Pb/Ge are of similar magnitude to those for $C_{24}Rb$. This is at first sight surprising, since the two systems are chemically very different. But a discussion in terms of chemical binding may not be appropriate for a weakly modulated liquid: The dominant interaction in a dense liquid is due to the hard core repulsion, and this may apply to the interaction between the liquid and the substrate.

It is assumed in the derivation of Eqn. 4.10 that the expansion coefficients V_{hk} are real, which implies that the position of the Ge surface atoms is an extremum of the potential surface. It is straightforward to show that V_{hk} becomes complex if the Pb liquid interacts with the second Ge layer, and that this breaks the symmetry between $(hk0)$ and $(kh0)$ reflections. The existing data (Table 4.1) is unfortunately too limited to reliably confirm or deny this effect.

Another point worthy of further investigation is the effect of the substrate modulation on $S(q)$. In the expressions for the scattering from a modulated liquid developed by Reiter and Moss, the Bragg peak contribution is a first order effect. To second order in $V_{hk}/k_B T$, the liquid halos become anisotropic and secondary halos appear about the innermost substrate Bragg reflections. Neither effect was detected in our study of the isotropic liquid scattering (Chapter 3). However, we estimate that such features would have a signal-to-noise ratio of less than one. More detailed experiments may thus reveal these predicted effects.

Finally, a remark concerning the disordered lattice gas model of the 1×1 phase. As B_{Pb} is allowed to become very large, this model approaches satisfactory agreement with the data. Physically this makes some sense. As the domain size decreases, and the atoms in each unit cell agitate more violently, the lattice gas model becomes less and less distinguishable from a liquid. Indeed, the best-fit value of $B_{Pb} = 10.2$ is considerably larger than that of bulk Pb in the vicinity of its melting point: $B_{bulk Pb} \sim 6-7$ (ref. 16). Further, optical diffraction simulations show that a disordered lattice gas also produces diffuse rings of scattering, although the ring positions and widths are in poor agreement with experiment (ref. 17).

4.6 Conclusion

We have measured the intensity of several integer-order reflections of Pb/Ge(111) through the $\sqrt{3} (\beta) \rightarrow 1 \times 1$ transition. A structure factor analysis above the transition indicates that the Pb monolayer becomes a 2-d liquid, weakly modulated by the substrate. Several Fourier components of the adsorbate-substrate potential can be estimated, and are of the same magnitude as those found for the intercalation compound $C_{24}Rb$ (ref. 15).

A high-temperature 1×1 phase is a feature common to a great variety of chemisorbed monolayers and submonolayers, as well as to many clean reconstructed surfaces. A surface X-ray diffraction analysis similar to the one presented here should thus be widely applicable.

4.7 References

1. W. Telieps, E. Bauer, Surf. Sci. 162, p. 163 (1985).
2. J. C. Campuzano, M. S. Foster, G. Jennings, R. F. Willis, W. Unertl, Phys. Rev. Lett. 54, p. 2684 (1985).
3. M. Schick, Progress in Surf. Sci. 11, p. 245-292 (1981).
4. G. Reiter and S. C. Moss, Phys. Rev. B33, p. 7209-7217 (1986).
5. M. Born, E. Wolf in "Principles of Optics" Chap. XII, Pergamon Press (1980).

6. D. Forster in "Hydrodynamic Fluctuations, Broken Symmetry and Correlation Functions", Chap. 2, W A Benjamin (1975).
7. T. Ichikawa, Solid State Comm. 46 p.827-831 (1983) T. Ichikawa, Solid State Comm. 49, p. 59-64 (1984).
8. R. Feidenhans'l, J. S. Pedersen, M Nielsen, F. Grey, R. L. Johnson, Surf. Sci. 178, p. 927-933 (1986).
9. J. S. Pedersen, R. Feidenhans'l, M. Nielsen, K. Kjaer, F. Grey, R. L. Johnson, Surf. Sci. 189/190, p. 1047-1054 (1987).
10. B. W. Batterman, D. R. Chipman, Phys. Rev. 127, p. 690-693 (1962).
11. J. J. Metois, G. Le Lay, Surf. Sci. 133, p. 422-442 (1983).
12. B. P. Tonner, H. Li, M. J. Robrecht, M. Onellion, J. L. Erskine, Phys. Rev. B36 p. 989-997 (1987).
13. G. Le Lay, J. Peretti, M. Hahnbuecken, W. S. Yang, Surf. Sci. 204, p. 57-68 (1988).
14. S. Alexander, Phys. Lett. A54, p. 353 (1975).
15. S. C. Moss, G. Reiter, J. L. Robertson, C. Thompson, J. D. Fan, Phys. Rev. Lett. 57, p. 3191-3194 (1986).
16. E. J. Lisher, Acta Cryst. A32, p. 506-509 (1976).
17. S. C. Moss, H. Zabel, Surf. Sci. 97, p. L357-L362 (1980).

5. STUDY OF THE PHASE DIAGRAM OF Pb/Ge(111)

Abstract: We have made surface X-ray diffraction measurements of Pb/Ge(111) as a function of temperature and Pb coverage in order to map out a phase diagram. Below $1/3$ ML, the $\sqrt{3} \times \sqrt{3}R30^\circ$ α -phase is found to coexist with a 1×1 phase. Between $1/3$ ML and $4/3$ ML, the α and β -phases form a simple two-phase system displaying phase separation. We emphasize analogies between the experimental phase diagram of Pb/Ge(111) and simple theoretical phase diagrams.

5.1 Introduction

In previous studies (ref. 1, 2, Chap. 2, 3) we have investigated the three stable phases of Pb/Ge(111): the $\sqrt{3} \times \sqrt{3}R30^\circ$ α and β -phases and the high temperature 1×1 phase. In this chapter we determine the boundaries between the different phases by measuring variations in the intensity of the $(2/3, 2/3)$ reflection of the $\sqrt{3}$ structure, for coverages between 0 and $4/3$ ML and from room temperature to 400° C. The resulting phase diagram is similar to one proposed by Ichikawa (ref. 3) on the basis of RHEED measurements. The main differences are in the assignment of the saturation coverage of the α -phase ($1/3$ ML rather than $2/3$ ML in ref. 3) and in the labelling of certain regions as mixed phase rather than pure.

In a mixed phase region, the relative concentration of each phase at a given temperature can be deduced from a lever rule (ref. 4). We investigate the effect of the lever rule on diffraction measurements for some simple model phase diagrams, and show how comparison between the model predictions and experiment yields useful information concerning the boundaries of the mixed phase region.

Near completion of the β -phase, we have made detailed sample-rotation (ω) scans of the $(2/3, 2/3)$ surface reflection as a function of temperature. The $(2/3, 2/3)$ reflection displays pronounced broadening near the transition to the 1×1 phase at $\sim 180^\circ$ C, even though the transition is first order. We draw attention to similar observations, made in studies of physisorbed gases on graphite near completion of a first adsorbed monolayer, and which are believed to be due to finite-size effects.

5.2 Theory

In this section we consider a simple two-phase lattice gas system, deduce the lever rule in the mixed phase region, and derive the consequences of the lever rule for two model phase diagrams.

Fig. 5.1a shows the theoretical phase diagram of a simple lattice-gas, where sites on a square lattice are either occupied or empty (ref. 5). There are only nearest neighbour attractive interactions between atoms, which makes it energetically more favourable for the filled and empty sites to cluster into two separate domains. In thermal equilibrium at any non-zero temperature, the domain of filled sites (the f-phase) will contain a number of empty sites $N_e(T)$ which increases as the temperature rises. Likewise, there will be an equilibrium concentration of filled sites $N_f(T)$ in the empty domain (e-phase). If the empty domain contains N sites, $\theta_e(T) = N_f(T)/N$ defines the maximum solubility of filled sites in the empty domain, and is called the solvus line of the e-phase. Similarly, if the filled domain has N' sites, $\theta_f(T) = 1 - N_e(T)/N'$ defines the solvus line of the f-phase.

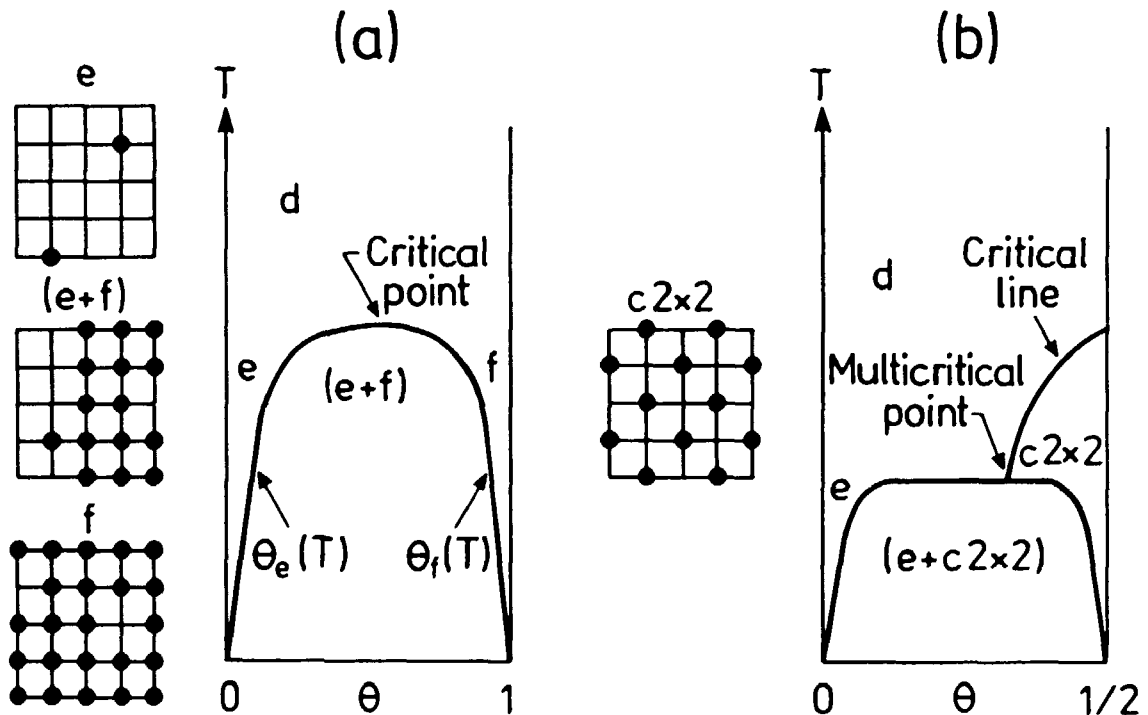


Fig. 5.1a,b: Phase diagrams for lattice-gas on a square lattice (a) is for nearest-neighbour attractive interactions only, (b) is for nearest-neighbour repulsion and weaker next-nearest-neighbour attraction, yielding a $c2 \times 2$ structure at $\theta = \frac{1}{2}$. The letters e, f, d indicate empty, filled and disordered phases, respectively.

Physically, the shape of the solvus lines is determined by the interaction energies of atoms on the surface. For instance, repulsive nearest-neighbour interactions and attractive next-nearest-neighbour interactions will stabilize a lattice-gas $c(2 \times 2)$ structure, with a line of critical points at high temperature which separates the $c(2 \times 2)$ phase and a disordered "fluid" phase (Fig. 5.1b). This line terminates at the mixed phase region in a multicritical point. An analogous phase diagram applies on a triangular lattice, except that the ordered phase is then a simple (α -phase) $\sqrt{3} \times \sqrt{3}$ structure. If phase boundaries can be determined accurately enough by experiment, it is possible to deduce the adatom interactions, on the assumption that the system behaves as a simple lattice gas (ref. 5).

At a given coverage θ and temperature T in the mixed phase ($e + f$) region, the relative amounts of the two phases are determined by $\theta_e(T)$ and $\theta_f(T)$, the positions of two solvus lines, because they define the coverage in the two domains that together form the mixed phase. If x is the fraction of f -phase on the surface, then

$$x \theta_f(T) + (1-x) \theta_e(T) = \theta \quad (5.1)$$

and hence

$$x = \frac{\theta - \theta_e(T)}{\theta_f(T) - \theta_e(T)} \quad (5.2)$$

Although this lever rule has been derived for a lattice gas, it is applicable to any mixed phase region, irrespective of the detailed nature of the phases. Ideally, the equilibrium configuration of the mixed phase is one macroscopic domain of each phase. For surface phases, however, terraces will effectively isolate microscopic regions on the surface, each one behaving as a separate system. This has the advantage that the X-ray measurement averages over a large number of systems, but the inconvenience that finite-size effects may play a large and difficultly controllable role.

Care must be taken when applying the lever rule to the analysis of diffraction measurements: the value of x gives the fraction of the surface covered by the f -phase, but the intensity of Bragg scattering from that phase will depend on the concentration of empty sites in it. For a lattice-gas, the structure factor per unit cell of an f -phase domain can be written

$$F(q) = \frac{1}{N'} \left(f_A(q) \sum_m e^{iq \cdot r_m} - f_A(q) \sum_n e^{iq \cdot r_n} \right) \quad (5.3)$$

m: summation over all N' sites in the domain

n: summation over N_e empty sites in domain

where the notation of Chap. 2 is employed. Assuming the r_n are randomly distributed on the lattice, the second summation in Eqn. 5.3 is on average zero, except at Bragg reflections, where the structure factor becomes

$$F(q) = \frac{1}{N'} (N' f_A(q) - N_e f_A(q)) = \theta_f(T) f_A(q) \quad (5.4)$$

Away from the Bragg reflections, the second summation in Eqn. 5.3 will result in scattered intensity $N_e f_A^2(q)$, identical to that for an ideal gas (Eqn 3.6). It is interesting to note that the vacancies thus form a "modulated" gas, in the sense of chapter 4, with isotropic scattering plus Bragg contributions.

For the case where the f-phase has a superstructure, as in Fig 5.1b, the fractional-order Bragg intensity will be due only to the f-phase domains. The integrated intensity $I(\theta, T)$ of a Bragg peak at a given coverage θ and temperature T is proportional to the total number of scatterers in the f-phase and so

$$I(\theta, T) = x \theta_f(T) I_0 \quad (5.5)$$

I_0 : integrated intensity for saturation coverage $\theta = 1/2$ at $T = 0$

From a temperature scan it is possible to deduce one of the solvus lines if the other is known. If, for example, $\theta_f(T)$ is known, then from Eqns 5.2 and 5.5,

$$\theta_e(T) = \frac{\theta - I(\theta, T)/I_0}{1 - I(\theta, T)/(I_0 \theta_f(T))} \quad (5.6)$$

The shape of the solvus lines bounding a mixed phase region can therefore be deduced in two ways: directly, by measuring the temperature at which the scattering due to one of the phases disappears, and indirectly, because of variation in scattered intensity from the constituent phases, due to the lever rule.

To illustrate the effect of the lever rule, we consider two idealized examples. In Fig. 5.2a, a "fluid" phase and an ordered α -phase coexist for $T < \theta'$, on a normalized temperature and coverage scale. The figure implies that the saturation concentration of vacancies in the α -phase is negligible at all temperature, in other words $\theta_f(T) = 1$. Applying the lever rule to this phase diagram, the concentration of α -phase as a function of temperature is deduced for several different coverages (Fig 5.2b). Fig 5.3a shows the mixed phase region of a

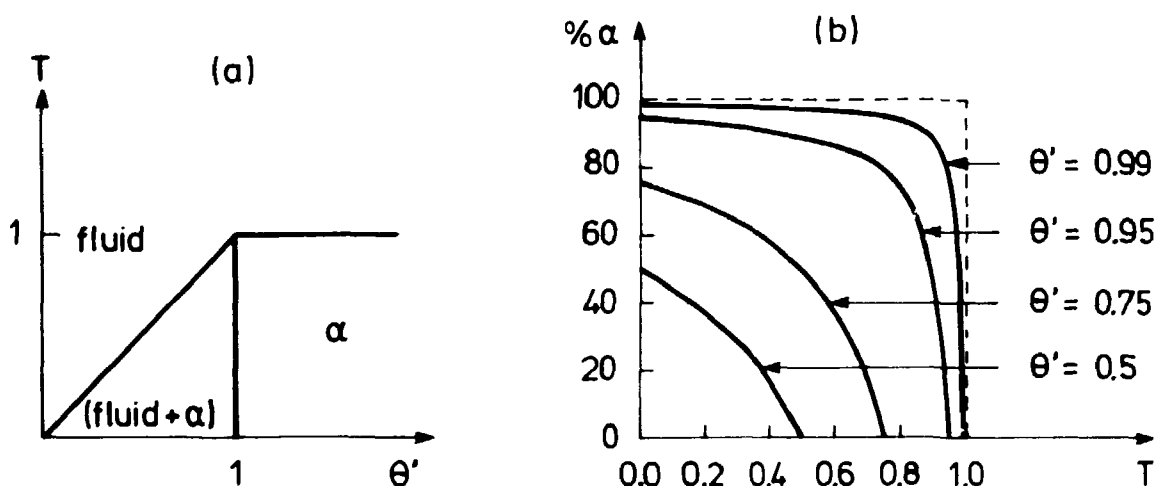


Fig. 5.2a,b: (a) Idealized phase diagram, (b) concentration of the ordered phase α as a function of temperature for several coverages.

textbook binary system, where the concentration of two phases α and β depends on the coverage θ' of a given substance. In Fig. 5.3a the constituents of the β -phase (for example, atoms) are soluble to a limited extent in the α -phase, but not vice-versa. At the triple line, $T = 1$, α and β -phases coexist over a range of coverages with a high-temperature fluid phase. Above $T = 1$, the fluid phase coexists with either the α -phase, below an eutectic coverage θ_{eut} , or with the β -phase, above θ_{eut} . For coverages below $\theta' = \theta_{eut}$, the concentration of β phase

will drop discontinuously to zero on crossing the triple line in a temperature scan, except below coverages $\theta' = 0.1$, where the lever rule results in a nearly linear decay of β -phase as a function of temperature (Fig. 5.3b).

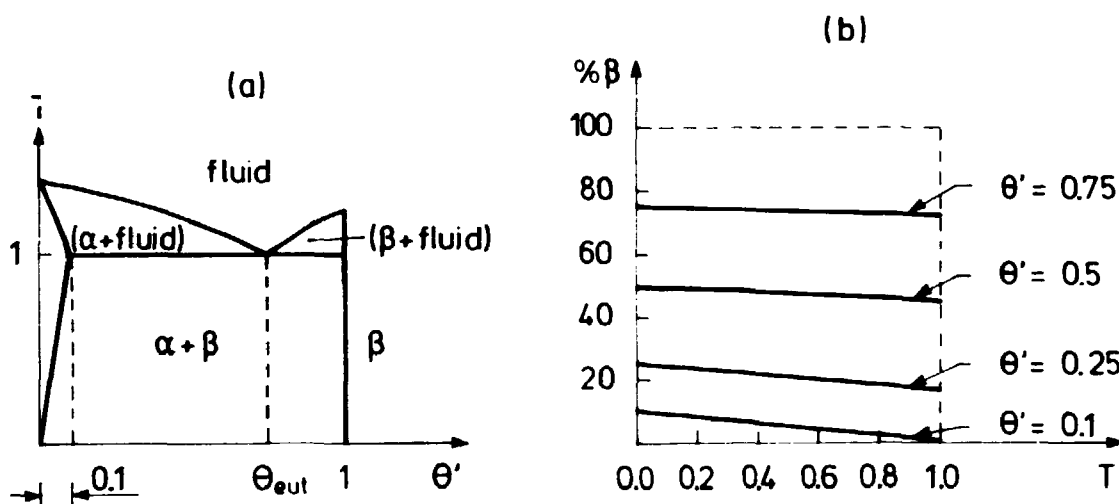


Fig. 5.3a,b: (a) Idealized phase diagram for a binary system, (b) concentration of β -phase as a function of temperature.

These two examples illustrate an important point: the lever rule can produce deceptively continuous-looking transitions. Further, if we assume that the average linear dimension of the domains of a certain phase scales with the concentration of that phase, then Bragg reflections may show pronounced broadening at a first order transition, simply due to the lever-rule variation of the concentration of one component (Eqn 2.9). Thus, continuous intensity decay or peak broadening is not sufficient evidence for concluding a transition is itself continuous, unless this can be supplemented with reliable information about the phase diagram.

5.3 Experimental Method

The data presented here were measured at the wiggler beamline W1 in HASYLAB ($\theta > 1\text{ML}$) and also at a 12kW rotating anode at Risø National Laboratory ($\theta < 1\text{ML}$); the X-ray wavelength was 1.38 Å and 1.54 Å ($\text{CuK}\alpha$), respectively.

Rise measurements: The goal was to investigate the phase diagram up to 400° C by monitoring the intensity of the (2/3, 2/3) reflection. As discussed in chapter 1, desorption is roughly .04ML/min at 400° C. Even at the wiggler beamline, an ω -scan of a surface reflection requires several minutes, and so it is out of the question to make such scans at or near 400° C on a rotating anode. Instead, the resolution of the diffractometer was relaxed (graphite monochromator, no exit slits) to 0.5° in ω for the (2/3, 2/3) reflection, so that the room-temperature peaks were resolution limited at all coverages. Under such conditions, the peak intensity is proportional to the integrated intensity, and hence to the structure factor intensity.

Using the method described in chapter 2, the coverage was determined to be $1.33 \pm .05$ ML at the beginning of the experiment. The coverage was varied in-situ by heating the sample briefly to 420° C. The intensity of the (2/3, 2/3) reflection at room-temperature, after successive desorptions, can be used in conjunction with Table 2.3 to determine the coverage. Below 1/3ML, the coverage is estimated using Eqn. 5.5, and assuming $\theta_f(T) = 1$ and $\theta_e(T) = 0$ at room temperature.

At each coverage, temperature scans of the peak intensity were made up to 400° C. The temperature was measured by thermocouple, and set by varying the current to the sample. Above 350° C, the temperature was changed in steps of $\sim 10^\circ$ and the counting time was 10s. Despite these precautions, slight desorption did occur, and this is included in the estimated errors on the coverage.

Hasylab measurements: The sample alignment and coverage calibration is described in chapter 2. The incidence angle was 1°. At each coverage, detailed ω -scans of the (2/3, 2/3) reflection were made as a function of temperature, which was measured by a thermocouple. No change in coverage was detected after several cycles at temperatures up to 190° C.

5.4 Overview

To give an overview of the various measurements, some representative temperature scans are sketched in Fig. 5.4 . First we consider the main qualitative features of these results.

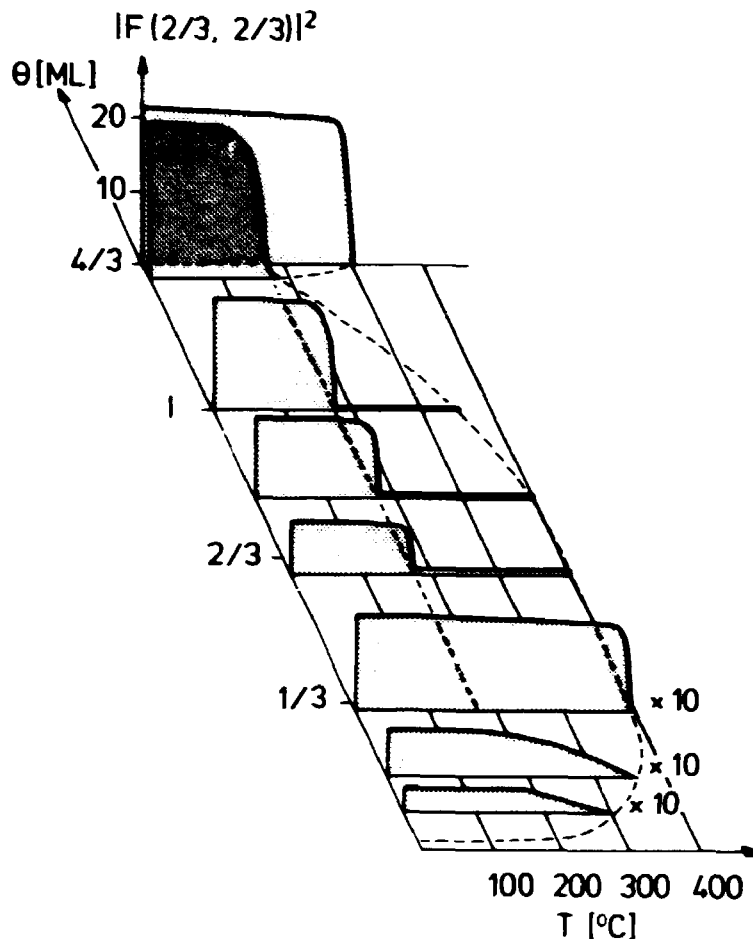


Fig. 5.4: Sketch of several scans of the (2/3, 2/3) structure factor intensity, as a function of coverage and temperature. The scans have been scaled to the room-temperature structure factor intensities, based on the coverage estimate for each scan.

At low coverages ($< 0.2\text{ML}$) the temperature scans show a smooth decay of intensity to zero. As the coverage increases, the transition to a 1×1 phase occurs at successively higher temperatures, and is increasingly abrupt. This is in close analogy with the lever-rule expectations for a phase diagram similar to Fig 5.2a, where $\theta' = 3\theta$ and $T = 1$ corresponds to 400°C .

Beyond $1/3\text{ML}$, a clear feature in the temperature scans is a triple-line at $175 \pm 5^\circ\text{C}$. At this temperature the $(2/3, 2/3)$ intensity drops abruptly to a small but finite value. The intensity of the $(2/3, 2/3)$ above the triple line decreases with increasing coverage, in accordance with a lever rule for a mixed phase ($\alpha + 1 \times 1$) region above the triple line. At $1.25 \pm 0.1\text{ML}$, there is no measurable intensity above the triple line. We thus identify the point $(1.25\text{ML}, 175^\circ\text{C})$ as the eutectic.

Beyond the eutectic coverage, the transition temperature to the 1×1 phase rises steeply to 300°C for a nominally complete β -phase. In a previous measurement (Chap. 3, Fig. 3.4), it was found that the β -phase and fluid 1×1 phase coexist over a finite temperature range below 300°C , hence this region is assigned to be a mixed phase ($\beta + 1 \times 1$).

These results are summarized in a phase diagram in Fig. 5.5, where disappearance or abrupt change of the $(2/3, 2/3)$ intensity is marked by filled circles (Risø data) or triangles (HASYLAB data). Open circles indicate room temperature measurements (see Chap. 2). Bold lines are guides to the eye, dashed lines are suggested by comparison with analogous systems: a lattice-gas model for $\theta < 1/3 \text{ ML}$, and a binary system for $1/3 \text{ ML} < \theta < 4/3 \text{ ML}$.

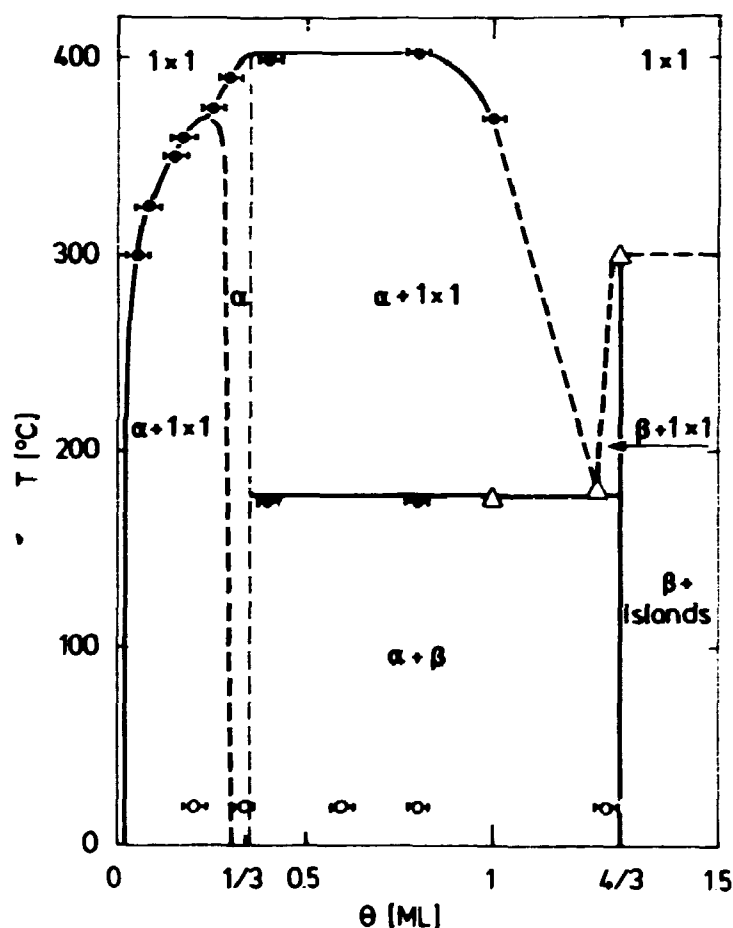


Fig. 5.5: Phase diagram for Pb/Ge(111). Full circles: Risø measurements. Triangles: Hasylab measurements. Open circles: Room temperature structure determinations. Bold lines are guides to the eye, dashed lines are suggested.

5.5 Analysis

$\theta < 1/3\text{ML}$: Fig. 5.6 shows a typical temperature scan of the $(2/3, 2/3)$ peak in the region below $1/3\text{ML}$. The temperature at which the intensity in the $(2/3, 2/3)$ reflection reaches background level defines a point on the solvus line of the 1×1 phase. As discussed in Section 5.2, it is in principle possible to determine the

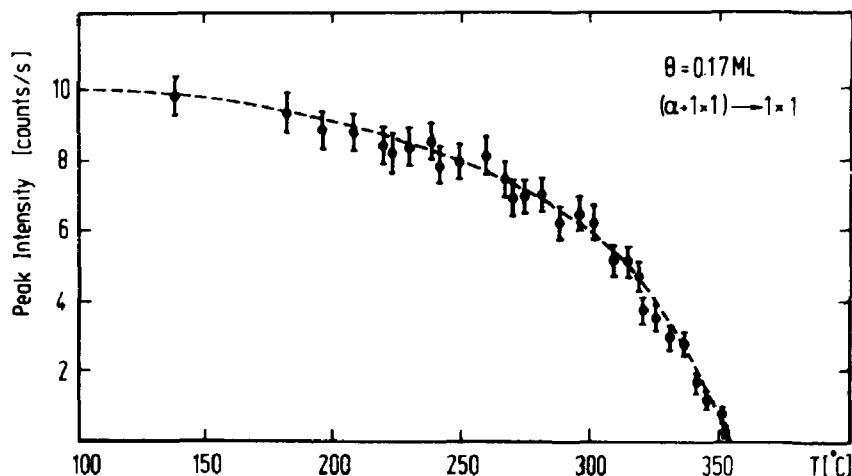
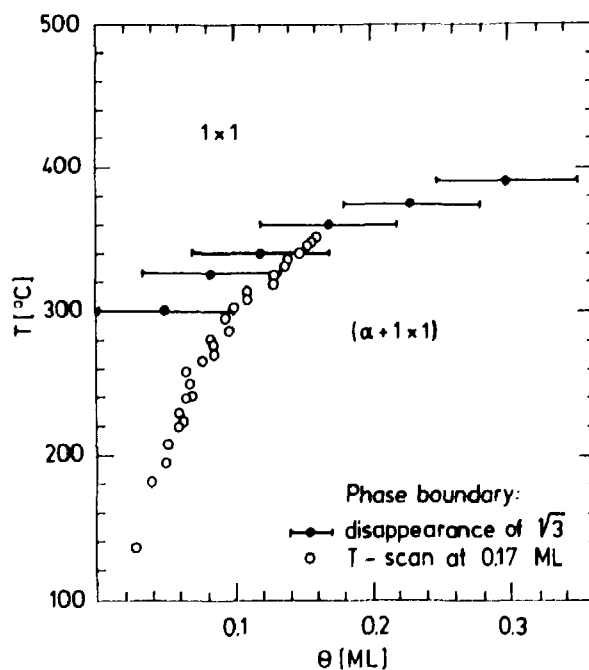


Fig. 5.6: Temperature scan of $(2/3, 2/3)$ at $0.17 \pm 0.05 \text{ ML}$.

shape of the solvus lines bounding the mixed phase region from temperature scans like Fig. 5.6. In practice there are several complications: the temperature dependence of the Debye-Waller factor, possible broadening of the peak near the transition, uncertainty on the coverage θ . Further, it is necessary to know the functional form of one of the solvus lines in order to determine the other (see Eqn. 5.6).

Fig. 5.7:
Phase boundary between 1×1 phase and $(1 \times 1 + \alpha)$. Full circles: as determined from disappearance of $(2/3, 2/3)$ signal in temperature scans. Open circles: using lever rule and temperature scan in Fig. 5.6.



Making the assumption that the α -phase solvus line is $\theta_{\alpha}(T) = 1/3$, then the 1×1 solvus line can be deduced from Eqn. 5.6. The result is compared in Fig. 5.7 with the points on the solvus line obtained by directly monitoring the temperature at which the fractional-order peaks disappear. Given the limitations mentioned above, the agreement is quite reasonable.

1/3ML < θ < 1ML: Fig. 5.8 shows a temperature scan of the $(2/3, 2/3)$ peak across the triple line at 0.4 ± 0.05 ML. The coverage has been calibrated by two means. First, from the intensity of the $(\alpha + \beta)$ phase well below the transition compared with a pure β -phase, as discussed in section 5.3. Secondly, by comparing the $(\alpha + \beta)$ intensity below the transition with that of the $(\alpha + 1 \times 1)$ mixed phase just above the transition, and applying the lever rule for $(\alpha + 1 \times 1)$, assuming the eutectic to be at 1.25ML. For the three coverages 0.4, 0.8 and 1.0 ML where temperature scans were made, the agreement between these two independent estimates of the coverage is better than $\pm 10\%$.

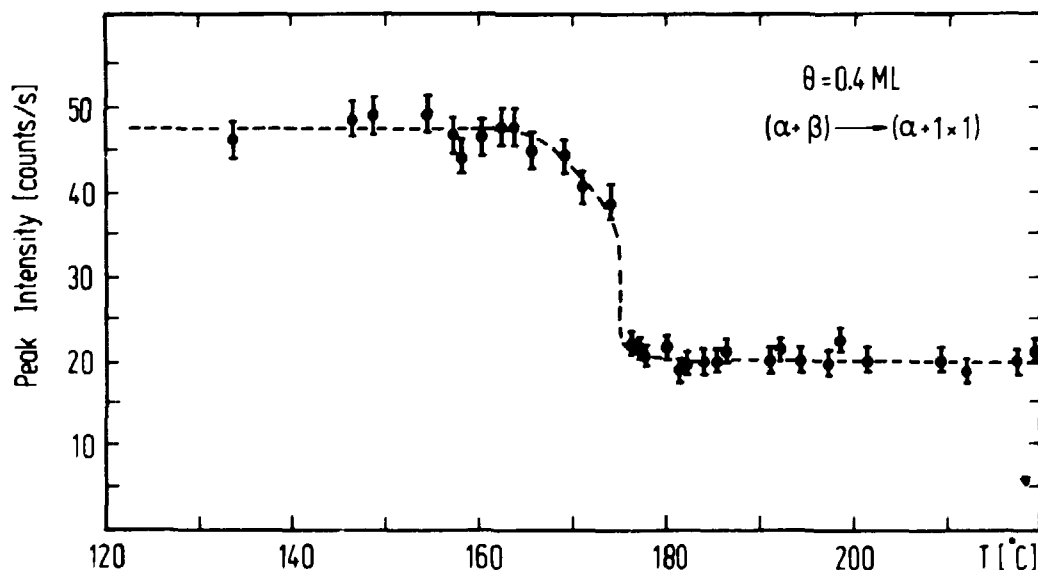


Fig. 5.8: Temperature scan of $(2/3, 2/3)$ at 0.4 ± 0.05 ML, in the vicinity of the triple line.

The intensity drops abruptly at the triple line, even for the 0.4 ML scan. By comparison with Fig. 5.3b, this suggests that the α -phase solvus line bounding the $(\alpha + \beta)$ region is very close ($<.06\text{ML}$) to the line $\theta = 1/3$. We do not, however, expect the solvus lines above and below $\theta = 1/3$ to be symmetric: it is generally energetically more expensive to create interstitials than vacancies (ref. 5).

$\theta = 1\text{ML}$: The ω -scans were analysed by least-square fits to the lineshape. A Lorentzian is used (empirically) and provides good fits ($\chi^2 < 2$) at all temperatures. The integrated intensity of the fitted Lorentzian is plotted in Fig.5.9 for scans through the triple-line in both directions. There is a hysteresis of 3°C at the transition. Scans performed at a fixed temperature near the transition at five minute intervals showed no measurable variation, suggesting that the hysteresis is intrinsic to the transition. Near the triple-line, the peak broadens considerably.

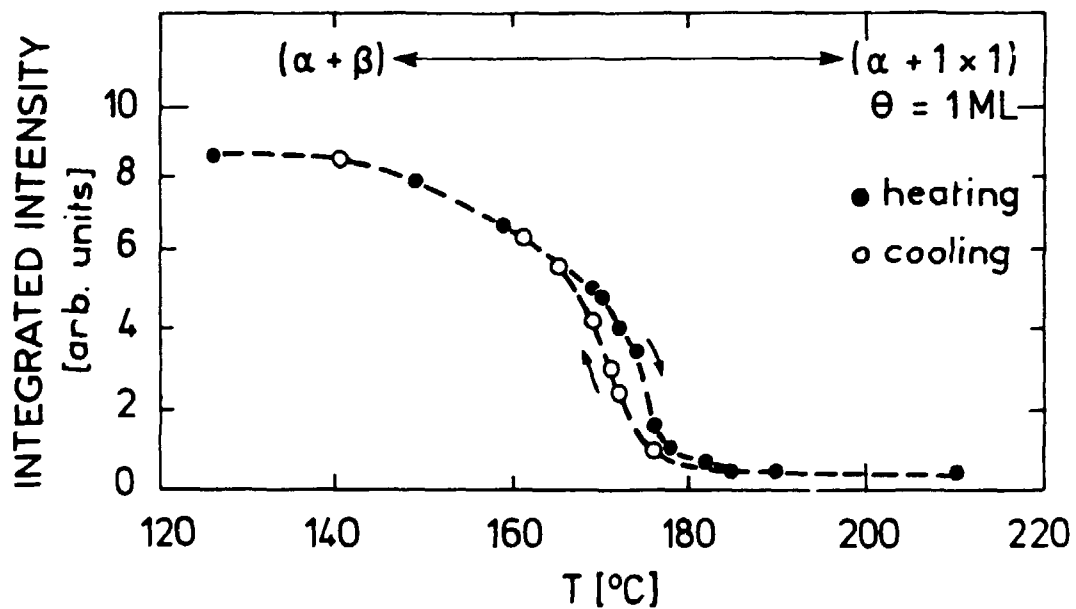


Fig. 5.9: Integrated intensity of Lorentzian fit to $(2/3, 2/3)$ as a function of temperature, $\theta = 1.0 \pm 0.05 \text{ ML}$.

The variation of the Lorentzian FWHM is illustrated in Fig 5.10. The largest contribution to the experimental resolution for ω -scans is from the finite angle subtended by the detector perpendicular to the surface, and is estimated to be $5.5 \times 10^{-3} \text{ \AA}^{-1}$. The experimental resolution was the same for the 1.3ML and 1.33ML data discussed below. A typical ω -scan and parameters of the best-fit Lorentzians are given in the Appendix.

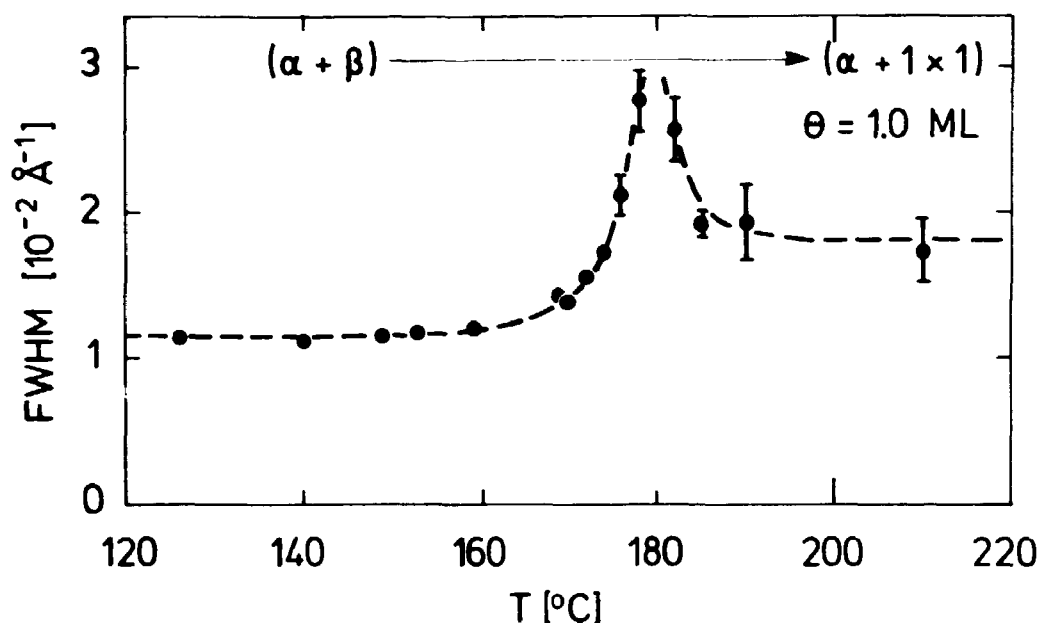


Fig. 5.10: FWHM of Lorentzian fit to $(2/3, 2/3)$ as a function of temperature, $\theta = 1.0 \pm 0.05$ ML.

$\theta = 1.3$ ML: A Lorentzian lineshape fits the experimental data well ($\chi^2 < 2$) except in the range 170-180° C, where $\chi^2 > 5$. Inspection shows that the lineshape has broader wings than a Lorentzian. Best agreement was obtained by a sum of two Lorentzians, one with the width due to instrumental broadening, and the other several times broader. The appearance of a broad component of scattering near the transition is characteristic of the short-range-order (SRO) scattering at a second order transition, due to divergence of the susceptibility of the system to fluctuations (ref. 6). The data was therefore analysed near the transition as a sum of SRO and long-range-order (LRO), the latter being resolution-limited. Above 184° C there is no LRO component, while below 170° C the SRO is too weak to be fitted reliably.

The amplitude of the LRO component is shown in Fig. 5.11 for heating and cooling scans. Again, hysteresis of 2.7° C is seen, indicative of a first order transition. Nevertheless, the FWHM and amplitude of the SRO component display the characteristics of a second-order transition, namely peaking and sharpening of the SRO near the transition temperature (ref. 6), as displayed in Fig. 5.12 and 5.13. A typical ω -scan and parameters of the best-fit Lorentzians are given in the Appendix.

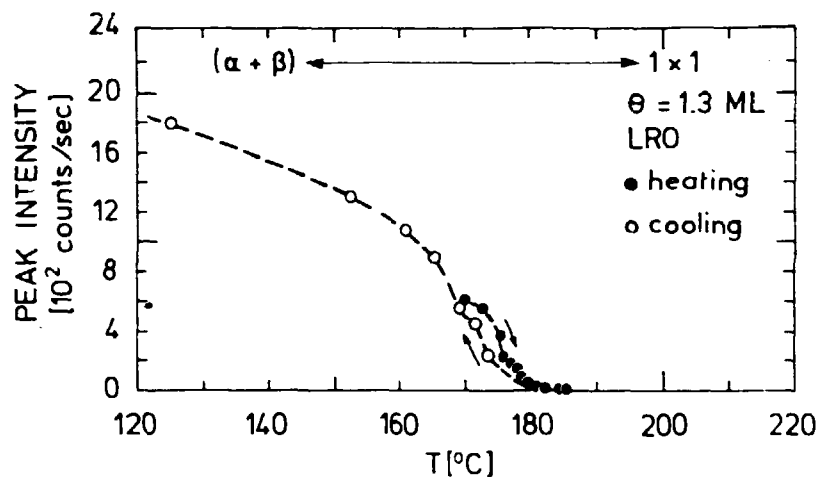


Fig. 5.11: Long-Range-Order (LRO) peak intensity from Lorentzian fit to (2/3, 2/3) as a function of temperature, $\theta = 1.3 \pm 0.05$ ML.

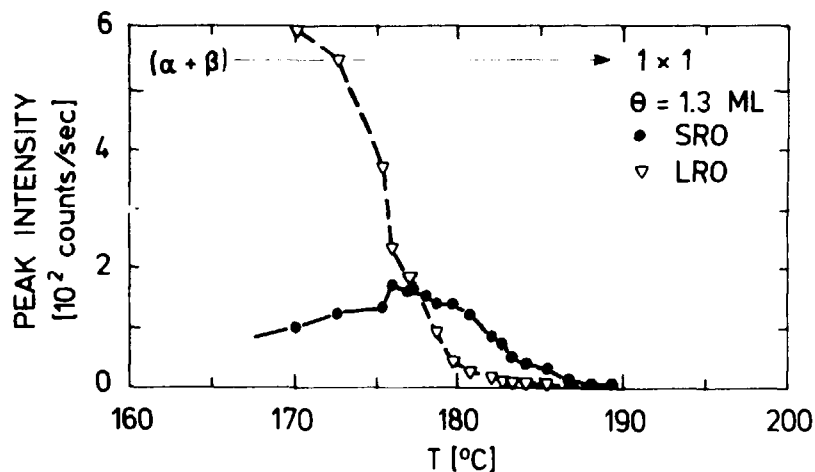


Fig. 5.12: Short-Range-Order (SRO) peak intensity from Lorentzian fit, as a function of temperature, $\theta = 1.3 \pm 0.05$ ML. Heating scan only.

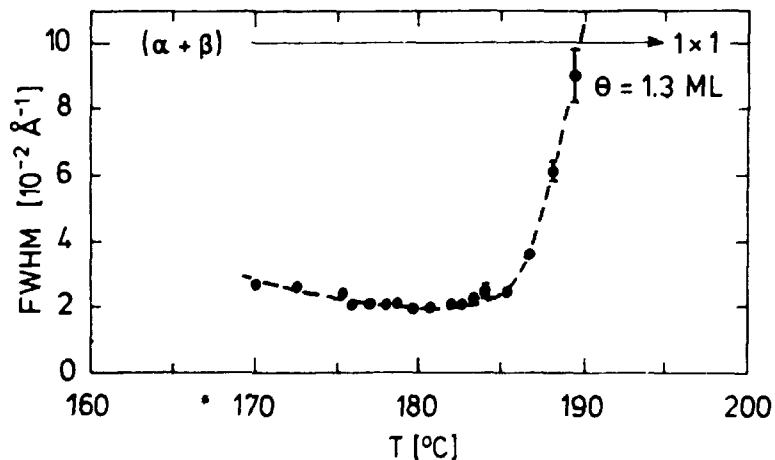


Fig. 5.13: FWHM of Short-Range-Order (SRO) component of (2/3, 2/3), as a function of temperature, $\theta = 1.3 \pm 0.05$ ML. Heating scan only.

$\theta = 1.33$ ML: At a nominally complete β -phase, the transition temperature rises to 301°C . A Lorentzian fit to the measured lineshape is good at all temperatures ($\chi^2 < 4$). The peak intensity of the fitted Lorentzian is plotted in Figure 5.14. Hysteresis was not measured for this transition. There is no measurable variation in the FWHM of the lineshape near the transition temperature. The absence of

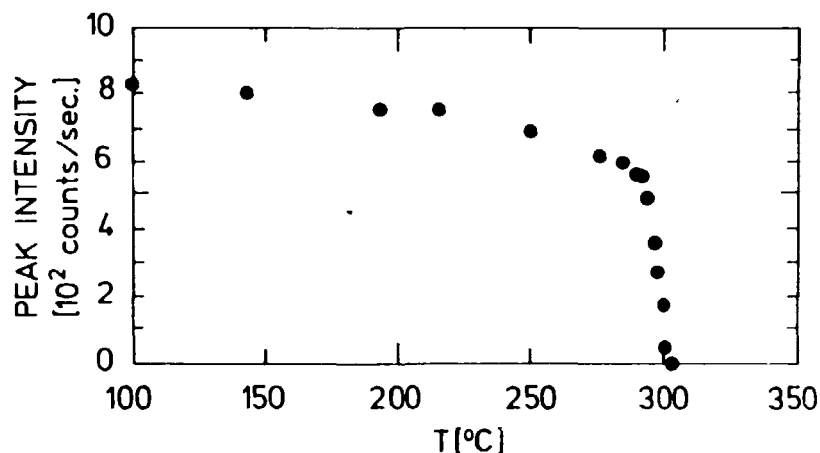


Fig. 5.14: Peak intensity of Lorentzian fit to $(2/3, 2/3)$ as a function of temperature, $\theta = 1.33 \pm 0.05$ ML.

any critical scattering suggests the transition is first-order, in agreement with the measurement of coexistence of β and 1×1 phases for the same coverage and transition temperature (Chapter 2). Parameters of the best-fit Lorentzians are given in the Appendix.

The existence of a mixed phase ($\beta + 1 \times 1$) region, even for a nominally complete β -phase, deserves comment. As a Bragg peak reflects only the ordered structure, the reconstruction may have a non-negligible defect concentration. The absolute coverage may therefore be somewhat less than estimated by structure factor analysis. Thus it may prove experimentally difficult to probe the $\beta \rightarrow 1 \times 1$ transition at precisely $\theta = 4/3$ ML.

5.6 Discussion

Here we consider in more detail the implications of the ω -scans of the $(2/3, 2/3)$ reflection near completion of the β -phase. The observation of peak broadening at

1.0ML and what appears to be SRO scattering at 1.3ML is somewhat surprising, since the transition across a triple line is expected to be first-order. We note that the shrinking of domain size, discussed in section 5.2 in connection with the lever rule, cannot account for the observed peak broadening, since the temperature scans are made at coverages very far from the α -phase solvus line. The transition should therefore be abrupt, without broadening.

The appearance of effects associated with a second-order transition in a region of a phase diagram where transitions should strictly be first-order has been termed "incipient criticality" by Ostlund and Berker (ref. 7). These authors have been able to reproduce the experimental phase diagrams of N_2 /graphite and Kr/graphite near completion of a dense-packed phase by including the effects of finite-size in calculations of a lattice gas phase diagram. The ideal phase diagram of these systems is essentially that of Fig. 5.1 b, except that the solid phase is $\sqrt{3} \times \sqrt{3}R30^\circ$, since the substrate lattice is triangular.

In an infinite system the correlation length of fluctuations would diverge at a second-order transition, but for the finite-size system, and a range of temperatures where the theoretical correlation length is larger than the average domain-size, the transition is smeared. This alters the form of the phase diagram in the region of the multicritical point considerably: the line of critical points separating the $\sqrt{3}$ solid and the fluid phase (as in Fig 5.1b) broadens into a mixed phase region. This feature is observed experimentally. In addition, the specific heat measurements of N_2 /graphite (ref. 8) show broad maxima in the transition from ($\sqrt{3}$ solid+fluid) to fluid phase, which should not occur for a first-order transition. The specific heat peaks sharpen on approaching the multicritical point which terminates the phase boundary between the dense-packed solid phase and the fluid phase, near completion of a first N_2 monolayer. Ostlund and Berker contend that this incipient criticality is a further consequence of the smearing of the transition.

Although Ostlund and Berker were concerned with a simple lattice-gas phase diagram, the finite-size smearing they discuss is clearly of general relevance to second-order surface phase transitions. It is possible to speculate how such effects might apply to the phase diagram of Pb/Ge(111): the ($\beta + 1 \times 1$) region in Fig. 5.5 could, for example, be due to a smeared critical line between the pure β phase and the 1×1 liquid phase. The multicritical point for the infinite system would then be identical with the eutectic, and incipient criticality would be observed approaching this point along the triple-line. One other result fits in this picture: the apparent first-order nature of the $\beta \rightarrow 1 \times 1$ transition at $300^\circ C$ is consistent

with a transition through a mixed-phase ($\beta + 1 \times 1$) region, occurring due to the finite-size smearing of the critical line. However, to test the above speculations will require considerably more information about the transition than is at present available.

5.7 Conclusions

We have made surface diffraction measurements of the $(2/3, 2/3)$ reflection of the $\sqrt{3}$ structure of Pb/Ge(111) as a function of temperature for several coverages between 0 and $4/3$ ML. The resulting phase diagram is illustrated in Fig. 5.5. Below $1/3$ ML, the α -phase coexists with a 1×1 phase, and there is close analogy with the phase diagram of a lattice-gas with nearest-neighbour repulsion. In the range $1/3$ ML to $4/3$ ML, the α and β -phases form a binary system which exhibits phase separation. The triple line is at $175 \pm 5^\circ$ C and the eutectic is at 1.25 ± 0.1 ML. Near completion of the β -phase at $1.3 \pm .05$ ML, the transition to a 1×1 phase at the triple line displays features characteristic of a second-order transition. This observation is similar to measurements near the completion of dense packed layers of certain physisorbed gases on graphite.

5.8 References

1. R. Feidenhans'l, J. S. Pedersen, M. Nielsen, F. Grey, R. L. Johnson, Surf. Sci. 178, p. 927-933 (1986).
2. J. S. Pedersen, R. Feidenhans'l, M. Nielsen, K. Kjaer, F. Grey, R. L. Johnson, Surf. Sci. 189/190, p. 1047-1054 (1987).
3. T. Ichikawa, Solid State Comm. 46, p.827-831 (1983).
4. R. A. Swalin, "The Thermodynamics of Solids", Wiley (1972), Chapter 10.
5. M. G. Lagally, T. M. Lu, D. G. Welkie, J. Vac. Sci. Tech. 17, p.223-230 (1980) and references therein.
6. W. N. Unertl, Comm. Cond. Mat. Phys. 12, p. 289-323 (1986).
7. S. Ostlund, A. N. Berker, Phys. Rev. Lett. 42, p. 843-846, (1979).
8. T. T. Chung, J. G. Dash, Surf. Sci. 66, p. 559-580, (1977).

APPENDIX

The Tables A1-A3 give the parameters of least-squares line-shape fits to the ω -scans at 1.0, 1.3 and 1.33 ML, discussed in Chapter 5. All data is for heating scans. For the 1.0ML and 1.33 ML data, a single Lorentzian is used; an example is given in Fig. A1. For the 1.3ML data, two Lorentzians are required to give a good fit in the range 170°-184° C; an example is given in Fig. A2.

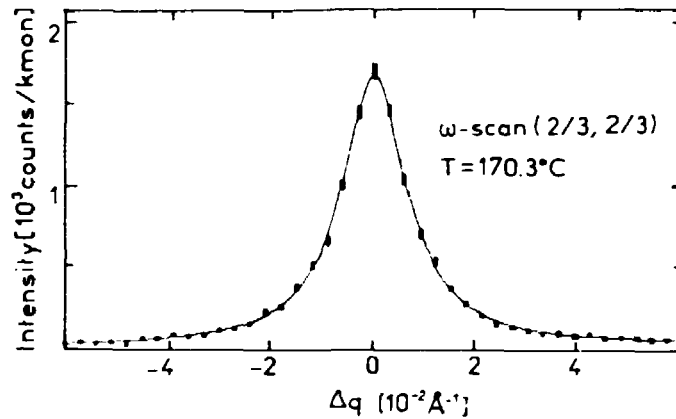


Fig. A1: typical ω -scan for data in Table A1. Fitted Lorentzian is shown.

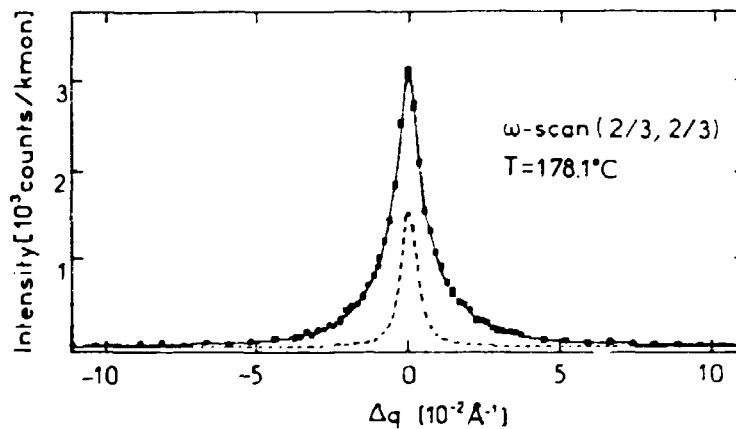


Fig. A2: typical ω -scan for data in Table A2. Fit with two Lorentzians is shown, as well as the LRO component (dashed).

The FWHM values given in all tables are as obtained from the fit. For Table A1, the fitted peak intensity of the Lorentzian is given. Note that in Chapter 5, the integrated intensity of the Lorentzian was plotted to illustrate more clearly the hysteresis. In Table A2, I(LRO) and I(SRO) are the fitted peak intensities of the

Long-Range-Order and Short-Range-Order components. The FWHM of the LRO is fixed at $5.5 \times 10^{-3} \text{ \AA}^{-1}$, the estimated resolution broadening. The least squares residual for a fit to a single Lorentzian is given in brackets in the second column. In Table A3, the fitted peak intensity of the Lorentzian is given. The intensity units for all three tables are counts per 100 kilomonitor counts (kmon), 10 kmon being on average 1 second.

T [°C]	χ^2	I [cts/100kmon]	FWHM [\AA^{-1}]
65.3	1.5	2190 (25)	1.08 (1)
126.0	1.3	1770 (25)	1.14 (1)
149.1	1.1	1595 (15)	1.16 (1)
158.7	1.1	1315 (15)	1.18 (2)
159.1	1.4	1365 (20)	1.21 (1)
168.8	0.9	840 (12)	1.43 (2)
170.3	0.9	830 (10)	1.39 (2)
172.0	0.9	630 (8)	1.55 (2)
174.0	0.6	485 (6)	1.71 (3)
175.9	0.8	175 (8)	2.1 (1)
176.1	0.8	90 (6)	2.4 (3)
177.7	1.8	85 (8)	2.8 (2)
182.3	0.9	60 (5)	2.6 (2)
185.0	0.8	54 (3)	1.9 (1)
190.5	0.8	54 (5)	1.9 (3)
210.6	1.2	47 (5)	1.7 (2)
245.4	0.7	43 (3)	1.9 (2)
286.0	1.4	48 (2)	1.7 (1)
318.1	0.9	46 (3)	1.8 (2)
345.5	1.0	52 (2)	1.5 (2)

Table A1: Parameters of least-squares fits to lineshape of (2/3,2/3) ω -scans, $\theta = 1.0 \pm 0.05 \text{ ML}$

T [°C]	χ^2	I(LRO) [cts/kmon]	I(SRO) [cts/100kmon]	FWHM(SRO) [Å ⁻¹]
58.9	1.2 (1.9)	20403 (135)	171 (20)	4.2 (5)
170.0	1.7 (5.7)	6015 (100)	990 (27)	2.71 (7)
172.6	1.0 (5.7)	5505 (75)	1215 (21)	2.58 (4)
175.3	1.3 (4.6)	3687 (78)	1323 (24)	2.40 (4)
176.0	1.6 (11.)	2326 (47)	1694 (17)	2.08 (2)
177.0	1.5 (8.5)	1839 (35)	1603 (13)	2.09 (2)
178.1	1.4 (5.7)	1511 (32)	1520 (12)	2.07 (2)
178.7	1.4 (3.9)	912 (29)	1384 (11)	2.10 (2)
179.7	2.2 (3.0)	428 (33)	1392 (15)	1.92 (2)
180.7	1.1 (1.8)	268 (23)	1201 (13)	1.95 (3)
182.0	1.1 (1.5)	174 (21)	834 (13)	2.08 (4)
182.8	1.2 (1.5)	67 (20)	703 (14)	2.10 (5)
183.4	1.1 (1.2)	70 (22)	495 (17)	2.25 (11)
184.0	1.0	0	385 (25)	2.44 (21)
185.5	0.9	0	302 (5)	2.46 (4)
186.7	1.1	0	96 (3)	3.62 (6)
188.1	1.1	0	36 (2)	6.2 (3)
189.4	1.2	0	19 (2)	9.2 (3)

*Table A2: Parameters of least-squares fits to lineshape of (2/3,2/3) ω -scans,
 $\theta = 1.3 \pm 0.05$ ML*

T [°C]	χ^2	I [cts/100kmon]	FWHM [Å ⁻¹]
100.2	3.0	8230 (100)	0.63 (1)
143.3	3.5	8020 (90)	0.59 (1)
194.0	3.2	7510 (80)	0.58 (1)
216.1	1.8	7490 (60)	0.57 (1)
250.1	3.6	6870 (80)	0.57 (1)
276.7	2.2	6160 (60)	0.58 (1)
285.9	1.6	5970 (50)	0.55 (1)
290.5	2.4	5635 (60)	0.55 (1)
292.3	1.4	5600 (50)	0.53 (1)
294.2	1.8	4905 (50)	0.53 (1)
297.0	1.7	3575 (30)	0.49 (1)
298.0	0.9	2660 (30)	0.50 (1)
300.3	1.1	1650 (25)	0.48 (1)
300.6	1.1	460. (12)	0.61 (1)
303.0	1.3	0.00 (60)	-

Table A3: *Parameters of least-squares fits to lineshape of (2/3,2/3) ω -scans, $\theta = 1.33 \pm 0.05$ ML.*

Summary and Outlook

This report has described several surface x-ray diffraction experiments on the chemisorption system Pb/Ge(111). A structural analysis of room-temperature measurements shows that there are two phases as a function of coverage: the simple $\sqrt{3}\times\sqrt{3}R30^\circ$ α -phase with one atom per unit cell and the $\sqrt{3}\times\sqrt{3}R30^\circ$ β -phase which is a distorted close-packed 2d structure with four atoms per unit cell. Beyond saturation coverage of the β -phase, Pb grows as 3d islands.

By measuring only a few surface Bragg reflections, it is possible to calibrate the Pb coverage accurately from a knowledge of the structure of the room temperature phases. A reliable temperature calibration has been obtained by placing a thermocouple in contact with the back surface of the directly-heated Ge substrate. Desorption of Pb is significant only at temperatures above 300°C , and diffusion into the substrate is negligible. The surface is stable in UHV for periods of up to two weeks. Transitions between the phases are easily detectable in diffraction measurements. It can be concluded that Pb/Ge(111) is an ideal chemisorption system with which to investigate surface phases and phase transitions.

In the high-temperature 1×1 phase of Pb/Ge(111), we have measured a weak isotropic halo of scattering consistent with a 2d liquid phase. Measurements of the integer-order Bragg reflections through the $\sqrt{3}(\beta) \rightarrow 1\times 1$ phase favour the 2d liquid model, provided the modulating effect of the periodic substrate on the liquid is taken into account. By measuring variations of the intensity of the $(2/3, 2/3)$ surface reflection as a function of coverage and temperature, we have deduced a simple phase diagram for Pb/Ge(111) in the monolayer coverage regime. We have investigated the transition to the 1×1 phase near completion of the β -phase, and observed continuous line-shape broadening that strongly suggests the transition is second-order.

This report raises several questions for future study. For example, how good an approximation is a lattice-gas model for the region below a coverage of $1/3\text{ML}$? Is the 1×1 phase at low coverages qualitatively different from the 1×1 phase near $4/3\text{ML}$, studied in this report? Is the transition to a 1×1 phase at the eutectic coverage a second-order melting transition? Clearly, Pb/Ge(111) is not a closed case! Many interesting experiments remain to be done, and it is hoped that this report will provide a useful basis for future investigations.

Acknowledgments

I wish to thank my supervisor Hans Henrik Andersen, and my co-supervisors, Mourits Nielsen and Robert Johnson, for their active support and encouragement at all stages in this study. Many stimulating discussions with Mourits Nielsen have helped to sharpen my understanding of surface phenomena considerably. Robert Johnson has taught me the fine art of UHV sample preparation, and his unshakeable good humour in the face of every vacuum leak and dropped sample was crucial to the success of the measurements.

It was a great pleasure to work alongside two enthusiastic young researchers, Robert Feidenhans'l and Jan Skov Pedersen; for their help with the experiments, and the many discussions we have shared, I am most grateful. I acknowledge useful discussions with several other scientists: Jens Als-Nielsen, Jakob Bohr, Paul Cowan, Bhupendra Dev, Jacques Ghijsen, Kristian Kjær, Guy Le Lay and Gert Materlik.

The technical assistance of the staff at HASYLAB and Risø National Laboratory is gratefully acknowledged. Hermann Kölln deserves special thanks for ensuring the successful operation of the transfer chamber.

I wish to thank Lin Chen and Tora Skov for drawing the many figures, and Lajla Frederiksen and Lone Astradsson for their expert help with the word-processing.

During the course of this work I received a grant from the Max Planck Institute for Solid State Research, which I gratefully acknowledge.

Financial support for these experiments was provided by the Danish National Science Foundation, the German Federal Minister for Science and Technology and the Max Planck Society.

Title and author(s) THE PHASES OF Pb/Ge(111): A SURFACE X-RAY DIFFRACTION STUDY François Grey	Date March 1988
	Department or group Physics
	Groups own registration number(s)
	Project/contract no.
Pages 81 Tables 11 Illustrations 40 References 67	ISBN 87-550-1454-2
Abstract (Max. 2000 char.) <p>This report describes the results of several surface X-ray diffraction measurements of a chemisorbed overlayer of Pb on the Ge(111) surface. Three phases of Pb/Ge(111) exist in the monolayer regime: the α- and β-phases with a $\sqrt{3} \times \sqrt{3} R30^\circ$ unit cell, and a high-temperature 1×1 phase. In the 1×1 phase of Pb/Ge(111), isotropic x-ray scattering is observed consistent with a two-dimensional liquid phase. Measurements of the integer-order Bragg reflections through the $\sqrt{3} \times \sqrt{3} R30^\circ \rightarrow 1 \times 1$ transition confirm the liquid-like nature of the 1×1 phase, and show that the liquid layer is modulated by the periodic potential of the substrate. By measuring variations of the $(2/3, 2/3)$ surface Bragg reflection from the $\sqrt{3} \times \sqrt{3} R30^\circ$ phase as a function of temperature and coverage, a simple phase diagram for Pb/Ge(111) is deduced. Below $1/3$ ML (where 1 ML is one Pb atom per Ge surface atom) the α-phase coexists with the 1×1 phase. Between $1/3$ ML and $4/3$ ML, α- and β-phases form a two-phase system displaying phase separation. Analogies with simple theoretical phase diagrams are emphasized.</p>	
Descriptors	
Available on request from Riso Library, Riso National Laboratory (Riso Bibliotek, Forskningscenter Riso), P.O. Box 49, DK-4000 Roskilde, Denmark. Telephone 02 37 12 12, ext. 2262. Telex: 43116, Telefax: 02 36 06 09	

Available on exchange from:
Risø Library,
Risø National Laboratory,
P.O. Box 49, DK-4000 Roskilde, Denmark
Phone (02) 37 12 12 ext. 2262

ISBN 87-550-1454-2
ISSN 0418-6435